ARL-TR-93-10

Interaction of Multiple Spark-Generated Bubbles in a Compressible Liquid

Technical Report under Grants N00014-91-J-1366 and N00014-93-J-0018

Jeffrey A. Cook

Applied Research Laboratories
The University of Texas at Austin
P. O. Box 8029 Austin, TX 78713-8029

1 June 1993

Technical Report

Approved for public release;
distribution is unlimited.

Prepared for:

Office of Naval Research
Physics Division ONR 312
Department of the Navy
Arlington, VA 22217-5660

REPORT DOCUMENTATION PAGE

Form Approved
OMB No. 0704-0188

1. AGENCY USE ONLY (Leave blank)	2. REPORT DATE	3. REPORT TYPE AND DATES COVERED
	1 Jun 93	technical

4. TITLE AND SUBTITLE
Interaction of Multiple Spark-Generated Bubbles in a Compressible Liquid, Technical Report under Grants N00014-91-J-1366 and N00014-93-J-0018

5. FUNDING NUMBERS
G N00014-91-J-1366
and
PE 61153N
G N00014-93-J-0018
TA 3126964

6. AUTHOR(S)
Jeffrey A. Cook

7. PERFORMING ORGANIZATION NAME(S) AND ADDRESS(ES)
Applied Research Laboratories
The University of Texas at Austin
P.O. Box 8029
Austin, TX 78713-8029

8. PERFORMING ORGANIZATION REPORT NUMBER
ARL-TR-93-10

9. SPONSORING/MONITORING AGENCY NAME(S) AND ADDRESS(ES)
Office of Naval Research
Physics Division ONR 312
800 North Quincy Street
Arlington, VA 22217-5660

10. SPONSORING/MONITORING AGENCY REPORT NUMBER

11. SUPPLEMENTARY NOTES
Ph.D. Dissertation of Jeffrey A. Cook

12a. DISTRIBUTION/AVAILABILITY STATEMENT
Approved for public release:
Distribution unlimited.

12b. DISTRIBUTION CODE

13. ABSTRACT (Maximum 200 words)

This dissertation describes the interaction of bubbles generated by underwater electrical discharges. The oscillations of these high temperature vapor and plasma bubbles generate acoustic signatures similar to the signatures generated by air guns, underwater explosions, and combustible sources. Tasks performed by these hydrodynamic sources typically require multiple sources in an array to achieve a directional beam. The properties of a single isolated source can be used to estimate the properties of an array of multiple sources, but in many cases, the acoustic properties of the source change dramatically when several sources are placed near one another. A set of model equations was developed in this report that allowed the time evolution of the bubble generated by a spark discharge to be calculated numerically from a given discharge. A simple interaction scheme was used to couple the model equations for multiple bubbles. The coupled equations were integrated simultaneously to determine the dynamics of the elements. An apparatus containing seven individual spark discharge elements was designed and constructed to test the interaction model experimentally. The model and experimental data agreed over separations down to a few bubble diameters, and the study described when the interaction between bubbles could be neglected.

14. SUBJECT TERMS		15. NUMBER OF PAGES
bubble dynamics	multiple bubble interaction	152
spark-generated	vapor bubble	16. PRICE CODE

17. SECURITY CLASSIFICATION OF REPORT	18. SECURITY CLASSIFICATION OF THIS PAGE	19. SECURITY CLASSIFICATION OF ABSTRACT	20. LIMITATION OF ABSTRACT
UNCLASSIFIED	UNCLASSIFIED	UNCLASSIFIED	

TABLE OF CONTENTS

This page intentionally left blank

LIST OF FIGURES AND TABLES

PREFACE

This is the technical report version of Jeffrey A. Cook's dissertation submitted in partial fulfillment of the requirements for the Ph.D. degree in Physics. This effort was primarily supported by the Office of Naval Research, under Grants N00014-91-J-1366 and N00014-93-J-0018.

This page intentionally left blank

1. INTRODUCTION

1.1 Summary

The underwater spark discharge creates a high pressure plasma/vapor bubble in water, and the oscillations of this bubble generate an acoustic signature similar to the signatures generated by air guns, underwater explosions, and combustible sources.[1,2,3] All of these hydrodynamic sources (including the spark discharge) radiate sound by creating a bubble in a body of water. Underwater spark discharges have been used as active sources in a number of roles, performing many of the same tasks as the other hydrodynamic sources.[4,5,6,7] These tasks typically require directional beams, and multiple sources are necessary to achieve this directivity of the radiated sound. The properties of a single isolated source can be used to estimate the properties of an array of multiple sources, but in many cases the acoustic properties of a given source change dramatically when several sources are placed near one another. Several papers have been published describing the interaction between air gun elements in an array,[8,9,10,11] and these papers indicate that a proper accounting of the interaction effects between multiple air guns is necessary to explain the resulting signature.

This report describes the interaction of a collection of spark-generated bubbles. A set of model equations was developed that allowed the time evolution of the bubble generated by a spark discharge to be calculated numerically from a set of known input parameters. A simple interaction scheme that coupled the model equations for multiple bubbles was then proposed. The coupled equations for a number of elements were integrated simultaneously to find the resulting properties of the collection of elements. An apparatus containing seven individual spark-discharge elements was designed and constructed to test the interaction model experimentally. The model and experimental data generated in this way described the collective dynamics of an array of spark-generated bubbles. The study proposed to understand quantitatively how the dynamics of this collection of bubbles changed and when the interaction between bubbles could be neglected. Although this model was developed specifically for spark discharge bubbles, the interaction of any arbitrary collection of hydrodynamic sources could be investigated with a few minor modifications to the model.

1.2 Typical Shot

The actual physical processes happening during and after the discharge must be discussed before the dynamics of the spark-generated bubbles can be discussed in detail. A single one-element experimentally measured acoustic signature (a shot) will be described and analyzed. This shot was representative of the data collected at Lake Travis and will be referred to as the "typical" shot. The statistics of the discharges used for this multiple bubble experiment are discussed in Chap. 6. Because the goal of this study was to isolate and investigate the effects of multiple

bubble interactions, the variability among discharges was minimized as much as possible. Even with the precautions taken, some amount of variability existed from shot to shot. The shot described in this report was representative of the data taken with respect to both the electrical discharges and acoustic signatures. The analyzed data from all the shots are presented where appropriate; however, a detailed analysis of this single shot is very helpful in understanding spark discharges in general and the model in particular.

1.3 Discharge Overview

A very simple diagram of a typical spark discharge system is shown in Fig. 1.1. Initially, a high voltage source is used to charge a capacitor that is isolated

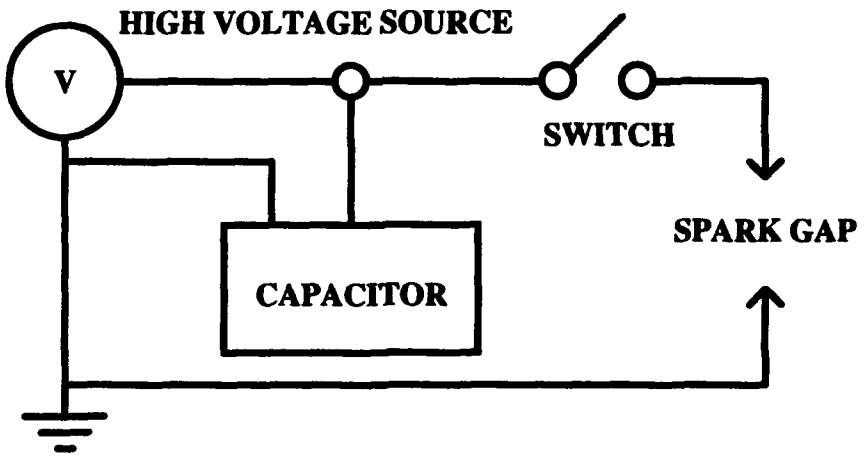

FIGURE 1.1
TYPICAL SPARK DISCHARGE SYSTEM
AS-93-268

from the electrodes. After the capacitor is charged, a switch (ignitron tube) is closed and the voltage appears across the electrode gap underwater. The dielectric in this gap (water) breaks down after a time, referred to as the breakdown time, and an arc consisting of an inertially confined plasma is formed. The measured

electrical characteristics (voltage and current) of a typical small discharge are shown in Fig. 1.2. The discharge channel grows and forms a small high pressure plasma/vapor bubble. Photographs in the literature show that the plasma fills the bubble in the early stages, then retreats to the center of the bubble as the bubble expands and cools.[12] High speed photographs taken at Applied Research Laboratories (ARL:UT) in the preliminary investigations for this study show similar results.

1.4 Qualitative Description of Acoustic Signature

The bubble expansion and collapse described above produces an acoustic signature. The acoustic signature produced by the electrical discharge shown in Fig. 1.2 is plotted in Fig. 1.3, and a modeled bubble radius is overlaid with the acoustic signature to elucidate the crucial events in the bubble evolution. The pressure shown in the acoustic signature is usually referred to simply as the pressure, but it is actually the overpressure in the liquid. The "zero" of the y-axis is the ambient pressure. The following important parts of the acoustic signature are labeled in Fig. 1.3:

1. Expansion Pulse: The bubble expands and cools under the influence of the high pressure until it reaches some maximum radius. In the early stages of the expansion, a positive pressure pulse (expansion pulse) is radiated. One of the well-defined parameters characterizing the acoustic signature is the radiated acoustic energy in this first pulse, calculated to the time the overpressure first goes negative.

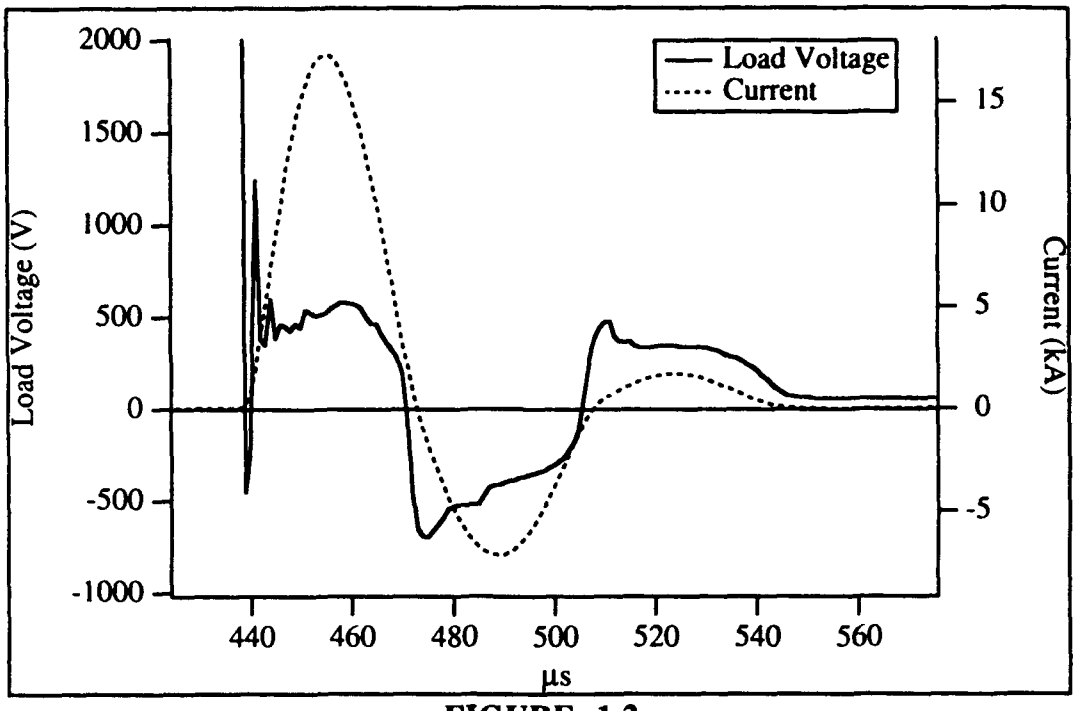

FIGURE 1.2
TYPICAL MEASURED ELECTRICAL DATA

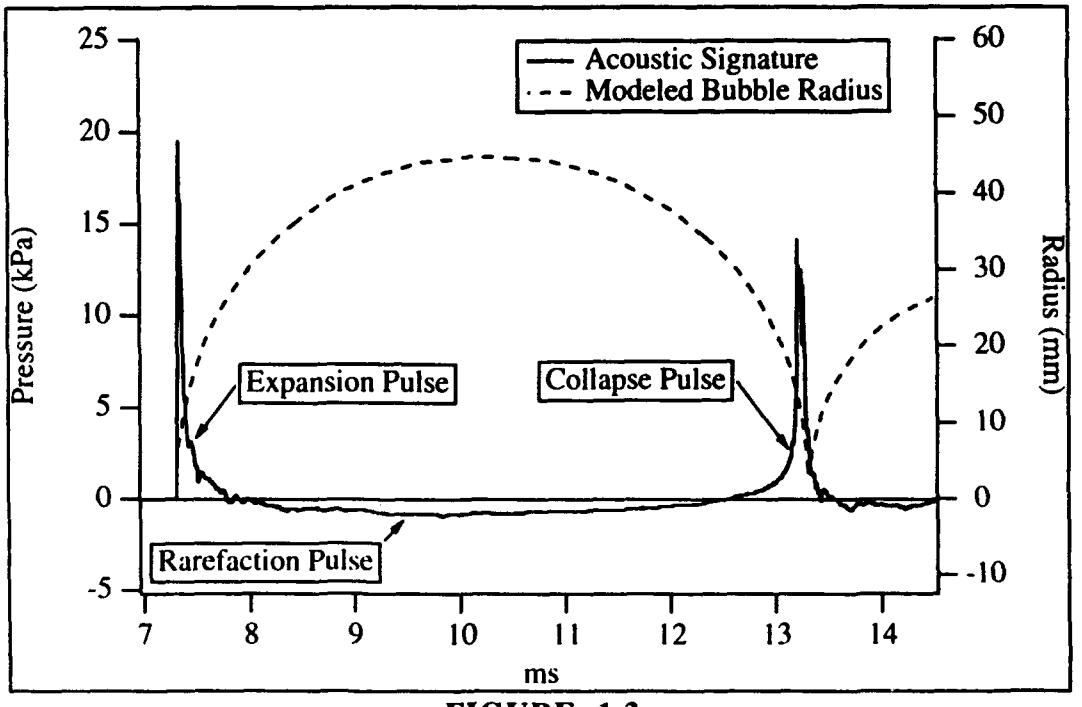

FIGURE 1.3
TYPICAL MEASURED ACOUSTIC SIGNATURE

AS-93-270

2. Rarefaction Pulse: The negative overpressure part of the acoustic signature (rarefaction pulse) is radiated while the bubble is large, and it is responsible for the low frequency part of the acoustic radiation from the bubble. The pressure inside the bubble at its maximum radius is negligible compared to the ambient static pressure, so that the bubble starts to collapse. The dynamics of the bubble at this time are very similar to those of an empty cavity.

3. Collapse Pulse: The pressure inside the bubble increases as the bubble collapses. Eventually the pressure inside the bubble becomes sufficiently high to arrest the collapse. High speed photographs show that this process is often very violent and unstable. The pressure radiated at this time is a sharp positive pulse (collapse pulse). Because of the violent nature of the collapse, multiple peaks near the time of the collapse are not unusual in the data.

4. Bubble Period: The bubble period is especially important in characterizing the energy and acoustic radiation characteristics of a given bubble, and is given by the time between the collapse pulse and expansion pulse pressure peaks. The bubble period can be used to estimate the total energy in the bubble, and that the period approximately sets the minimum frequency of the acoustic radiation from the bubble.

After this first oscillation and collapse, the oscillation repeats with subsequent oscillations and radiated acoustic signatures becoming progressively weaker. Typically, the power delivery ends very early in the bubble evolution. From there, the bubble history is influenced by the initial and ambient conditions, but not by any additional power delivery. The acoustic signature is in this respect

an indicator of the dynamic response of the bubble to ambient conditions, rather than a forced response to a continued power delivery. This signature is one of the few observables in this type of experiment and is certainly the one best suited for examining the hydrodynamic behavior of the bubble over the entire period of oscillation. Because the majority of the bubble dynamics are determined by the ambient conditions and because other nearby bubbles change these conditions, these other bubbles can have an important influence on the bubble dynamics.

1.5 Model Description

This study required a model that could accurately predict the effects of having several bubbles near one another. An important part of developing such a model was to develop a robust model that described the behavior (especially the acoustic signature) of a single isolated bubble. It was determined that for this application the match between the experimental and the model signature was of paramount importance, and that a "first principles" derivation of all aspects of the model was not necessary. Data were available from single spark discharge experiments previously conducted at ARL. This allowed the development of a model having the correct behavior with a minimum of parameters to be adjusted, using a semi-empirical approach. That is to say, the model was based on sound physical principles, but had constants that determined the relative effects or used approximations to the "real" physics to reduce computation time.

The spark-generated bubble exhibits large amplitude nonlinear motion, so a closed-form solution of the equations was not possible. To increase understanding of the dynamics of a spark-generated bubble and to further illuminate the degree

and nature of the interaction between several such bubbles, the equations governing the dynamics of the bubble were numerically integrated, using a published fourth-order Runge-Kutta routine.[13] Several equations describing the radial dynamics of a bubble in a compressible liquid were available in the literature, and it was not necessary to repeat the derivation of those equations. The various forms of the equations are briefly discussed in Chap. 3, and a good review of the equations of bubble dynamics is given by Young.[14] It was assumed that the contents of the spark-generated bubble were homogeneous and obeyed the ideal gas law, with modifications to allow for changes in the equation of state as the water vapor inside the bubble became dissociated. These modifications were necessary because of the high temperatures reached inside the bubble during the spark discharge.[15,16,17,18] These temperatures indicated that blackbody radiation might play an important role in the dynamics of the bubble. The emissivity of the bubble was determined approximately by using a frequency averaged mean free path inside the bubble. Indications in the literature[19,20,21,22,23] were that the finite rate of condensation and evaporation affects the dynamics of cavitation vapor bubbles, so a non-equilibrium model describing the exchange of mass between the bubble and surrounding liquid was included. One effect not included was the thermal conductivity of heat into the liquid. Studies indicate that thermal conductivity is not an important effect for transient vapor bubbles such as the ones examined here.[20,24] Although a finite amplitude theory is essential for propagating the acoustic signature from underwater explosions,[25] a linear acoustics solution was deemed sufficient for propagating the signature from the spark-generated bubble, especially considering the other approximations that are made in the model. Concurrent investigations by Roberts[26]

indicate that the use of a linear acoustics propagation model is sufficient for the acoustic signatures generated by the discharges examined.

This model assumes a spherical bubble isolated except for other bubbles that oscillate simultaneously in an infinite liquid. The presence of the electrode is explicitly ignored in all the calculations and simulations. Other studies have examined cavitation bubbles collapsing near a boundary, and found that the bubbles will become asymmetric near the end of the collapse. This effect is not considered in this study, as each bubble is somewhat larger than the electrode for most of its lifetime.

1.6 The Single Element Experiments (Sea Data)

The model for the bubble dynamics was compared to experimental data previously recorded by Rogers[27] in the Gulf of Mexico in 1990. These data will be referred to as the "sea" data. The sea data were used to determine the parameters in the bubble model that are introduced in Chap. 3. Comparisons between the sea data and model are presented in Chap. 4. The model was found to agree over wide ranges of energy and ambient pressure on several characteristic values of the acoustic signatures. The bubble period in particular matched very well between model and experiment, indicating that the total energy losses predicted by the model over the oscillation of the bubble were approximately correct. However, no reliable information is gained about the relative magnitudes of the individual energy loss mechanisms examined. The bubble period and the minimum rarefaction pressure are found to depend on depth, while the peak pressures in the expansion

and collapse pulses and the acoustic energy in the expansion pulse are not. The dependence in each case is discussed further in Sec. 4.2.

1.7 Motivation of the Interaction Model

Previous experiments conducted at ARL[28,29] indicated that when multiple spark-generated bubbles were initiated near one another, the resulting acoustic signature differed from the signature that would be expected if the signatures from isolated bubbles were simply added together. In particular, this deviation was observed by noting that the bubble periods of multiple spark-generated bubbles were longer than the periods of isolated bubbles created with the same discharge energy, and that the amplitude of the pressure signature in the rarefaction pulse was smaller than would be calculated by linear superposition. The studies of vapor and gas bubbles in sound fields[30,31] provided insight to modeling the interaction between multiple spark-generated bubbles. In the same way that an incident sound field alters the dynamics of an isolated bubble (by modifying the ambient pressure), the radiated sound fields of multiple bubbles were presumed to modify the dynamics of neighboring bubbles.

1.8 The Multiple Element Experiments (Lake Data)

The model equations were numerically integrated for a set of discharges similar to those that had been measured in the previous experiments. On the basis of these preliminary investigations, an experimental apparatus (described in Chap. 6) was designed and fabricated to study the multiple bubble interactions in a nearby lake equipped for acoustic studies. Data sets were collected at a number of separations, for one, three, five, and seven elements, at a fixed energy. The one-

element discharges were used to determine the statistical behavior of the data. The statistics from the data were then used to generate series of random discharges with appropriate characteristics for multiple-element model simulations.

1.9 Comparison with Lake Data

The modeled bubble data were generated by performing "numerical experiments" using the model equations. With the discharges generated randomly, the equations were integrated ten times for each separation and number of elements. Besides the simulations executed for each experimental configuration, additional simulations were run at interesting intermediate separations to "fill out" the curves. The data from the model simulations were then analyzed similarly to the experimental data. Results reported in Chap. 7 indicate that the model predicted the general form and magnitude of the changes in the bubble period and pressure signature, although the effects were smaller than the model predicted at the closest separations. The model predicted the changes in the pressure signature at intermediate spacings reasonably well. At spacings of less than two maximum bubble diameters, the predictions were not as good.

1.10 Conclusions

The data presented in this report support statements characterizing single spark-generated bubbles, and describe the nature of the interaction between multiple elements. The model developed predicted a time evolution in good agreement with the experimentally measured signatures for a single spark-generated bubble. The single spark-generated bubbles were found to have a bubble period consistent with accepted laws for cavitation bubbles, when an allowance was made

for some energy loss between the electrical discharge energy and total energy of the bubble. The model failed to capture the subtle differences between discharges of similar energies but different discharge times. Both experimental and model data on the characteristics of the discharge agree with theoretical studies of single spark-generated bubbles in the literature. Predictions by the model of temperatures reached during the discharge were in reasonable agreement with measurements made of the temperatures of bubbles created under similar experimental conditions.

The model was able to predict interaction effects down to array element separations of about two maximum bubble diameters. The model given predicted the changes in the bubble period for several element separations of interest, and predicted the pressure signature in the farfield of an array. The model accounted for the interaction between elements in the array, at least down to a spacing of about two maximum bubble diameters, where the approximations and assumptions in the model apparently met with some difficulty. It was determined that the shift in bubble periods is measurable, but probably not important, for element separations greater than about 10 maximum bubble diameters in a one-dimensional linear array, but the deviation from linear superposition must be considered in calculating the pressure signature for such an array. This spacing is less than would probably be used for typical one-dimensional arrays indicating that the real interaction of interest is the deviation from linear superposition in the pressure signatures.

---

[1]L. Bjørnø, "A Comparison Between Measured Pressure Waves in Water Arising From Electrical Discharges and Detonation of Small Amounts of Chemical Explosives," *Trans. ASME, J. Eng. Ind.*, Paper No. 69-Unt-1, 1-8 (1969).

[2]J. B. Keller and I. I. Kolodner, "Damping of Underwater Explosion Bubble Oscillations," *J. Appl. Phys.* **27**(10), 1152–1161 (1956).

[3]I. Z. Okun', "Generation of Compression Waves by a Pulsed Discharge in Water," *Zh. Tekh. Fiz.* **41**(2), 292–301 (1971) [English transl.: *Sov. Phys. – Tech. Phys.*, **16**(2), 219–226 (1971)].

[4]W. C. Beckmann, A. C. Roberts, and B. Luskin, "Sub-Bottom Depth Recorder," *Geophysics* **24**(4), 749–760 (1959).

[5]D. D. Caulfield, "Predicting Sonic Pulse Shapes of Underwater Spark Discharges," *Deep-Sea Research* **9**, 339–348 (1962).

[6]H. Edelmann, "An Underwater Sound Source with Higher Seismic Efficiency," 474–490 (1968).

[7]S. Gardner, *Electro-Acoustic Properties of the Underwater Spark Discharge* (Edo Corporation, College Point, New York, 1961), Report 5480.

[8]J. J. Nooteboom, "Signature and Amplitude of Linear Airgun Arrays," *Geophysical Prospecting* **26**, 194–201 (1978).

[9]J. E. Sinclair and G. Bhattacharya, "Interaction Effects in Marine Seismic Source Arrays," *Geophysical Prospecting* **28**, 323–332 (1980).

[10]R. C. Johnston, "Development of More Efficient Airgun Arrays: Theory and Experiment," *Geophysical Prospecting* **30**, 752–773 (1982).

[11]A. Ziolkowski, G. Parkes, L. Hatton, and T. Haugland, "The Signature of an Air Gun Array: Computation from Near-Field Measurements Including Interactions," *Geophysics* **47**(10), 1413–1421 (1982).

[12]K. A. Naugol'nykh and N. A. Roi, *ELEKTRICHESKIE RAZRJADY V VODE* (Nauka, Moskva, 1971) [English transl.: *Spark Discharges in Water* (Applied Research Laboratories, The University of Texas at Austin, 1987), Internal Report].

[13]W. H. Press, B. P. Flannery, S. A. Teukolsky, and W. T. Vetterling, *Numerical Recipes in Pascal* (Cambridge University Press, Cambridge, 1989), Chap. 15, pp. 599–632.

[14]F. R. Young, *Cavitation* (McGraw-Hill Book Company, London, 1989), Chap. 2, pp. 8–37.

[15]E. A. Martin, *The Underwater Spark: An Example of Gaseous Conduction at About 10,000 Atmospheres*, Ph.D. Dissertation, University of Michigan, Ann Arbor, 1956.

[16]E. A. Martin, "Experimental Investigation of a High-Energy Density, High-Pressure Arc Plasma," *J. Appl. Phys.* **31**(2), 255–267 (1960).

[17]A. I. Ioffe, "Theory of the Initial Stage of an Electrical Discharge in Water," *J. Appl. Mech. Tech. Phys. (PMTF)* **7**(6), 69–72 (1966).

[18]J. W. Robinson, M. Ham, and A. N. Balaster, "Ultraviolet Radiation from Electrical Discharges in Water," *J. Appl. Phys.* **44**(1), 72–75 (1973).

[19]S. Fujikawa and T. Akamatsu, "Effects of the Non-Equilibrium Condensation of Vapour on the Pressure Wave Produced by the Collapse of a Bubble in a Liquid," *J. Fluid Mech.* **97**(3), 481–512 (1980).

[20]M. S. Plesset and A. Prosperetti, "Bubble Dynamics and Cavitation," *Ann. Rev. Fluid Mech.* **9**, 145–185 (1977).

[21]W. J. Bornhorst and G. N. Hatsopoulos, "Analysis of a Liquid Vapor Phase Change by the Methods of Irreversible Thermodynamics," *J. Appl. Mech.* **34**, 840–846 (1967).

[22]W. J. Bornhorst and G. N. Hatsopoulos, "Bubble-Growth Calculation without Neglect of Interfacial Discontinuities," *J. Appl. Mech.* **34**, 847–853 (1967).

[23]T. Mitchell and F. G. Hammitt, "On the Effects of Heat Transfer upon Collapsing Bubbles," *Nuc. Sci. Eng.* **53**, 263–276 (1974).

[24]C. Herring, *Theory of the Pulsations of the Gas Bubble Produced by an Underwater Explosion* (Columbia University, New London, Connecticut, 1941), NDRC Report No. C4–sr20–010.

[25]R. H. Cole, *Underwater Explosions* (Princeton University Press, Princeton, New Jersey, 1948).

[26]R. M. Roberts, *The Energy Partition of Underwater Sparks*, Ph.D. Dissertation (The University of Texas at Austin, to be published).

[27]R. L. Rogers, *Intermediate Energy Tests and Analysis of a Plasma Sound Source*, Applied Research Laboratories, The University of Texas at Austin, 1992, Report ARL–TR–92–15.

[28]J. A. Cook, "Studies of Various Electrode Configurations for a Plasma Sound Source," *J. Acoust. Soc. Am. Suppl. 1* **88**, S168 (1990).

[29]J. A. Cook, "Mutual Coupling Effects Between Elements in a Spark Source Array," *J. Acoust. Soc. Am.* **90**(4), Pt. 2, 2350 (1991).

[30]A. Prosperetti and A. Lezzi, "Bubble Dynamics in a Compressible Liquid. Part 1. First-order Theory," *J. Fluid Mech.* **168**, 457–478 (1986).

[31]J. B. Keller and M. Miksis, "Bubble Oscillations of Large Amplitude," *J. Acoust. Soc. Am.* **68**(2), 628–633 (1980).

2. THEORY

2.1 Bubble Dynamics in an Incompressible Fluid

In the first examination of the bubble dynamics, the fluid was assumed to be incompressible. Therefore, the sound speed is infinite or, equivalently, the mach number vanishes, where the mach number is defined as the ratio of the bubble wall velocity to the speed of sound $\left(m = \dot{R}/c_\infty\right)$. Although the equation of dynamics outlined here was not used in the simulations, some insight is derived by looking at this incompressible form of the equation.

Consider a spherical bubble in an infinite liquid. The appropriate equations are the continuity equation and Euler's equation (the momentum equation):[1]

$$\frac{\partial \rho}{\partial t} + \nabla \cdot (\rho \mathbf{u}) = 0 \tag{2.1}$$

$$-\nabla p = \rho \left[\frac{\partial \mathbf{u}}{\partial t} + (\mathbf{u} \cdot \nabla)\mathbf{u} \right] \quad . \tag{2.2}$$

The assumption of spherical symmetry implies purely radial motion and allows the introduction of a velocity potential:

$$\varphi; \quad \mathbf{u} = \nabla \varphi \quad . \tag{2.3}$$

Replacing $\mathbf{u}$ in Eq. (2.2) with $\nabla\varphi$ and integrating from an undisturbed region to the region of interest (assuming isentropic motion in the liquid, and that the variables in the undisturbed liquid take their equilibrium values):

$$\int_{p_-}^{p}\frac{dp}{\rho}+\frac{\partial\varphi}{\partial t}+\frac{1}{2}u^2=0 \quad . \tag{2.4}$$

A definition suitable for our purposes is that the integral in Eq. (2.4) is the enthalpy difference between the liquid at pressure p and the liquid at pressure p_-, hereafter referred to as the liquid enthalpy:[2]

$$h=\int_{p_-}^{p}\frac{dp}{\rho} \quad . \tag{2.5}$$

This definition is consistent with an assumption of isentropic motion in the liquid.[3] Substitution into Eq. (2.4) gives the equation usually referred to as the Bernoulli integral:

$$h+\frac{\partial\varphi}{\partial t}+\frac{1}{2}u^2=0 \quad . \tag{2.6}$$

Now, assuming the fluid is incompressible $(\rho=\rho_-=\text{constant})$, Eq. (2.1) becomes the incompressible continuity equation:

$$\frac{\partial\left(r^2u\right)}{\partial r}=0 \qquad \Rightarrow \qquad r^2u=\text{constant} \quad . \tag{2.7}$$

If the bubble radius is denoted by R and the bubble wall velocity by $\dot{R}$, then the kinematic boundary condition at the bubble wall is given by

$$u\big|_{r=R}=\left.\frac{\partial\varphi}{\partial r}\right|_{r=R}=\dot{R} \quad . \tag{2.8}$$

The small signal continuity equation (Eq. (2.7)) and the kinematic boundary condition (Eq. (2.8)) together imply

$$r^2u=R^2\dot{R} \quad . \tag{2.9}$$

Solving this expression for u and integrating with respect to r yields an explicit expression for the velocity potential

$$\varphi = -\frac{R^2\dot{R}}{r} \quad . \tag{2.10}$$

In the case of small signals, the liquid enthalpy can be approximated by the first term in a Taylor series expansion [see Eq. (2.24)], giving the incompressible liquid enthalpy:

$$h \cong \frac{p - p_\infty}{\rho_\infty} \quad . \tag{2.11}$$

Substituting these expressions into the Bernoulli integral [Eq. (2.6)], and writing the radial and time dependence explicitly in the pressure term, the incompressible liquid pressure distribution is given by

$$p(r,t) - p_\infty = \rho_\infty \frac{R^2\ddot{R} + 2\dot{R}^2 R}{r} - \rho_\infty \frac{\dot{R}^2 R^4}{2r^4} \quad . \tag{2.12}$$

To complete the formulation of the equation of bubble dynamics in an incompressible liquid, Eq. (2.12) is evaluated at $r = R$. The resulting equation is the incompressible equation of bubble dynamics, first written in this form by Lord Rayleigh:[4]

$$R\ddot{R} + \frac{3}{2}\dot{R}^2 = \frac{p(R,t) - p_\infty}{\rho_\infty} \quad . \tag{2.13}$$

In this equation, $p(R,t)$ is explicitly a function of the bubble radius and, therefore, implicitly a function of time. If the cavity is assumed empty, this equation of bubble dynamics reduces to:

$$R\ddot{R} + \frac{3}{2}\dot{R}^2 = -\frac{p_\infty}{\rho_\infty} \quad . \tag{2.14}$$

If R is chosen as the independent variable, and a separation of variables is performed, Eq. (2.14) can be integrated once to yield an expression for the bubble wall velocity:

$$\int_0^{\dot{R}} dx\, x\left[\frac{3}{2}x^2+\frac{p_\infty}{\rho_\infty}\right]^{-1} = -\int_{R_{max}}^{R} dx\, x^{-1} \tag{2.15}$$

$$\frac{1}{3}\ln\left(1+\frac{3}{2}\frac{\rho_\infty}{p_\infty}\dot{R}^2\right) = \ln\left(\frac{R_{max}}{R}\right) \tag{2.16}$$

$$1+\frac{3}{2}\frac{\rho_\infty}{p_\infty}\dot{R}^2 = \left(\frac{R_{max}}{R}\right)^3 . \tag{2.17}$$

Solving this expression for the square of the bubble wall velocity,

$$\dot{R}^2 = \frac{2}{3}\frac{p_\infty}{\rho_\infty}\left[\left(\frac{R_{max}}{R}\right)^3-1\right] . \tag{2.18}$$

Notice that $\dot{R}^2$ tends to infinity as R vanishes in the case of an empty cavity. This is the difficulty with the incompressible equation of bubble dynamics. The fluid near the bubble wall would have a velocity greater than the speed of sound as the bubble collapses. The assumption of an incompressible fluid will obviously be wrong in this case. The difficulty in the theory can be avoided by assuming the cavity contains a small amount of gas or water vapor. When this is done, the increasing pressure inside the cavity halts the collapse and $\dot{R}$ is bounded. Whether or not the incompressible fluid assumption is valid when a gas or vapor fills the cavity depends on the amount of gas or vapor initially present in the cavity, as the magnitude of the maximum bubble wall velocity will be reduced as the pressure inside the cavity increases. In the case of a cavity filled with water vapor, a portion of the vapor initially present in the cavity may condense against the surface. The pressure inside the cavity may not increase until the speed of the bubble wall

exceeds the speed at which the finite rate of condensation can maintain equilibrium conditions. A full treatment of the gas-filled bubble in an incompressible liquid has previously been done and will not be repeated here.[5,6]

2.2 Acoustic Signature Calculation

The equations of bubble dynamics that were used to model the spark-generated bubbles contain an expression that gives the pressure in the liquid at the bubble surface as a function of the state variables for the bubble contents. From this pressure, using the available information about the bubble dynamics, the pressure at a particular point was calculated. Some insight into the two terms in Eq. (2.12) is gained by replacing the bubble radius with the bubble volume. The pressure distribution equation takes the form:

$$p(r,t) - p_{\infty} = \rho_{\infty} \frac{\ddot{V}}{4\pi r} - \frac{1}{2}\rho_{\infty} \frac{\dot{V}^2}{(4\pi)^2 r^4} \quad . \tag{2.19}$$

The first term on the right hand side, which contains the volume acceleration, is the general form of the radiation from a simple source,[7] while the second term describes the changes in the pressure field near the bubble. These observations led to the identification of this first term as the farfield term, and the second as the afterflow term.[8] The pressure distribution can be written explicitly identifying those terms:

$$p(r,t) - p_{\infty} = \frac{R}{r} p_{\text{farfield}}(t) + \frac{R^4}{r^4} p_{\text{afterflow}}(t) \tag{2.20}$$

$$p_{\text{farfield}}(t) = \rho_{\infty}\left(R\ddot{R} + 2\dot{R}^2\right) \tag{2.21}$$

$$p_{\text{afterflow}}(t) = -\frac{\rho_{\infty}}{2}\dot{R}^2 \quad . \tag{2.22}$$

The farfield term is the pressure that is radiated to infinity as a compression wave, while the afterflow term denotes the incompressible radial flow near the bubble that results from the passage of the pressure wave. Computation of the pressure in the nearfield (distances on the order of the bubble diameter) requires both of these terms. At larger distances, the afterflow term is negligible, and the pressure distribution in the liquid is often calculated using only the farfield term. The pressure in the liquid at the surface of the bubble contains both terms, and each must be propagated with the proper radial dependence to ensure that the afterflow term becomes negligible in the farfield. Before discussing how this is done, the equation for the pressure distribution in the liquid will be examined to determine what modifications should be made for a compressible liquid.

A simple solution was found for the pressure distribution in the incompressible case. It turns out that the same expression is also valid in the acoustic approximation to first order by simply evaluating the terms relating to the bubble dynamics at the appropriate retarded time, assuming a finite propagation speed. The equations used to derive the pressure distribution previously will be used again, but this time the terms relating to the compressibility will be written explicitly. A finite sound speed will be introduced, and the pressure distribution equation will be derived again, keeping terms up to second order in the sound speed.

As mentioned, when the liquid enthalpy was discussed previously, the motion in the liquid is considered isentropic, and the sound speed is defined as[3]

$$\frac{dp}{d\rho} = c^2 \quad . \tag{2.23}$$

With this definition, and the one given previously for the liquid enthalpy, Taylor series expansions of the liquid enthalpy and the sound speed around ρ_∞ and c_∞ can be performed:

$$h = \int_{p_\infty}^{p} \frac{\mathrm{d}p}{\rho} = \int_{p_\infty}^{p} \frac{\mathrm{d}p}{\rho_\infty}\left(1 - \frac{p-p_\infty}{\rho_\infty c_\infty^2} + \ldots\right) = \frac{p-p_\infty}{\rho_\infty} - \frac{1}{2c_\infty^2}\left(\frac{p-p_\infty}{\rho_\infty}\right)^2 + \ldots \qquad (2.24)$$

$$c^{-2} = c_\infty^{-2} + (p-p_\infty)\frac{\mathrm{d}c^{-2}}{\mathrm{d}p} + \ldots = c_\infty^{-2} - \frac{p-p_\infty}{c_\infty^4}\frac{\mathrm{d}c^2}{\mathrm{d}p} + \ldots \quad . \qquad (2.25)$$

Substituting these expansions into the continuity and Bernoulli equations [Eqs. (2.1) and (2.6)], and replacing the particle velocity with the velocity potential (Eq. (2.3)) gives a form of the continuity and Bernoulli equations accurate to order c_∞^{-2}:

$$\nabla^2\varphi + \frac{1}{\rho_\infty c_\infty^2}\left(\frac{\partial p}{\partial t} + \frac{\partial \varphi}{\partial r}\frac{\partial p}{\partial r}\right) = 0 \qquad (2.26)$$

$$\frac{\partial \varphi}{\partial t} + \frac{1}{2}(\nabla\varphi)^2 + \frac{p-p_\infty}{\rho_\infty}\left(1 - \frac{p-p_\infty}{2\rho_\infty c_\infty^2}\right) = 0 \quad . \qquad (2.27)$$

A finite speed of sound is assumed, and this requires that any terms depending on an event occurring at a position other than r be evaluated at the retarded time:

$$t_r = t - r/c_\infty \quad . \qquad (2.28)$$

Following the previous derivation for the pressure distribution in an incompressible liquid,

$$r^2 u(r,t) = \text{constant} + O\left(c_\infty^{-2}\right) \;\Rightarrow\; r^2 u(r,t) = \left[R^2\dot{R}\right]_{t_r} + O\left(c_\infty^{-2}\right) \qquad (2.29)$$

$$\varphi(r,t) = -\frac{1}{r}\left[R^2\dot{R}\right]_{t_r} + O\left(c_\infty^{-2}\right) \qquad (2.30)$$

$$\frac{\partial \varphi(r,t)}{\partial t} = -\frac{1}{r}\left[2R\dot{R}^2 + R^2\ddot{R}\right]_{t_r} + O\left(c_\infty^{-2}\right) \qquad (2.31)$$

$$\frac{\partial \varphi(r,t)}{\partial t} + \frac{1}{2}\left(u(r,t)\right)^2 + \frac{p(r,t)-p_\infty}{\rho_\infty} + O\left(c_\infty^{-2}\right) = 0 \quad . \qquad (2.32)$$

The final expression for the first order pressure distribution is then given by

$$p(r,t)-p_\infty=\left[\rho_\infty\frac{R}{r}\left(R\ddot{R}+2\dot{R}^2\right)-\rho_\infty\frac{R^4}{r^4}\frac{\dot{R}^2}{2}\right]_{t_r} \quad . \tag{2.33}$$

Except for the terms on the right hand side being evaluated at the retarded time, this final expression is the same as was derived earlier for the incompressible case, provided the second order sound speed terms are neglected. Solution of the equations to order c_∞^{-2} is much more difficult, and it will be found later that the second order terms are not necessary, because the equation to be used for the bubble dynamics will have only first order corrections. This equation for the pressure distribution can be used to calculate the pressure at any point in the liquid provided the bubble radius, and the velocity and acceleration of the bubble wall are known. In practice however, the pressure calculated using the bubble wall acceleration is not as smooth as the pressure calculated using the liquid pressure directly. An expression will therefore be derived from this equation that allows the pressure distribution in the liquid to be calculated using the liquid pressure at the bubble wall, bubble radius, and bubble wall velocity. In the following equations, the radial and time dependence are identified explicitly in the pressure term, while the terms relating to the bubble dynamics are assumed to be evaluated at the appropriate retarded time. In the interest of eliminating $R\ddot{R}$ from the pressure distribution in favor of the liquid pressure, Eq. (2.13) is solved for $R\ddot{R}$:

$$R\ddot{R}=\frac{p(R,t)-p_\infty}{\rho_\infty}-\frac{3}{2}\dot{R}^2 \quad . \tag{2.34}$$

The following symbol is introduced for the liquid pressure at the bubble wall:

$$p_B(t)\equiv p(R,t) \quad . \tag{2.35}$$

Substituting these two expressions into the previous equation for the pressure distribution (Eq. (2.33)), the following final expression is found:

$$p(r,t)-p_{\infty}=\left[\frac{R}{r}\left(p_B(t)-p_{\infty}+\left(1-\frac{R^3}{r^3}\right)\frac{\rho_{\infty}\dot{R}^2}{2}\right)\right]_{t_r} \quad . \tag{2.36}$$

This is the equation that was used to calculate the pressure distribution in the liquid from the variables that were integrated in the model equations, and it is identical to the Eq. (1.3) given by Plesset[9] when the right hand side of that equation is evaluated at the retarded time.

The acoustic energy radiated can be calculated from the pressure signature and the particle velocity:[1]

$$E_{acoustic}=4\pi r^2\int\left[p(r,t)-p_{\infty}\right]\cdot u\,dt \quad . \tag{2.37}$$

For a spherically spreading wave, the complex particle velocity $(\tilde{u})$ can be calculated from the pressure using the specific acoustic impedance (z):

$$\tilde{u}=\frac{p}{z}=\frac{p}{\rho_{\infty}c_{\infty}\cos\theta}e^{-i\theta}=ue^{-i\theta} \qquad \theta\equiv\cot^{-1}kr \quad . \tag{2.38}$$

For a spherically spreading pressure wave, the particle velocity is not in phase with the pressure. If *kr* is large, however, Eq. (2.38) reduces approximately to the plane wave relation:

$$u\cong\frac{p}{\rho_{\infty}c_{\infty}} \quad . \tag{2.39}$$

The acoustic energy for large *kr* is therefore given approximately by

$$E_{acoustic}=\frac{4\pi r^2}{\rho_{\infty}c_{\infty}}\int\left[p(r,t)-p_{\infty}\right]^2 dt \quad . \tag{2.40}$$

2.3 Bubble Period

The bubble wall velocity was given in Eq. (2.18) as a function of the bubble radius for a collapsing empty cavity. The same expression can be derived directly from energy considerations. This type of cavity is usually referred to as a Rayleigh cavity, in reference to Lord Rayleigh's work. An examination of this type of cavity, although often done in the literature,[10,11,12] will be repeated briefly here because of its importance and usefulness. As before, consider an isolated empty cavity in an infinite homogeneous incompressible fluid. The total kinetic energy in the liquid as the liquid collapses into the cavity is given by

$$T_{KE} = \frac{\rho_\infty}{2}\int_R^\infty \dot{r}^2 4\pi r^2 dr = 2\pi\rho_\infty \dot{R}^2 R^3 \quad . \tag{2.41}$$

Then, for a cavity starting at radius R_{max}, assuming isothermal compression and a constant hydrostatic pressure, the work done by the water in compressing the cavity to a radius R is given by

$$W(R) = \frac{4}{3}\pi\left(R_{max}^3 - R^3\right)p_\infty \quad . \tag{2.42}$$

Demanding that these two expressions balance the available energy yields immediately

$$\dot{R}^2 = \frac{2}{3}\frac{p_\infty}{\rho_\infty}\left[\left(\frac{R_{max}}{R}\right)^3 - 1\right] \quad . \tag{2.43}$$

This expression is identical to the one derived earlier in Eq. (2.18). Separating variables and integrating both sides of Eq. (2.43) gives an expression that can be evaluated numerically for the time to collapse to any given final radius:

$$\frac{dR}{dt} = -\sqrt{\frac{2p_\infty}{3\rho_\infty}}\left[\frac{R_{max}^3}{R^3} - 1\right]^{1/2} \tag{2.44}$$

$$\int_0^{\tau_{collapse}} dt = -\sqrt{\frac{2}{3}\frac{\rho_\infty}{p_\infty}} \int_{R_{max}}^{R_{final}} dR \left[\left(\frac{R_{max}}{R} \right)^3 - 1 \right]^{-1/2} \quad . \tag{2.45}$$

If the integration is carried out to a final radius $R_{final} = 0$, then a closed-form solution is obtained for the collapse time:

$$\tau_{collapse} = R_{max} \left(\frac{\pi}{6} \frac{\rho_\infty}{p_\infty} \right)^{1/2} \frac{\Gamma\left(\frac{5}{6}\right)}{\Gamma\left(\frac{4}{3}\right)} = 0.915 R_{max} \left(\frac{\rho_\infty}{p_\infty} \right)^{1/2} \quad . \tag{2.46}$$

The bubbles created by underwater sparks have properties similar to these empty cavities, so that the collapse time is a very useful quantity. If the expansion phase is assumed to be a mirror image of the collapse phase, the total period of oscillation, hereafter referred to as the bubble period, is given by

$$\tau = 2 \cdot \tau_{collapse} = 1.83 R_{max} \left(\frac{\rho_\infty}{p_\infty} \right)^{1/2} \quad . \tag{2.47}$$

Another interesting formulation of the bubble period considers the hydromechanical energy in the bubble. At $R = R_{max}$, the kinetic energy vanishes, and the potential energy of the cavity is given by Eq. (2.42) as

$$E = \frac{4}{3} \pi R_{max}^3 \, p_\infty \quad . \tag{2.48}$$

This energy is the total energy for the empty cavity. If the cavity was created by an electrical discharge, the energy delivered by that discharge ($E_{discharge}$) is related to the energy in the cavity by the efficiency of whatever energy conversion processes might be involved. This efficiency has been referred to as the hydraulic efficiency of the discharge:[13]

$$\varepsilon_{hyd} = E / E_{discharge} \quad . \tag{2.49}$$

Solving Eq. (2.48) for R_{max} and substituting into Eq. (2.47) yields an expression for the bubble period in terms of the potential energy:

$$\tau = 1.83\left(\frac{3}{4\pi}\right)^{1/3} \frac{\rho_\infty^{1/2} E^{1/3}}{p_\infty^{5/6}} \quad . \tag{2.50}$$

Alternatively, this expression may be written with the delivered energy and the hydraulic efficiency:

$$\tau = 1.83\left(\frac{3}{4\pi}\right)^{1/3} \frac{\rho_\infty^{1/2} \left(\varepsilon_{hyd} E_{discharge}\right)^{1/3}}{p_\infty^{5/6}} \quad . \tag{2.51}$$

This expression for the bubble period is especially useful for gauging the behavior of spark bubbles, as the liquid density, delivered energy, and ambient pressure are all known.

A matter to be addressed is whether the bubble period will obey this equation when a bubble is filled with water vapor, instead of being empty. A calculation has been done[14] for a gas-filled bubble, and the result is that

$$\tau \cong \left(1 + P_0 / p_\infty\right) \cdot \tau_{collapse} \quad , \tag{2.52}$$

where P_0 is the initial pressure in the gas, γ has been taken to be $\frac{4}{3}$, and $\tau_{collapse}$ is given by Eq. (2.46). This expression will probably overestimate the correction, because some of the vapor will condense against the bubble wall. Because the vapor pressure is typically only about 1% of the ambient pressure in the experiments performed, the bubble period shift from this effect is expected to be about 1%. The standard deviation on the bubble periods in the experiments performed was about 3%. In this case, it does not appear that a correction to the bubble period calculated from the Rayleigh calculation is necessary, except that the discharge energy should be multiplied by an efficiency (ε_{hyd}) that is dependent on the electrical discharge system. The data taken in previous experiments with spark-generated bubbles tend to confirm this choice,[15,16] although it has been reported by

another source[17] that spark-generated bubbles do not obey Eq. (2.51). This equation for the bubble period will be discussed in more detail in Chap. 4.

The bubble period characterizes the lowest frequency of the acoustic radiation from a bubble. This fundamental frequency is related to the bubble period by

$$f_{peak} \approx \tau^{-1} \quad . \tag{2.53}$$

The wavelength of this radiation is given by

$$\lambda_{fundamental} = \frac{c_\infty}{f_{peak}} \quad . \tag{2.54}$$

The wavelength of the fundamental radiation can therefore be related to the maximum bubble diameter using Eqs. (2.47) and (2.54):

$$\lambda_{fundamental} \approx c_\infty \tau \approx \frac{2c_\infty R_{max}}{\sqrt{p_\infty/\rho_\infty}} \approx \frac{D_{max}}{\varepsilon_0} \tag{2.55}$$

$$\varepsilon_0 = \frac{\sqrt{p_\infty/\rho_\infty}}{c_\infty} \quad . \tag{2.56}$$

The acoustic mach number (ε_0) is introduced here and gives a rough scaling of the bubble wall mach number for a general bubble collapse. The multiple bubble experiments presented in this report were performed at a depth of about 10 m, leading to a value for the acoustic mach number of about 0.01. The maximum diameter of the bubbles (D_{max}) at this depth is about 100 times smaller than the wavelength of the fundamental frequency of the radiation from the bubble.

---

[1]L. E. Kinsler, A. R. Frey, A. B. Coppens, and J. V. Sanders, *Fundamentals of Acoustics* (John Wiley and Sons, New York, 1982), 3rd ed.

[2]F. R. Gilmore, *The Growth or Collapse of a Spherical Bubble in a Viscous Compressible Liquid* (California Institute of Technology Hydrodynamics Laboratory, Pasadena, California, 1952), Report 26–4.

[3]A. Prosperetti, "Bubble Phenomena in Sound Fields: Part One," *Ultrasonics* **22**, 69–77 (1984).

[4]Lord Rayleigh, "On the Pressure Developed in a Liquid during the Collapse of a Spherical Cavity," *Phil. Mag.* **34**, 94–98 (1917).

[5]B. E. Noltingk and E. A. Neppiras, "Cavitation Produced by Ultrasonics," *Proc. Phys. Soc. B (London)* **63B**, 674–683 (1950).

[6]E. A. Neppiras and B. E. Noltingk, "Cavitation Produced by Ultrasonics: Theoretical Conditions for the Onset of Cavitation," *Proc. Phys. Soc. B (London)* **64B**, 1032–1038 (1951).

[7]P. M. Morse, *Vibration and Sound* (Acoustical Society of America, American Institute of Physics, New York, 1981), 2nd ed., Chap. 7, pp. 311–325.

[8]R. H. Cole, *Underwater Explosions* (Princeton University Press, Princeton, New Jersey, 1948).

[9]M. S. Plesset and A. Prosperetti, "Bubble Dynamics and Cavitation," *Ann. Rev. Fluid Mech.* **9**, 145–185 (1977).

[10]F. R. Young, *Cavitation* (McGraw–Hill Book Company, London, 1989), Chap. 2, pp. 8–37.

[11]K. A. Naugol'nykh and N. A. Roi, *ELEKTRICHESKIE RAZRJADY V VODE* (Nauka, Moskva, 1971) [English transl.: *Spark Discharges in Water* (Applied Research Laboratories, The University of Texas at Austin, 1987), Internal Report].

[12]E. A. Neppiras, "Acoustic Cavitation," *Physics Reports* **61**(3), 159–251 (1980).

[13]A. G. Ryabinin and G. A. Ryabinin, "Gas-Bubble Energy in an Underwater Electrical Discharge," *Zh. Tekh. Fiz.* **46**, 881–884 (1976) [English transl.: *Sov. Phys. Tech. Phys.* **21**(4), 512–514 (1976)].

[14]G. A. Khoroshev, "Collapse of Vapor-Air Cavitation Bubbles," *Akust. Zh.* **9**(3) 340–346 (1963) [English transl.: *Sov. Phys. Acoust.* **9**(3), 275–279 (1964)].

[15]R. L. Rogers, *Intermediate Energy Tests and Analysis of a Plasma Sound Source* (Applied Research Laboratories, The University of Texas at Austin, 1992), Report ARL–TR–92–15.

[16]R. H. Mellen, *An Experimental Study of the Collapse of a Spherical Cavity in Water* (U. S. Navy Underwater Sound Laboratory, New London, Connecticut, 1955), Research Report 279.

[17]D. C. Gibson, "The Pulsation Time of Spark Induced Vapor Bubbles," *Trans. ASME, J. Basic Eng.* **94**, 248–249 (1972).

3. MODEL

An overview of the model developed in this chapter was given in Sec. 1.5. A complete model for the spark-generated bubble is introduced in this chapter. The model describes the large amplitude radial oscillations of an isolated spherical bubble containing water vapor and plasma when compressibility effects are important. The equations of bubble dynamics are adaptations of equations developed in the literature. A model that describes how multiple bubbles interact with one another will be presented in Chap. 4. The other bubbles were presumed to influence the bubble of interest through their radiated pressure signatures. Each pressure signature will be incident from one side of the bubble and will propagate across the bubble, so the equations of dynamics were modified to account for this physical situation.

The model for the isolated spark-generated bubble has several features. The energy flow as a result of processes such as electromagnetic radiation and mass flow is considered. Radiation is assumed to be blackbody radiation, and the attenuation properties of water as a function of wavelength are used to determine an approximate radiative transfer from the bubble. The bubble contents are assumed to be homogeneous and in thermodynamic equilibrium. Besides being a heat loss, electromagnetic radiation deposited near the bubble wall may bring mass into the

bubble. Mass flow from evaporation and condensation is modeled according to the kinetic theory equation for mass flow developed by Schrage[1] in 1953. The energy balance equations are discussed and new terms are added to describe the pertinent features of the spark-generated bubbles. Heat conduction to the water is neglected.

3.1 Equations of Bubble Dynamics

The bubbles created by spark discharges share many characteristics with cavitation bubbles, because they are essentially vapor bubbles, without any noncondensable gas inside. Many papers have been published describing the dynamics of single isolated gas bubbles and cavitation bubbles in a compressible fluid. The papers of Herring[2] and Trilling[3] discuss gas bubbles in a compressible liquid, as do those of Gilmore[4] and Flynn.[5] An interesting discussion was published by Lastman and Wentzell,[6] comparing five of the available models. The recent work by Fujikawa and Akamatsu[7] and Shima and Tomita[8] add a number of terms that greatly complicate the equations. The model developed by Keller and Miksis[9] for the bubble dynamics is put on firmer footing by Prosperetti[10,11] and Lezzi.[12] These models are a good place to start in describing spark-generated bubbles.

The equations of bubble dynamics to be used for the modeling are the set of equations developed by A. Lezzi and A. Prosperetti in 1986 and 1987.[11,12] These equations are developed as perturbation solutions of the partial differential equations governing motion in a compressible liquid. This approach is a more rigorous extension of the mathematical formulation proposed and developed by Keller and several others.[9,13,14] The two papers by Lezzi and Prosperetti develop

approximate equations of motion for the bubble radius to first and second order in the bubble wall mach number. The equivalence of the large number of equations of bubble dynamics available in the literature is discussed. In particular, the equations developed are not unique. Instead, a one-parameter family of equations of motion for the bubble wall is found to exist at first order, and a two-parameter family is found at second order. An important part of developing an equation of bubble dynamics is determining the parameters in these equations. This is accomplished by comparing the solutions of the equations of bubble dynamics to the numerical results obtained by solving the complete partial differential equations by the method of characteristics. Forms of the first and second order equations that agreed most closely with this exact solution are given in the conclusion of the second paper by Lezzi and Prosperetti, and will be given below. The first order equation given is very similar to the equation given by Keller and Miksis, which is in turn a further development of the equation given by Keller and Kolodner. Following the derivation of the Keller equation is helpful in understanding the general approach taken by Lezzi and Prosperetti, without the cumbersome details of the complete perturbation method.

The development followed in the previous chapter led to the following equations for the continuity and momentum equations accurate to order c_∞^{-2}:

$$\nabla^2\varphi+\frac{1}{\rho_\infty c_\infty^2}\left(\frac{\partial p}{\partial t}+\frac{\partial\varphi}{\partial r}\frac{\partial p}{\partial r}\right)=0 \tag{2.26}$$

$$\frac{\partial\varphi}{\partial t}+\frac{1}{2}(\nabla\varphi)^2+\frac{p-p_\infty}{\rho_\infty}\left(1-\frac{p-p_\infty}{2\rho_\infty c_\infty^2}\right)=0 \quad . \tag{2.27}$$

Near the bubble, the finite sound speed is unimportant, because the propagation times are much smaller than the time scale associated with the motion of the bubble

boundary (τ). The liquid behaves as if it were incompressible, and $c_\infty \to \infty$. The continuity and Bernoulli equations in the nearfield then become

$$\nabla^2\varphi = 0 \tag{3.1}$$

$$\frac{\partial\varphi}{\partial t} + \frac{1}{2}(\nabla\varphi)^2 + \frac{p - p_\infty}{\rho_\infty} = 0 \quad . \tag{3.2}$$

Besides disregarding the finite speed of propagation, this nearfield formulation also neglects the compression energy stored in the liquid through a change in liquid density (second-order and higher terms in the Bernoulli equation). This effect will be unimportant near the bubble, because the kinetic energy and the "pressure energy" (the first term in the expansion for the enthalpy) are large compared to the compression energy. Far from the bubble, the finite propagation speed cannot be ignored. Nonlinear effects are expected to be small, however, so a linearized form of these equations is sufficient in the farfield:

$$\nabla^2\varphi + \frac{1}{\rho_\infty c_\infty^2}\frac{\partial p}{\partial t} = 0 \tag{3.3}$$

$$\frac{\partial\varphi}{\partial t} + \frac{p - p_\infty}{\rho_\infty} = 0 \quad . \tag{3.4}$$

Taking the time derivative of Eq. (3.4) and using Eq. (3.3) to eliminate p leads directly to the wave equation:

$$\nabla^2\varphi - \frac{1}{c_\infty^2}\frac{\partial^2\varphi}{\partial t^2} = 0 \quad . \tag{3.5}$$

The approach taken by Keller was to find an approximate equation of motion for the bubble wall using a model formulation valid simultaneously in the nearfield and the farfield. This was done by using the wave equation (Eq. (3.5)) with the incompressible Bernoulli integral (Eq. (3.2)). The wave equation is correct in the farfield, and its difference from the nearfield continuity equation in the

nearfield is negligible. In the same way, the nearfield form of the Bernoulli integral differs from the farfield form by the term $(\nabla\varphi)^2$, which has already been assumed small in the farfield. The following discussion is a derivation of the equation developed in the paper by Keller and Miksis, except that the terms involving the viscosity and surface tension have been dropped from the equations of bubble dynamics because they are small.

The wave equation implies a velocity potential that is the sum of an outward propagating wave function (f) and an inward propagating wave function (g):

$$\varphi(r,t)=\frac{f(t-r/c_\infty)}{r}+\frac{g(t+r/c_\infty)}{r} \quad . \tag{3.6}$$

Derivatives of φ are given by

$$\frac{\partial\varphi(r,t)}{\partial t}=\frac{f'(t-r/c_\infty)}{r}+\frac{g'(t+r/c_\infty)}{r} \tag{3.7}$$

$$\frac{\partial\varphi(r,t)}{\partial r}=\frac{g'(t+r/c_\infty)}{rc_\infty}-\frac{f'(t-r/c_\infty)}{rc_\infty}-\frac{\varphi(r,t)}{r} \quad . \tag{3.8}$$

The kinematic boundary condition at the bubble wall was given previously by

$$u\big|_{r=R}=\left.\frac{\partial\varphi}{\partial r}\right|_{r=R}=\dot{R} \quad . \tag{2.8}$$

The nearfield Bernoulli integral (Eq. (3.2)) is then evaluated at the bubble wall, and the kinematic boundary condition is used to simplify the expression. The resulting equation is the following:

$$\frac{p_B(t)-p_\infty}{\rho_\infty}=-\left.\frac{\partial\varphi}{\partial t}\right|_{r=R}-\frac{\dot{R}^2}{2} \quad . \tag{3.9}$$

Equation (3.8) can be used to eliminate the arbitrary function f in Eq. (3.7):

$$\frac{\partial\varphi(r,t)}{\partial t}=\frac{2g'(t+r/c_\infty)}{r}-c_\infty\frac{\partial\varphi(r,t)}{\partial r}-c_\infty\frac{\varphi(r,t)}{r} \quad . \tag{3.10}$$

Substituting this expression into Eq. (3.9) and using Eq. (2.8) yields

$$R\frac{p_B(t)-p_\infty}{\rho_\infty}=c_\infty R\dot{R}-2g'(t+R/c_\infty)+c_\infty\varphi(R,t)-\frac{R\dot{R}^2}{2} \quad . \tag{3.11}$$

The total time derivative of the velocity potential at $r=R$ can be written (using Eqs. (2.8) and (3.9)) as:

$$\frac{d\varphi(R,t)}{dt}=\left.\frac{\partial\varphi(r,t)}{\partial t}\right|_{r=R}+\dot{R}^2=\frac{\dot{R}^2}{2}-\frac{p_B(t)-p_\infty}{\rho_\infty} \quad . \tag{3.12}$$

Taking the total time derivative of Eq. (3.11), using Eq. (3.12) to eliminate φ, and collecting terms, a form of the equation of bubble dynamics is found:

$$\left(1-\frac{\dot{R}}{c_\infty}\right)R\ddot{R}+\frac{3}{2}\left(1-\frac{\dot{R}}{3c_\infty}\right)=$$
$$\left(1+\frac{\dot{R}}{c_\infty}\right)\left[\frac{p_B(t)-p_\infty}{\rho_\infty}+\frac{2g''(t+R/c_\infty)}{c_\infty}\right]+\frac{R}{c_\infty}\frac{\dot{p}_B(t)}{\rho_\infty} \quad . \tag{3.13}$$

This is the Keller form of the equation of bubble dynamics. The function g is determined by assuming the bubble is in an incident sound field with velocity potential $\Phi(\vec{x},t)$, where $\vec{x}=\vec{x}_i$ is the center of the i'th bubble. $\Phi(\vec{x},t)$ can be written as a sum of spherically symmetric and antisymmetric parts:

$$\Phi(\vec{x},t)=\Phi_s(\vec{x},t)+\Phi_a(\vec{x},t) \quad . \tag{3.14}$$

The symmetric part can be written as

$$\Phi_s(\vec{x},t)=\frac{g(t+r/c_\infty)+h(t-r/c_\infty)}{r};\qquad r=|\vec{x}-\vec{x}_i| \quad . \tag{3.15}$$

If $\Phi(\vec{x},t)$ is regular at $\vec{x}=\vec{x}_i$, then $h=-g$. Since the antisymmetric part must vanish at the center of the bubble,

$$\Phi(\vec{x}_i,t)=\lim_{r\to 0}\frac{g(t+r/c_\infty)-g(t-r/c_\infty)}{r}$$
$$=\frac{1}{c_\infty}\lim_{r/c_\infty\to 0}\frac{g(t+r/c_\infty)-g(t-r/c_\infty)}{r/c_\infty}\equiv\frac{2g'(t)}{c_\infty} \quad , \tag{3.16}$$

where g' denotes the derivative of g with respect to its argument. Therefore, the function g can be found in terms of the velocity potential of the incident sound field:

$$\Phi(\vec{x}_i,t)=\frac{2g'(t)}{c_\infty} \quad \Rightarrow \quad \frac{2g''(t)}{c_\infty}=\frac{\partial\Phi(\vec{x}_i,t)}{\partial t} \quad . \tag{3.17}$$

The sound field pressure is related to the velocity potential by[15]

$$\frac{p(\vec{x},t)-p_\infty}{\rho_\infty}=-\frac{\partial\Phi(\vec{x},t)}{\partial t} \quad . \tag{3.18}$$

The function g can then be written in terms of the pressure of the incident sound field, where $p_v(\vec{x}_i,t)$ is introduced to represent the variable part of the liquid pressure at the center of the bubble in the absence of the bubble:

$$\frac{2g''(t)}{c_\infty}=-\frac{p(\vec{x}_i,t)-p_\infty}{\rho_\infty}\equiv-\frac{p_v(\vec{x}_i,t)}{\rho_\infty} \quad . \tag{3.19}$$

With this substitution, the Keller equation of bubble dynamics becomes

$$\left(1-\frac{\dot{R}}{c_\infty}\right)R\ddot{R}+\frac{3}{2}\left(1-\frac{\dot{R}}{3c_\infty}\right)\dot{R}^2 = \left(1-\frac{\dot{R}}{c_\infty}\right)\left[\frac{p_B(t)-p_\infty}{\rho_\infty}-\frac{p_v(\vec{x}_i,t+R/c_\infty)}{\rho_\infty}\right]+\frac{R}{c_\infty}\frac{\dot{p}_B(t)}{\rho_\infty} \quad . \tag{3.20}$$

As was mentioned previously, Lezzi and Prosperetti found a one-parameter family of equations of bubble dynamics to exist at first order, which they referred to as the general Keller-Herring equation:

$$\left(1-(\beta+1)\frac{\dot{R}}{c_\infty}\right)R\ddot{R}+\frac{3}{2}\left(1-(3\beta+1)\frac{\dot{R}}{3c_\infty}\right)\dot{R}^2 = \left(1+(1-\beta)\frac{\dot{R}}{c_\infty}+\frac{R}{c_\infty}\frac{\mathrm{d}}{\mathrm{d}t}\right)\left(h_B-\frac{p_v(t)}{\rho_\infty}\right) \quad . \tag{3.21}$$

The parameter β in this equation is a numerical constant of order unity, and represents the indeterminacy present in the first order equation because the algebraic manipulations to get to a final equation of bubble dynamics are not unique. A value of $\beta = 1$ leads to the Herring form of the equation of bubble dynamics. An optimal value of $\beta = 0$ was determined by comparing the solutions of this equation to the numerical solutions of the partial differential equations. With this value of θ, the general Keller-Herring equation takes the Keller form:

$$\left(1-\frac{\dot{R}}{c_\infty}\right)R\ddot{R}+\frac{3}{2}\left(1-\frac{\dot{R}}{3c_\infty}\right)\dot{R}^2=\left(1+\frac{\dot{R}}{c_\infty}+\frac{R}{c_\infty}\frac{\mathrm{d}}{\mathrm{d}t}\right)\left(h_B-\frac{p_v(t)}{\rho_\infty}\right) \quad . \qquad (3.22)$$

This first order equation was determined by Lezzi and Prosperetti to be valid up to bubble wall mach numbers of about 0.5. Unless the mach number exceeds this value, or the pressure inside the bubble exceeds about 5000 times the undisturbed value in the liquid, it should give good results.

The Keller equation was developed here from the continuity and Bernoulli equations accurate to order c_∞^{-2}, in keeping with the original papers, but the equation given by Lezzi and Prosperetti is written explicitly in terms of the enthalpy. The equations using the enthalpy directly are preferred to equations written in terms of the pressure. This is because the order of $(p-p_\infty)/\rho_\infty$ in the enthalpy expansion (Eq. (2.24)) must be small if the first term is to be a good approximation for the enthalpy. The incompressible Bernoulli integral (Eq. (3.2)) shows, however, that near the minimum radius of the bubble, the order of this term is set not by the square of the particle velocity, but by the term $\partial\varphi/\partial t$, which may be large. Using the enthalpy directly avoids this problem. The equation given by Gilmore based on the Kirkwood-Bethe approximation[16] also uses the enthalpy directly. Many authors

have used this equation to good effect for the bubbles generated by cavitation,[17,18] explosions,[19] air guns,[20] and sparks.[21,22,23] Although this equation contains some second order terms, it is not formally consistent to second order,[7,24] and it was found by Lezzi and Prosperetti to be a poorer approximation than the first order equation given here. The reason for its success appears to be its use of the enthalpy directly, and it is found to be superior to the Keller form of the first order equation when that equation is written in terms of the pressure. The Gilmore equation is not suited for use in multiple bubble studies, as the assumption is explicitly made in its derivation that no pressure waves travel towards the bubble.[10]

The two equations of bubble dynamics above (Eqs. (3.20) and (3.22)) show the terms concerning the variable pressure in slightly different forms. The two formulations are essentially equivalent. The portion of the right hand side describing the variable pressure and its derivative in Eq. (3.22) is given by

$$r.h.s.=\ldots-\frac{1}{\rho_\infty}\left[\left(1+\frac{\dot{R}}{c_\infty}\right)p_v(t)+\frac{R}{c_\infty}\frac{dp_v(t)}{dt}\right] \quad . \tag{3.23}$$

The pressure in this equation $\left(p_v(t)\right)$ is the liquid pressure at the center of the bubble. If this pressure is written in the same form as it was in the derivation of the Keller equation, this expression takes the form

$$r.h.s.=\ldots-\frac{1}{\rho_\infty}\left[\left(1+\frac{\dot{R}}{c_\infty}\right)p_v(\vec{x}_i,t)+\frac{R}{c_\infty}\frac{dp_v(\vec{x}_i,t)}{dt}\right] \quad . \tag{3.24}$$

The expression in Eq. (3.20) for the variable part of the pressure can be approximated to first order as:

$$p_v(\vec{x}_i,t+R/c_\infty)\cong p_v(\vec{x}_i,t)+\frac{R}{c_\infty}\frac{dp_v(\vec{x}_i,t)}{dt} \quad . \tag{3.25}$$

When this is substituted into Eq. (3.20), the right hand side of the equation is

given by

$$r.h.s. \equiv \ldots - \frac{1}{\rho_\infty}\left(1+\frac{\dot{R}}{c_\infty}\right)\left[p_v(\vec{x}_i,t)+\frac{R}{c_\infty}\frac{dp_v(\vec{x}_i,t)}{dt}\right]$$

$$\equiv \ldots - \frac{1}{\rho_\infty}\left[\left(1+\frac{\dot{R}}{c_\infty}\right)p_v(\vec{x}_i,t)+\frac{R}{c_\infty}\frac{dp_v(\vec{x}_i,t)}{dt}+R\frac{\dot{R}}{c_\infty^2}\frac{dp_v(\vec{x}_i,t)}{dt}\right] \quad . \qquad (3.26)$$

This last form shows that the differences between the variable pressure terms in Eqs. (3.20) and (3.22) are of second order. To first order then, these expressions are identical.

The equations above demonstrate that the time derivatives of the variable pressure in the equations of dynamics are present to evaluate the incoming spherical pressure wave at the advanced time $(t+R/c_\infty)$. In this study, the incoming pressure waves will originate from other bubbles that oscillate approximately in phase with the bubble under consideration (see Fig. 3.1). The pressure will propagate past the bubble, from one side to the other. The variable pressure at a given bubble will not be constant across the bubble because the amplitude and phase of the incoming pressure wave depend on the radial distance from the bubble that radiated. In Sec. 5.2, an average variable pressure is determined. For the farfield term, the average variable pressure is the pressure evaluated at the center of the

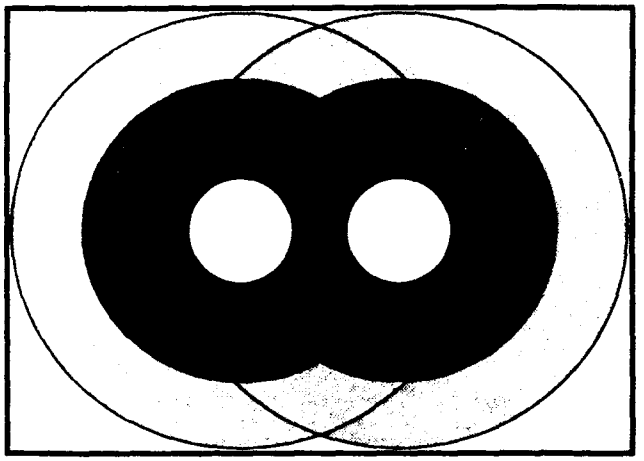

FIGURE 3.1 AS-93-271
PRESSURE PROPAGATION

bubble. An expression is given for the afterflow term of the average variable pressure that reduces to the value at the center of the bubble when the bubble separation is sufficiently large. The variable pressure will therefore be evaluated at the center of the bubble, and the time derivative term should be dropped from the variable pressure expression.

Dropping the time derivative term in the overpressure, and making the substitution for the variable pressure, the first order equation of bubble dynamics becomes:

$$\left(1-\frac{\dot{R}}{c_\infty}\right)R\ddot{R}+\frac{3}{2}\left(1-\frac{\dot{R}}{3c_\infty}\right)\dot{R}^2=\left(1+\frac{\dot{R}}{c_\infty}\right)\left(h_B-\frac{p_v(\vec{x}_i,t)}{\rho_\infty}\right)+\frac{R}{c_\infty}\dot{h}_B \quad . \qquad (3.27)$$

This equation is integrated simultaneously with the equations describing the interior of the bubble (derived in the next section) to find the time evolution of the bubble radius and the bubble wall velocity.

Although only the first order equation of bubble dynamics has been discussed here, a second order equation of bubble dynamics was also developed in the papers by Lezzi and Prosperetti:[12]

$$\left(\frac{R}{c_\infty}\ddot{R}\right)^2+\left[1-\frac{3}{2}\frac{\dot{R}}{c_\infty}\left(1-\frac{38}{15}\frac{\dot{R}}{c_\infty}\right)\right]R\ddot{R}+\frac{3}{2}\left[1-\frac{5}{6}\frac{\dot{R}}{c_\infty}\left(1-\frac{52}{25}\frac{\dot{R}}{c_\infty}\right)\right]\dot{R}^2=$$
$$\left(1+\frac{\dot{R}}{2c_\infty}\right)\left[h_B-\frac{p_v(t)}{\rho_\infty}\right]+\frac{\dot{R}}{c_\infty}\left(1-\frac{3}{2}\frac{\dot{R}}{c_\infty}\right)\frac{d}{dt}\left[h_B-\frac{p_v(t)}{\rho_\infty}\right]$$
$$+\frac{1}{c_\infty^2}\frac{d}{dt}\left[g_2-R^2\frac{d}{dt}\frac{p_v(t)}{\rho_\infty}\right] \quad . \qquad (3.28)$$

This expression is quadratic in the bubble wall acceleration and accurate to second order in the bubble wall mach number $(\dot{R}/c_\infty)$. While a one-parameter family of equations was found to exist at first order, the second order equation has two levels

of indeterminacy. The equation given here matches the numerical solutions most closely.

This equation is discussed in more detail in Appendix B, and was used to verify the results from the first order equation in the case of an isolated bubble. The first and second order equations did not give significantly different results for any of the discharges considered in this study. It is likely that conditions could be chosen such that the second order equation would be required, but this has not been explored.

The liquid equation of state is taken to be a pressure-density relationship of the modified Tait form[19]

$$\frac{p+B}{p_\infty+B}=\left(\frac{\rho}{\rho_\infty}\right)^n; \qquad \begin{matrix} n=7.15 \\ B=304{,}913{,}000 \text{ Pa} \end{matrix} \tag{3.29}$$

From the previous equation for the sound speed (Eq. (2.23)) and this equation of state,

$$c^2=\frac{n(p+B)}{\rho}=c_\infty^2+(n-1)h \quad , \tag{3.30}$$

where the sound speed in the undisturbed liquid (c_∞^2) can now be given by

$$c_\infty^2=\frac{n(p_\infty+B)}{\rho_\infty} \quad . \tag{3.31}$$

The specific enthalpy in the liquid is given by

$$h=\frac{c^2-c_\infty^2}{n-1}=\frac{c_\infty^2}{n-1}\left[\left(\frac{p+B}{p_\infty+B}\right)^{\frac{n-1}{n}}-1\right] \quad . \tag{3.32}$$

The liquid pressure at the bubble wall is given by the condition on the normal

stresses, where P is the internal pressure of the bubble:

$$p_B(t) = P - \frac{1}{R}\left(2\sigma + 4\mu\dot{R}\right) \tag{3.33}$$

$$\sigma = 0.072 \text{ N/m} \tag{3.34}$$

$$\mu = 0.001 \text{ Pa}\cdot\text{s} \quad . \tag{3.35}$$

It should be noted here that the equation for the liquid pressure contains the surface tension (σ) and viscosity (μ), while these terms were dropped in the equation of bubble dynamics. The reason for this is that in the equation for the dynamics these terms are always negligible, while in the liquid pressure equation these terms may not be negligible for small bubbles. The specific enthalpy at the bubble wall is found by evaluating the specific enthalpy at the bubble wall liquid pressure

$$h_B = \frac{c_\infty^2}{n-1}\left[\left(\frac{p_B + B}{p_\infty + B}\right)^{\frac{n-1}{n}} - 1\right] \quad . \tag{3.36}$$

We can use the equation for the specific enthalpy at the bubble wall to find an expression for $\dot{h}_B$ in terms of the other variables:

$$\dot{h}_B \equiv \frac{\mathrm{d}}{\mathrm{d}t}h_B = \frac{c_\infty^2}{n-1}\left[\frac{n-1}{n}\left(\frac{p_B + B}{p_\infty + B}\right)^{\frac{n-1}{n}} \frac{\dot{p}_B}{p_B + B}\right]$$

$$= \frac{\dot{p}_B}{p_B + B}\left[\frac{n-1}{n}h_B + \frac{c_\infty^2}{n}\right] \quad . \tag{3.37}$$

The expression for $\dot{p}_B$ is found by taking the time derivative of Eq. (3.33)

$$\dot{p}_B = \dot{P} - \frac{4\mu}{R}\ddot{R} + \frac{\dot{R}}{R^2}\left(2\sigma + 4\mu\dot{R}\right) \quad . \tag{3.38}$$

It will be necessary to use conservation of energy to determine a relation for the pressure inside the bubble. It will also be necessary to assume an equation of state for the vapor, i.e., the ideal gas law.

The equations of dynamics should be examined to determine what modifications might be made as a result of the movement of the bubble boundary due to mass flow. Assume that the specific total mass flow is given by $\dot{m}_T$. Then the velocity of the boundary as a result of mass flow is given by:

$$\dot{R}_M = \frac{\dot{m}_T}{\rho_\infty} \quad . \tag{3.39}$$

The following expressions then describe the terms in the equations of dynamics:

$$\dot{R}_T = \dot{R} + \dot{R}_M \quad . \tag{3.40}$$

$$\dot{R}_T = \dot{R}_{Total} \qquad \dot{R} = \dot{R}_{Dynamics} = \left(\frac{\partial \phi}{\partial r}\right)_{r=R} \qquad \dot{R}_M = \dot{R}_{Massflow} \quad . \tag{3.41}$$

The matching conditions used to derive the equation of bubble dynamics assume that $\dot{R}$ will be used, and that equation then gives $\ddot{R}$. The desired bubble wall velocity and acceleration are $\dot{R}_T$ and $\ddot{R}_T$, which are given by (assuming an incompressible fluid)

$$\dot{R}_T = \dot{R} + \frac{\dot{m}_T}{\rho_\infty} \tag{3.42}$$

$$\ddot{R}_T = \ddot{R} + \frac{\ddot{m}_T}{\rho_\infty} \quad . \tag{3.43}$$

A comparison of the terms in these equations was made to determine whether the additional complications in the equations of dynamics were warranted for the regimes examined. It was determined that the additional terms due to mass flow were of lower magnitude than the errors in the estimates that were made in other parts of the model, and they were neglected. These terms were included in a bubble collapse study performed by Fujikawa and Akamatsu.[7]

3.2 Blackbody Radiation

When the electrical energy is deposited into the water, a plasma is created in the water.[25,26] This plasma inside the bubble cools as the bubble expands, and is heated again when the bubble collapses. Because of the high temperatures inside the bubble at these times, a consideration of the electromagnetic radiation from the bubble is necessary.

The radiation from low pressure gas discharges generally consists of spectral lines, bremsstrahlung, and continuous recombination radiation. As the pressure increases, the spectral lines broaden and the portion of the radiation due to recombination increases, so that the radiation becomes continuous. The experimental evidence indicates that the spark-generated bubble might be expected to radiate with the spectral distribution of a blackbody, if the internal pressure is greater than about 20 MPa. If this distribution is to be established, the contents of the bubble must be in equilibrium, and the photon mean free path must be small compared to the size of the bubble.

Preliminary numerical simulations indicated that electromagnetic radiation from the bubble would have to be considered in a model of the spark-generated bubble. The equations developed here describe the electromagnetic radiation from the bubble, assuming blackbody radiation from a homogeneous spherical radiator. The contents of the bubble were presumed to radiate according to the Stefan-Boltzmann Law. The total radiation from the bubble is given by[27]

$$F_{BB} = 4\pi R^2 \varepsilon f_{BB} \tag{3.44}$$

$$f(T) \equiv \int_0^\infty \Phi(\lambda, T)\, d\lambda = \sigma_{BB} T^4 \tag{3.45}$$

$$f_{BB} = f(T) - f(T_\infty) = \sigma_{BB}\left(T^4 - T_\infty^4\right) \tag{3.46}$$

$$\frac{1}{\varepsilon} = \frac{1}{\varepsilon_{water}} + \frac{1}{\varepsilon_{sphere}} - 1 \qquad \varepsilon_{water} \cong 0.65 \quad . \tag{3.47}$$

In this equation, the factors ε_{water} and ε_{sphere} are the emissivities of the water and spherical bubble, while ε is the total emissivity. The absorption (and therefore the emissivity) has been calculated[28] for a spherical radiator of radius R and is given as:

$$\varepsilon_{sphere} = 1 - \frac{1}{2}\left(\frac{\ell(\nu)}{R}\right)^2\left[1 - \left(1 + \frac{2R}{\ell(\nu)}\right)\exp\left(\frac{-2R}{\ell(\nu)}\right)\right] \quad , \tag{3.48}$$

where $\ell(\nu)$ is the frequency dependent photon mean free path, and R is the radius of the sphere. Using the emissivity in this form requires an integration over frequency at each time step. Instead of performing this integration, the frequency dependent photon mean free path will be replaced by a frequency averaged mean free path. A frequency dependent weighting must be chosen to calculate the average mean free path. An analysis was performed on the model output before the blackbody radiation part of the model was implemented. This allowed a determination of the effects that radiation might have in the model, and indicated what portions of the acoustic signature it might affect. Equations are available in the literature to calculate the mean free path as a function of the thermodynamic variables in the bubble. When the mean free path is very small compared to the size of the bubble, the bubble is considered optically thick, and when the mean free path is very large compared to the size of the bubble, the bubble is considered optically thin.[29] An inspection of the mean free path at several points in the bubble evolution indicated that it varied over several orders of magnitude. The bubble was found to be optically thick when the bubble radius was small and the temperature high. The same analysis showed that almost all the blackbody radiation that would be radiated would have been radiated at these times, because of the strong

temperature dependence in the Stefan-Boltzmann Law. The restrictions outlined above also require an optically thick body for the assumption of blackbody radiation to be valid. This preliminary analysis indicated that a frequency weighting assuming an optically thick body would be appropriate. The Rosseland weighting assumes an optically thick body, and gives the following average photon mean free path:

$$\ell_R = C\frac{T^2 m_w}{\rho}\exp\left(\frac{I}{k_B T}\right) \tag{3.49}$$

$$m_w = 3\times10^{-26}\,\text{kg} \qquad C = 9\times10^{10}(\text{meters}\,^\circ\text{K})^{-2} \tag{3.50}$$

$$I = 13.6\ \text{eV} \qquad k_B = 1.38066\times10^{-23}\ \text{J}/^\circ\text{K} \quad . \tag{3.51}$$

The emissivity of a spherical radiator is then given approximately by

$$\varepsilon_{\text{sphere}} \approx 1-\frac{1}{2}\left(\frac{\ell_R}{R}\right)^2\left[1-\left(1+2\frac{R}{\ell_R}\right)\exp\left(\frac{-2R}{\ell_R}\right)\right] \quad . \tag{3.52}$$

3.3 Mass Flow

The mass flow into the bubble is composed of two portions, which are assumed to operate independently and simultaneously:

1. Mass influx from heating and evaporation via blackbody radiation $(\dot{m}_{BB})$.
2. Mass exchange from evaporation and condensation $(\dot{m}_E)$.

The total specific mass flow is the sum of these two mass flows:

$$\dot{m}_T = \dot{m}_{BB} + \dot{m}_E \quad . \tag{3.53}$$

It is related to the total mass flow by the relation:

$$\dot{M} = 4\pi R^2 \dot{m}_T \quad . \tag{3.54}$$

It is assumed that blackbody radiation will bring mass into the bubble by depositing a portion of the total radiated power near the bubble wall. This radiation will heat the surrounding water, changing it to water vapor that will find its way into the bubble. This vapor is assumed to come into the bubble at the evaporation temperature (which is a function of pressure). The amount of mass brought into the bubble depends on the amount of heat deposited in the water near the bubble. Energy deposited far from the bubble will probably not contribute significantly to bringing mass into the bubble, so energy deposited beyond a given dissipation length will be assumed lost to the surrounding water by the bubble contents in the energy balance equations. The proportion of the radiation dissipated is a complicated function of the layer thickness and bubble temperature. This function is difficult to determine, as it requires a consideration of the absorption coefficient. This absorption coefficient varies by many orders of magnitude over the frequency range of interest.[30] Rather than trying to determine the exact proportion of the radiation dissipated, an approximate method was used to compile a table from which estimated values of the necessary function could be interpolated. The following steps were taken:

1. Absorption coefficient for water (α) was plotted versus wavelength (λ).
2. Several wavelength ranges $(\lambda_1, \lambda_2)_i$ were chosen over which average values for the absorption coefficient $(\overline{\alpha}_i)$ were easily determined.
3. Blackbody spectrum was integrated numerically for several temperatures over each of these ranges:

$$f\left((\lambda_1,\lambda_2)_i,T\right)=\int_{(\lambda_1)_i}^{(\lambda_2)_i}\Phi(\lambda,T)\,d\lambda \qquad f\left((0,\infty),T\right)=\sigma_{BB}T^4\equiv f(T) \quad . \qquad (3.55)$$

4. A number of dissipation lengths (x) were chosen to be examined.

5. The total power dissipated in each dissipation length was determined from:

$$P_{\text{dissipated}}(x,T) = \sum_i \left(1 - e^{-\bar{\alpha}_i x}\right) f\left((\lambda_1,\lambda_2)_i, T\right) \quad . \tag{3.56}$$

6. The total dissipated power in a given dissipation length was normalized by the total power radiated to give the proportion of radiation dissipated:

$$\Pi(x,T) = P_{\text{dissipated}}(x,T)/f(T) \quad . \tag{3.57}$$

7. The results obtained over a range of temperatures and dissipation lengths were compiled into a table.

8. The percentage of dissipated power was calculated at a given temperature and dissipation length by linearly interpolating within this table.

These steps were carried out for temperatures ranging from 100 - 100,000°K, and for dissipation lengths ranging from 1 - 100,000 angstroms. The results are shown in Fig. 3.2. Experimental work performed by Robinson[31] indicated that about 30% of the radiation would be trapped near the surface of the bubble, based on the portion of the radiation in the ultraviolet band.

The mass flow into the bubble as a result of blackbody radiation is determined by assuming that blackbody radiation heats water up through the phase transition to water vapor. Because the absorption and emissivity of the water vapor are very low when the vapor is cold, it is unlikely that the radiation contributes strongly to heating the vapor. The expression for the specific mass flow from heating and evaporation through blackbody radiation is then given as:

$$\dot{m}_{\text{BB}} = \frac{\Pi(x,T)\varepsilon f_{\text{BB}}}{c_{\text{pw}}(T_{\text{E}} - T_{\infty}) + L} \quad . \tag{3.58}$$

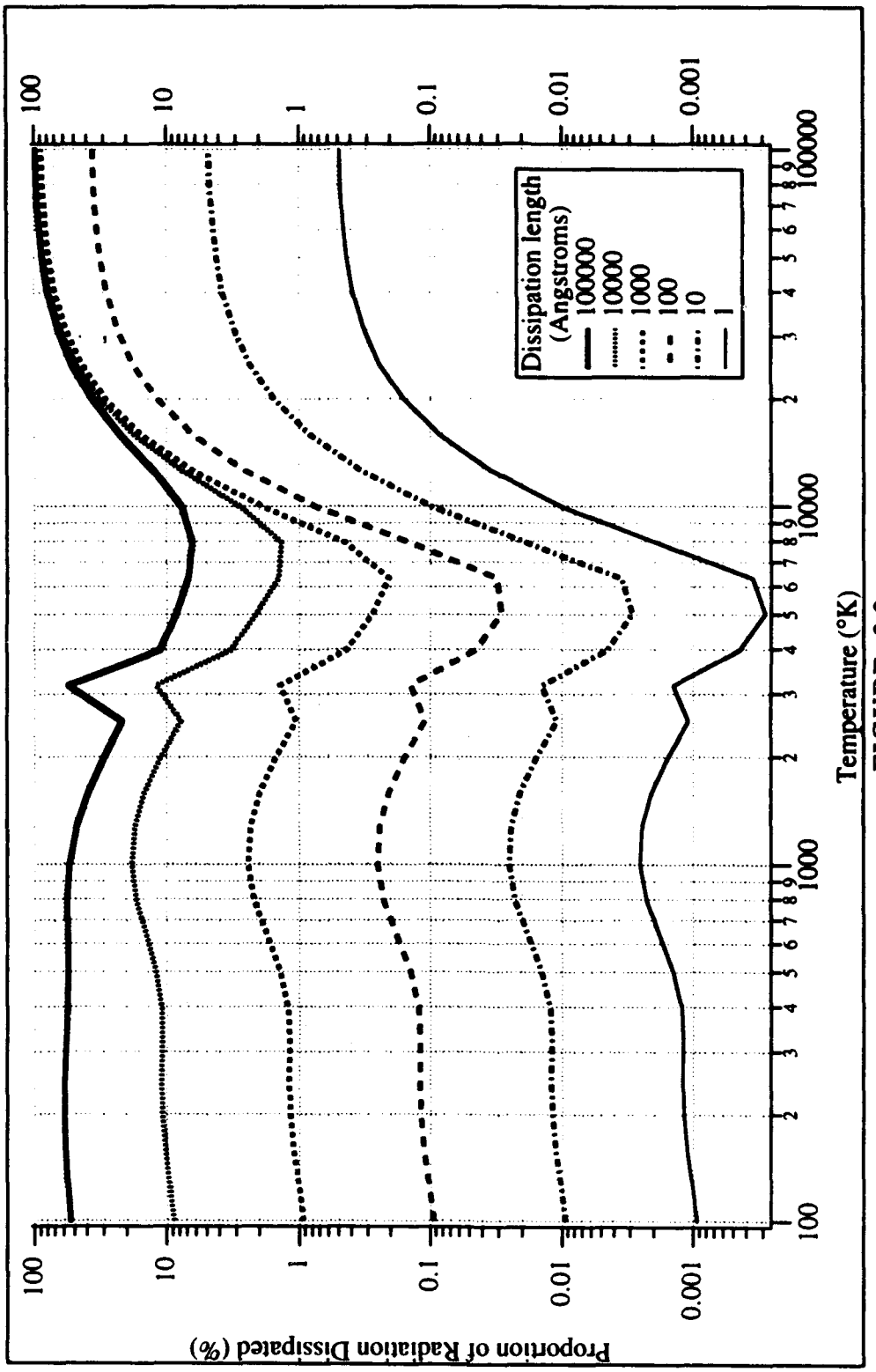

FIGURE 3.2
PROPORTION OF RADIATION DISSIPATED

AS-93-272

The specific heat capacity at constant pressure and latent heat of vaporization for water are given by:

$$c_{pw} = 4186 \text{ J/(kg·°K)} \qquad L = 2.25\times10^{6} \text{ J/kg} \quad . \tag{3.59}$$

The evaporation temperature is calculated from the following equation:

$$T_E = \frac{L}{g\Re \ln(p_0/p_\infty)} \qquad p_0 \equiv 4.8\cdot10^{10}\,\text{Pa} \quad . \tag{3.60}$$

The factor Π given in Eq. (3.57) gives the percentage of the total power radiated that brings mass into the bubble. The rest of the radiation is presumed to be radiated far away from the bubble. The heat loss from the bubble as a result of blackbody radiation is therefore:

$$q_{BB} = (1-\Pi) f_{BB} \quad . \tag{3.61}$$

The portion of the blackbody radiation that brings mass back into the bubble is not lost, since the mass that comes into the bubble has been heated from the ambient temperature up through the phase change. The energy required for this heating is returned to the bubble when the mass enters the bubble.

The specific mass flow as a result of evaporation and condensation is given by the kinetic theory equation for mass flow:[1]

$$\dot{m}_E = \frac{\alpha_M}{\sqrt{2\pi\Re}}\left[\frac{p^*}{\sqrt{T_\infty}} - \Gamma\frac{P}{\sqrt{T}}\right] \quad . \tag{3.62}$$

The symbols P and T are the pressure and temperature of the bubble contents, and T_∞ is the ambient temperature of the liquid. The equilibrium vapor pressure (p^*) is calculated from

$$p^* = p_0 \exp\left(\frac{-L}{\Re T_\infty}\right) \quad . \tag{3.63}$$

The accommodation coefficient will be discussed in Sec. 3.7. It can take on values ranging from zero to unity:

$$\alpha_M \qquad 0 \le \alpha_M \le 1 \tag{3.64}$$

$$\Gamma = 1 - \frac{\dot{m}_T}{2} \frac{\sqrt{T_\infty}}{p^*} \sqrt{2\pi \Re} \quad . \tag{3.65}$$

In these equations, Γ is a correction factor that compensates for the mass flow towards or away from the phase change interface, when the departure from equilibrium is assumed small. This factor describes the deviation of the velocity distribution from a Maxwellian distribution and is equal to unity for equilibrium conditions. Because the net mass flow contributes to the bulk velocity near the bubble wall, the total mass flow is used to calculate Γ. The simulations indicate for spark-generated bubbles that condensation dominates over evaporation because of the high pressures, and the mass flow due to evaporation and condensation is generally onto the bubble surface. The mass flow reaches its most negative values when the bubble is small and pressures are high. This is also when the blackbody mass flow reaches its largest values, and the blackbody mass flow therefore offsets much of the mass flow due to evaporation and condensation. The conclusion here is that the blackbody mass flow negates much of the mass migration towards the boundary. Because of these two opposing processes, Γ will be fixed at a value of unity in this study.

These expressions were developed for conditions near equilibrium, and the conditions in the bubble created by the spark discharge should be examined to determine if these equations will be strictly applicable. The contents of a vapor or gas bubble are generally considered to be in equilibrium if the bubble wall velocity

is less than the speed of sound in the gas.[7] This corresponds to a bubble wall mach number of about 0.3, assuming internal temperatures on the order of the ambient temperature. In fact, the internal temperatures are somewhat higher, which leads to a higher speed of sound in the gas. The bubble also contains some plasma, at least in the early stages of the bubble expansion. An analysis by Naugol'nykh and Roi[22] indicates that the bubble contents are very likely to be in equilibrium for this regime, also. This study has assumed that the bubble contents are in equilibrium, and the two referenced works tend to support that assumption.

The bubble contents are assumed to supply the heat to bring water from the ambient temperature through the phase transition and up to the temperature of the bubble. The heat removed from the bubble to heat this incoming mass serves to quench the high temperatures inside the bubble. Let the total mass flow quench (q_M) be given by the sum of two terms, one that describes the heating of the incoming water up through the phase change at the evaporation temperature (q_{Evap}), and one that describes the heating of the incoming vapor at constant pressure up to the temperature of the internal contents of the bubble (q_p):

$$q_M = q_{Evap} + q_p \quad . \tag{3.66}$$

Heat is removed from the bubble when mass comes into the bubble but is not added to the bubble when mass condenses on the bubble wall. This is because the heat in each case will flow to the coolest reservoir. This condition is written in the form:

$$r \quad \lceil 1,\ 0 \} \text{ for } \dot{m}_E \{>,\ <\} 0. \tag{3.67}$$

The current model assumes that the thermal conductivity of the water is sufficiently large that the temperature does not increase near the bubble wall as a result of the condensation. The amount of mass flow out of the bubble predicted by the model

indicates that this may be a poor approximation, and the temperature near the bubble wall probably does increase somewhat. The added heat would of course bring mass back into the bubble, either directly, as blackbody radiation does, or through a modification to the equilibrium pressure and the liquid temperature in the mass flow equation. These assumptions should be considered when the results are compared to the experimental data available The quench due to the heating and phase change of the water is given by:

$$q_{\text{Evap}} = (\dot{m}_{\text{BB}} + \zeta \dot{m}_{\text{E}})\left(c_{\text{pw}}(T_{\text{E}} - T_{\infty}) + L\right) \quad . \tag{3.68}$$

The quench due to the heating of the vapor is given by

$$q_{\text{p}} = (\dot{m}_{\text{BB}} + \zeta \dot{m}_{\text{E}}) \int_{T_{\text{E}}}^{T} c_{\text{p}}(T')\, \mathrm{d}T' \quad . \tag{3.69}$$

The specific heat capacity (c_{p}) written in Eq. (3.69) is generally a function of temperature.

3.4 Conservation of Energy

The contents of the spark-generated bubble have been assumed to be described by the pressure (P) and temperature (T). In this section, equations will be developed for $\dot{P}$ and $\dot{T}$ that will be integrated simultaneously with the equation of bubble dynamics. To understand the relation between pressure, temperature, mass flow, and heat flow, some simplifying assumptions will be made for the internal contents of the bubble. These assumptions are the following:

1. The pressure and temperature inside the bubble are uniform.
2. The bubble contents obey some form of the ideal gas law.
3. The bubble is filled with water vapor only, which may be dissociated.

4. A single average $\alpha(P,T)$ gives the degree of dissociation.

The function $\alpha(P,T)$ will range from 0 (no dissociation) to 1 (full dissociation), and the number of molecules from a single water molecule will range from one to three. The ideal gas law for water vapor takes the form

$$PV = Mg\Re T; \qquad g(\alpha) = 1+2\alpha \quad . \tag{3.70}$$

This form of the ideal gas law describes the varying constituents of the bubble, but still assumes the particles inside the bubble do not interact. The function $g(\alpha)$ describes the number of molecules in the bubble per original water molecule. The energy of an ideal gas (U), allowing dissociation but neglecting ionization, is given by:[22,32]

$$U = M\left[\alpha c_{v\_dis} T + (1-\alpha) c_{v\_H_2O} T + \alpha L_{dis}\right] \quad . \tag{3.71}$$

The ideal gas constant has the following value for water vapor:

$$\Re = 461.522 \ {}^{J}/_{kg\,°K} \quad . \tag{3.72}$$

The specific heat at constant volume is given twice in Eq. (3.71), once for the undissociated vapor ($c_{v\_H_2O}$), and once for the dissociated vapor(c_{v_dis}):

$$c_{v\_H_2O} = 3\Re \qquad c_{v\_dis} = \frac{3}{2}\cdot 3\Re \quad . \tag{3.73}$$

The latent heat of dissociation is given by:

$$L_{dis} = 50{,}950{,}000 \ {}^{J}/_{kg} \quad . \tag{3.74}$$

Substituting these values into Eq. (3.71), the following expression is found for the energy of an ideal gas of water vapor:

$$U = M\Re\left[3T\left(1+\frac{\alpha}{2}\right)+\alpha\frac{L_{dis}}{\Re}\right] \quad . \tag{3.75}$$

It is obvious from the above that $U = U(M,T,\alpha)$, but the independent variables in this equation can also be chosen so that $U = U(T,V,M)$. Both of these formulations are useful. The time derivative of the latter form of the ideal gas energy gives an energy balance equation:

$$\dot{U} = \left(\frac{\partial U}{\partial T}\right)_{V,M} \dot{T} + \left(\frac{\partial U}{\partial V}\right)_{T,M} \dot{V} + \left(\frac{\partial U}{\partial M}\right)_{T,V} \dot{M} \quad . \tag{3.76}$$

Using the formulation of $U = U(M,T,\alpha)$ given above (Eq. (3.75)), expressions can be found for each of these differentials. Taking the time derivative of Eq. (3.75),

$$\dot{U} = \left(\frac{\partial U}{\partial T}\right)_{\alpha,M} \dot{T} + \left(\frac{\partial U}{\partial \alpha}\right)_{T,M} \dot{\alpha} + \left(\frac{\partial U}{\partial M}\right)_{T,\alpha} \dot{M} \quad . \tag{3.77}$$

Given $\alpha = \alpha(P,T)$,

$$\dot{\alpha} = \left(\frac{\partial \alpha}{\partial P}\right)_{T} \dot{P} + \left(\frac{\partial \alpha}{\partial T}\right)_{P} \dot{T} \quad . \tag{3.78}$$

Taking the time derivative of the ideal gas law,

$$\dot{P} = \frac{P}{g}\frac{\partial g}{\partial \alpha}\dot{\alpha} + P\left[\frac{\dot{T}}{T} + \frac{\dot{M}}{M} - \frac{\dot{V}}{V}\right] \quad . \tag{3.79}$$

Equations (3.78) and (3.79) can be used to find an explicit expression for $\dot{\alpha}$:

$$\dot{\alpha} = \eta\left\{\left(\frac{\partial \alpha}{\partial P}\right)_{T}\left[\frac{P}{T}\dot{T} + \frac{g\Re T}{V}\dot{M} - \frac{P}{V}\dot{V}\right]\dot{P} + \left(\frac{\partial \alpha}{\partial T}\right)_{P}\dot{T}\right\} \tag{3.80}$$

$$\eta = \left(1 - \frac{P}{g}\frac{\partial g}{\partial \alpha}\left(\frac{\partial \alpha}{\partial P}\right)_{T}\right)^{-1} \quad . \tag{3.81}$$

The function η is introduced to make Eq. (3.80) more tractable. Substituting Eqs. (3.79) and (3.80) into Eq. (3.77), collecting like terms, and using Eq. (3.76) to identify the differentials:

$$\left(\frac{\partial U}{\partial T}\right)_{V,M} \equiv C_v = Mc_v \tag{3.82}$$

$$= \left(\frac{\partial U}{\partial T}\right)_{\alpha,M} + \left(\frac{\partial U}{\partial \alpha}\right)_{T,M} \eta\left(\left(\frac{\partial \alpha}{\partial P}\right)_{T}\frac{P}{T} + \left(\frac{\partial \alpha}{\partial T}\right)_{P}\right)$$

$$\left(\frac{\partial U}{\partial V}\right)_{T,M} = -\frac{P\eta}{V}\left(\frac{\partial U}{\partial \alpha}\right)_{T,M}\left(\frac{\partial \alpha}{\partial P}\right)_{T} \tag{3.83}$$

$$\left(\frac{\partial U}{\partial M}\right)_{T,V} = \left(\frac{\partial U}{\partial M}\right)_{T,\alpha} + \frac{g\Re T\eta}{V}\left(\frac{\partial U}{\partial \alpha}\right)_{T,M}\left(\frac{\partial \alpha}{\partial P}\right)_{T} \quad . \tag{3.84}$$

The first law of thermodynamics for an open system gives another expression for the energy balance that describes the heat flow:

$$\dot{U} = \left(\frac{\partial U}{\partial M}\right)_{T,V}\dot{M} - \dot{W} + Q \quad . \tag{3.85}$$

The thermodynamic work is given by

$$\dot{W} = P\dot{V} \quad . \tag{3.86}$$

The heat added to the spark-generated bubble system will be assumed to take the following form:

$$Q = 4\pi R^2 q = 4\pi R^2\left(\Omega - q_{BB} - q_{M}\right) \quad . \tag{3.87}$$

The function Ω is the external delivered power per unit area, and will be discussed more in Sec. 3.5. The terms q_{BB} and q_{M} were defined in Eqs. (3.61) and (3.66). From Eqs. (3.76) and (3.85), an expression for the conservation of energy can be written:

$$Mc_{v}\dot{T} + \left(\frac{\partial U}{\partial V}\right)_{T,M}\dot{V} = Q - P\dot{V} \quad . \tag{3.88}$$

This equation may be solved for $\dot{T}$, with c_{v} given by Eq. (3.82):

$$\dot{T} = \left[Q - \left(\left(\frac{\partial U}{\partial V}\right)_{T,M} + P\right)\dot{V}\right]\frac{g\Re T}{c_{v}PV} \quad . \tag{3.89}$$

We may use Eqs. (3.79) and (3.80) to determine the equation for $\dot{P}$:

$$\dot{P} = \eta P\left[\left(\frac{\partial g}{\partial \alpha}\frac{1}{g}\left(\frac{\partial \alpha}{\partial T}\right)_{P} + \frac{1}{T}\right)\dot{T} + \frac{g\Re T}{PV}\dot{M} - \frac{1}{V}\dot{V}\right] \quad . \tag{3.90}$$

With the volume and its derivatives written in terms of the radius, these equations

take the final form:

$$\dot{T} = \frac{3g\Re T}{c_v PR}\left[q - \dot{R}\left(\left(\frac{\partial U}{\partial V}\right)_{T,M} + P\right)\right] \tag{3.91}$$

$$\dot{P} = \eta P\left[\left(\frac{\partial g}{\partial \alpha}\frac{1}{g}\left(\frac{\partial \alpha}{\partial T}\right)_p + \frac{1}{T}\right)\dot{T} + \frac{3g\Re T}{PR}\dot{m}_T - \frac{3\dot{R}}{R}\right] \quad . \tag{3.92}$$

These equations are the ones that are integrated simultaneously with the equations of bubble dynamics to give the time evolution of the spark-generated bubble.

Values for α and the specific heat at constant pressure have been calculated numerically for the water vapor system over wide ranges of pressure and temperature, and the results were used to fit the following empirical functions to the calculated values:[28]

$$\alpha = \frac{1}{2}\left[\tanh\left(\frac{T - T_0}{\tau} - \chi\right) + 1\right] \tag{3.93}$$

$$\overline{c_p(T)} = \frac{1}{T - T_0}\int_{T_0}^{T} c_p(T')\,dT' = c_{p,0} + \left(c_{p,1} - c_{p,0} + \frac{L_{dis}}{T - T_0}\right)\alpha(P,T) \quad , \tag{3.94}$$

where the variables and constants in these equations have the following values:

$$T_0 = 100\ ^\circ\mathrm{K} \qquad [T] = {}^\circ\mathrm{K} \tag{3.95}$$

$$\tau = \tau_0 (P/\mathrm{Pa})^{\tau_2} + \tau_1\ ^\circ\mathrm{K} \qquad [P] = \mathrm{Pa} \tag{3.96}$$

$$\tau_0 = 12.2384\ {}^\circ\mathrm{K}/\mathrm{Pa} \qquad \tau_2 = 0.253283 \qquad \tau_1 = 261.336\,^\circ\mathrm{K} \tag{3.97}$$

$$\chi = \chi_0 \ln(P/\mathrm{Pa}) + \chi_1 \qquad \chi_0 = -0.50792 \qquad \chi_1 = 13.017 \tag{3.98}$$

$$c_{p,0} = 1846.10\ \mathrm{J}/\mathrm{kg}\cdot{}^\circ\mathrm{K} \qquad c_{p,1} = 3461.43\ \mathrm{J}/\mathrm{kg}\cdot{}^\circ\mathrm{K} \quad , \tag{3.99}$$

and the latent heat of dissociation was given in Eq. (3.74) as

$$L_{dis} = 50{,}950{,}000\ \mathrm{J}/\mathrm{kg} \quad . \tag{3.74}$$

These functions are shown in Figs. 3.3 and 3.4 over typical ranges of pressure and temperature. Equation (3.94) for the average specific heat is then used in Eq. (3.69). With the form given for the dissociation (Eq. (3.93)), expressions for

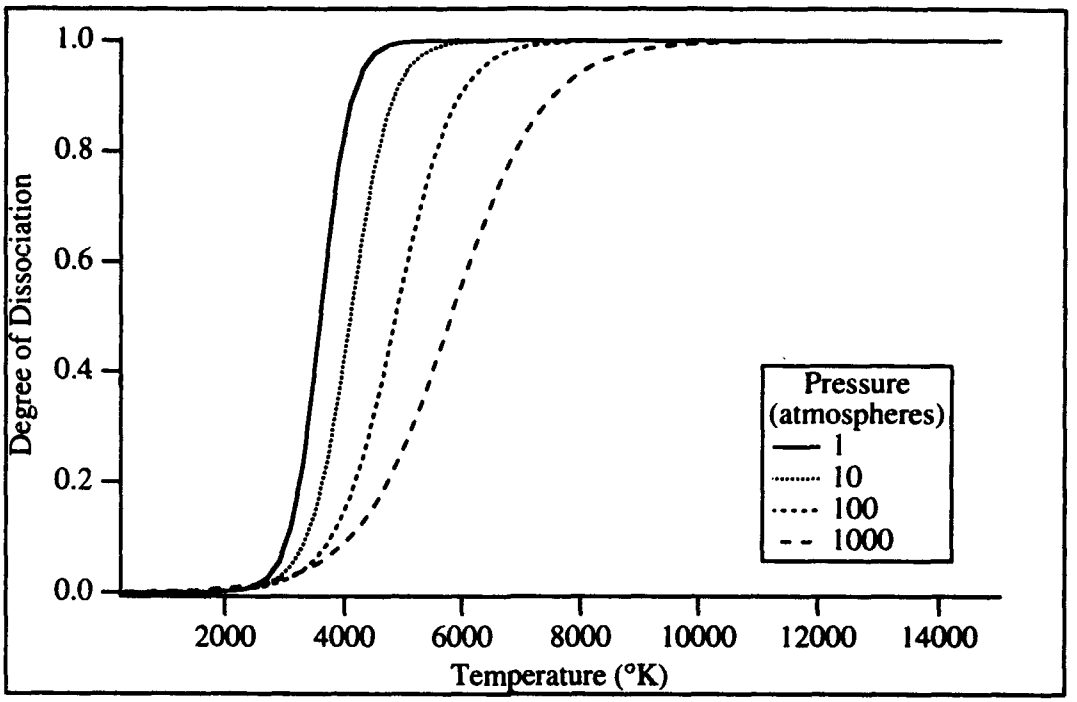

FIGURE 3.3
DEGREE OF DISSOCIATION

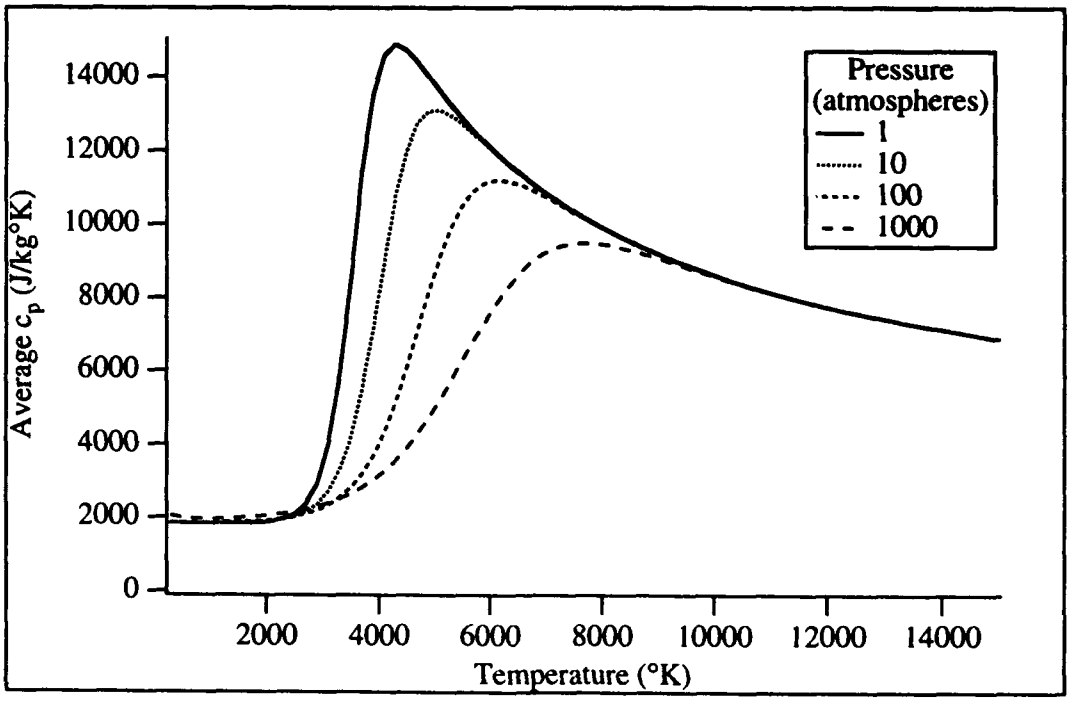

FIGURE 3.4
AVERAGE CONSTANT PRESSURE SPECIFIC HEAT CAPACITY

AS-93-273

the necessary differentials can be found:

$$\left(\frac{\partial \alpha}{\partial T}\right)_P = \frac{1}{2\tau}\operatorname{sech}^2\left(\frac{T-T_0}{\tau}-\chi\right) \tag{3.100}$$

$$\left(\frac{\partial \alpha}{\partial P}\right)_T = \frac{-1}{2P}\left[(T-T_0)(\tau-\tau_1)\frac{\tau_2}{\tau^2}+\chi_0\right]\operatorname{sech}^2\left(\frac{T-T_0}{\tau}-\chi\right) \quad . \tag{3.101}$$

$$\left(\frac{\partial U}{\partial V}\right)_{T,M} = \frac{-\eta P^2}{g}\left(\frac{3}{2}+\frac{L_{dis}}{T\Re}\right)\left(\frac{\partial \alpha}{\partial P}\right)_T \tag{3.102}$$

$$c_v = \Re\left[\frac{3}{2}\alpha+3+\eta\left(\frac{3}{2}+\frac{L_{dis}}{T\Re}\right)\left[P\left(\frac{\partial \alpha}{\partial P}\right)_T+T\left(\frac{\partial \alpha}{\partial T}\right)_P\right]\right] \quad . \tag{3.103}$$

3.5 Discharge Parameters

Some parameters are needed to describe the energy and power delivered during the discharge. The energy delivered by the spark discharge was previously identified in Sec. 2.3 as $E_{discharge}$. The power delivery as a function of time is determined by the circuit and water/vapor environment of the developing bubble. A detailed study of the evolution of this complex system is beyond the scope of this report. Instead, the actual power delivery curves will be approximated by functions that match the observed power delivery characteristics. Two different types of discharges were modeled in this study. The discharges in the sea tests[23] were nearly critically damped, and were approximated by the following function:

$$4\pi R^2 \Omega(t) = P_0\left(1-At_*^2\right)\sin \pi t_* \quad . \tag{3.104}$$

The function t_* is the non-dimensional discharge time:

$$t_* = \frac{t-t_{breakdown}}{\tau_{discharge}} \quad . \tag{3.105}$$

A finite time will pass before the gap "breaks down" and the main discharge begins. This time is referred to as the breakdown time ($t_{breakdown}$), and typically ranges from about 50 to 500 μs. The total discharge time is identified as $\tau_{discharge}$.

The constant P_0 in Eq. (3.104) is approximately the power amplitude, and is used as a fitting parameter for the discharge. The other parameter (A) in Eq. (3.104) is used to fit the asymmetry of the discharge. Integration of Eq. (3.104) yields the following expression for the total energy delivered during the discharge:

$$E_{discharge} = \frac{P_0 \tau_{discharge}}{\pi}\left[2 - A + \frac{4A}{\pi^2}\right] \quad . \tag{3.106}$$

For the discharges examined, a value of $A = 0.6$ led to a power delivery that matched the experimental data well. Substituting this value into Eq. (3.106) gives the following equation for the discharge energy:

$$E_{discharge} = 0.523 \tau_{discharge} P_0 \quad . \tag{3.107}$$

The discharges in the multiple bubble studies were underdamped, and were all of approximately the same energy and discharge time. Rather than fitting a function to the discharge, a table of sampled data was used as input to the model. The total energy was then adjusted as needed over a small range with a multiplicative constant. A plot of the power and delivered energy in the typical shot considered previously is shown in Fig. 3.5. This power is the one that was used in the simulations.

Because none of the details of the electrical system are included in the model, this model is essentially a thermal impulse model. In this respect, it is similar to the one developed by Gibson.[33]

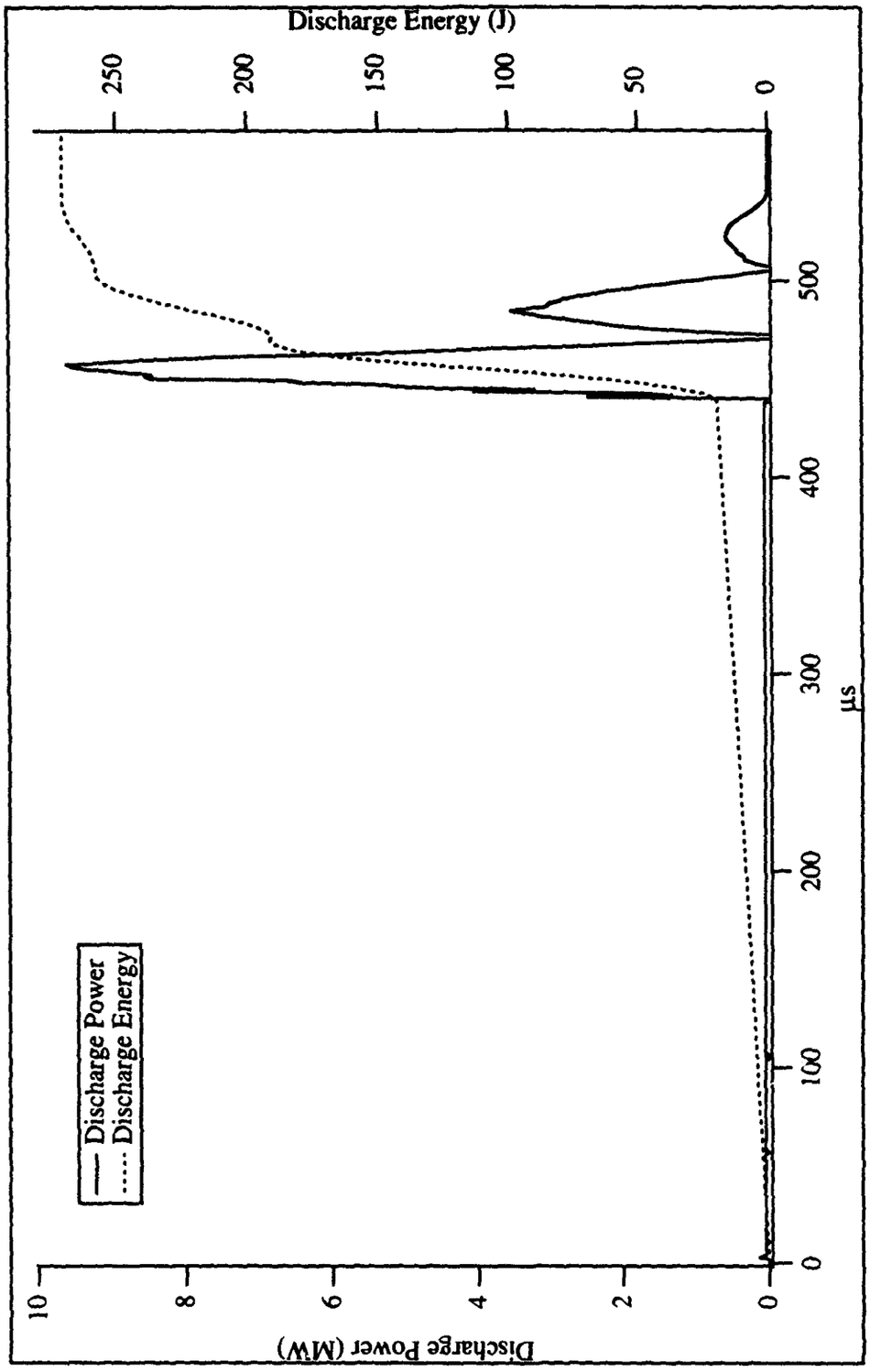

FIGURE 3.5
TYPICAL DISCHARGE POWER AND ENERGY

AS-93-274

3.6 Initial Conditions

Initial conditions must be chosen for the variables to be integrated in the model equations. Logical choices for the initial pressure and temperature are the following:

$$P_{init} = p_{\infty} \qquad T_{init} = T_E \quad . \tag{3.108}$$

T_E was previously given by Eq. (3.60). The initial volume is somewhat arbitrary, but some insight as to a reasonable choice can be gained by examining the discharge energy in Fig. 3.5. It can be seen on the plot of discharge energy that a small portion of the energy is delivered to the cavity before the main discharge starts. This "pre-discharge" energy is typically only a fraction of the total energy delivered to the bubble. Part of this pre-discharge energy will probably be conducted into the electrodes, but part of it may also be responsible for initiating a small cavity. Even if a cavity is not created by this portion of the discharge, the liquid near the electrodes may be "prepared" for the main discharge. Regardless of the physical mechanism, a reasonable choice for the initial conditions is that the initial potential energy of the cavity is proportional to this pre-discharge energy. Further examination of the energy delivery characteristics of a number of shots covering a range of energy shows that the fraction of the total energy delivered in this pre-discharge stage is roughly constant. This would mean that the initial potential energy of the cavity might then be proportional to the discharge energy:

$$P_{init} V_{init} = \eta_{init} E_{discharge} \tag{3.109}$$

The proportion of the discharge energy in the initial cavity potential energy is given by η_{init}. This choice does give good results in matching the data. Values tested for η_{init} ranged from about 0.05 to 0.3%.

3.7 Model Parameters

The preceding discussion outlines the model equations that will be integrated to determine the time evolution of spark-generated bubbles. Several fitting parameters have been introduced and discussed. The three fitting parameters outlined here were the ones used in the model.

1. α_M: The accommodation coefficient affects the mass flow resulting from evaporation and condensation in the model. The value of α_M is typically found to be between 0.01 and 1, and this parameter describes the condition of the interface. A "dirty" interface interferes with mass transfer across the bubble boundary, and will result in a lower coefficient.

2. x: The dissipation length is used in the radiation model to balance the mass flow as a result of heating from blackbody radiation against the radiation losses. A larger value of x will result in a larger portion of the radiation contributing to the mass flow, while a smaller value allows more radiation to escape from the bubble.

3. η_{init}: The proportion of the discharge energy in the initial cavity potential energy was discussed in the section immediately preceding this one. It is used in Eq. (3.109) to determine the initial radius.

These are the parameters that are adjusted to match the model output to the experimental data. The technique used to find the proper values for these parameters is discussed in Sec. 4.1. One set of values was found appropriate for all

the discharges examined:

$$\alpha_M = 0.005 \qquad x = 20 \text{ Angstroms} \qquad \eta_{init} = 0.001 \quad . \qquad (3.110)$$

With these parameter choices, the model closely matched the experimental data for single bubbles over wide ranges of discharge energy and depth.

---

[1]R. W. Schrage, *A Theoretical Study of Interphase Mass Transfer* (Columbia University Press, New York, New York, 1953).

[2]C. Herring, *Theory of the Pulsations of the Gas Bubble Produced by an Underwater Explosion* (Columbia University, New London, Connecticut, 1941), NDRC Report No. C4–sr20–010.

[3]L. Trilling, "The Collapse and Rebound of a Gas Bubble," *J. Appl. Phys.* **23**(1), 14–17 (1952).

[4]F. R. Gilmore, *The Growth or Collapse of a Spherical Bubble in a Viscous Compressible Liquid* (California Institute of Technology Hydrodynamics Laboratory, Pasadena, California, 1952), Report 26–4.

[5]H. G. Flynn, "Cavitation Dynamics. 1. A Mathematical Formulation," *J. Acoust. Soc. Am.* **57**(6), Pt. 1, 1379–1396 (1975).

[6]G. J. Lastman and R. A. Wentzell, "Comparison of Five Models of Spherical Bubble Response in an Inviscid Compressible Liquid," *J. Acoust. Soc. Am.* **69**(3), 638–642 (1981).

[7]S. Fujikawa and T. Akamatsu, "Effects of the Non-Equilibrium Condensation of Vapour on the Pressure Wave Produced by the Collapse of a Bubble in a Liquid," *J. Fluid Mech.* **97**(3), 481–512 (1980).

[8]A. Shima and Y. Tomita, "Some Numerical Aspects of Cavitation Bubble Collapse," in *Ann. Rev. of Num. Fluid Mech. Heat Transfer*, edited by L. A. Dziobek and B. Brienza (Hemisphere Publishing Corporation, 1989), Vol. 2, Chap. 5, pp. 198–226.

[9]J. B. Keller and M. Miksis, "Bubble Oscillations of Large Amplitude," *J. Acoust. Soc. Am.* **68**(2), 628–633 (1980).

[10]A. Prosperetti, "Bubble Phenomena in Sound Fields: Part One," *Ultrasonics* **22**, 69–77 (1984).

[11]A. Prosperetti and A. Lezzi, "Bubble Dynamics in a Compressible Liquid. Part 1. First-order Theory," *J. Fluid Mech.* **168**, 457–478 (1986).

[12]A. Lezzi and A. Prosperetti, "Bubble Dynamics in a Compressible Liquid. Part 2. Second-order Theory," *J. Fluid Mech.* **185**, 289–321 (1987).

[13]J. B. Keller and I. I. Kolodner, "Damping of Underwater Explosion Bubble Oscillations," *J. Appl. Phys.* **27**(10), 1152–1161 (1956).

[14]D. Epstein and J. B. Keller, "Expansion and Contraction of Planar, Cylindrical, and Spherical Underwater Gas Bubbles," *J. Acoust. Soc. Am.* **52**(3), Pt. 2, 975–980 (1972).

[15]L. E. Kinsler, A. R. Frey, A. B. Coppens, and J. V. Sanders, *Fundamentals of Acoustics* (John Wiley and Sons, New York, 1982), 3rd ed.

[16]J. G. Kirkwood and H. A. Bethe, *The Pressure Wave Produced by an Underwater Explosion* (Office of Science Research and Development, 1942), Report 588.

[17]R. H. Mellen, *An Experimental Study of the Collapse of a Spherical Cavity in Water* (U. S. Navy Underwater Sound Laboratory, New London, Connecticut, 1955), Research Report 279.

[18]W. Hentschel and W. Lauterborn, "Acoustic Emission of Single Laser-Produced Cavitation Bubbles and their Dynamics," *Appl. Sci. Res.* **38**, 225–230 (1982).

[19]R. H. Cole, *Underwater Explosions* (Princeton University Press, Princeton, New Jersey, 1948).

[20]M. H. Safar, "The Radiation of Acoustic Waves from an Air-Gun," *Geophysical Prospecting* **24**, 756–772 (1976).

[21]A. I. Ioffe and K. A. Naugol'nykh, "Formation of Shock Waves by an Electric Discharge in Water," *J. Appl. Mech. Tech. Phys. (PMTF)* **9**(1), 134–137 (1968).

[22]K. A. Naugol'nykh and N. A. Roi, *ELEKTRICHESKIE RAZRJADY V VODE* (Nauka, Moskva, 1971) [English transl.: *Spark Discharges in Water* (Applied Research Laboratories, The University of Texas at Austin, 1987), Internal Report].

[23]R. L. Rogers, *Intermediate Energy Tests and Analysis of a Plasma Sound Source* (Applied Research Laboratories, The University of Texas at Austin, 1992), Report ARL–TR–92–15.

[24]Y. Tomita and A. Shima, "On the Behavior of a Spherical Bubble and the Impulse Pressure in a Viscous Compressible Liquid," *Bull. JSME* **20**, 1453–1460 (1977).

[25]E. A. Martin, *The Underwater Spark: An Example of Gaseous Conduction at About 10,000 Atmospheres*, Ph.D. Dissertation (University of Michigan, Ann Arbor, 1956).

[26]E. A. Martin, "Experimental Investigation of a High-Energy Density, High-Pressure Arc Plasma," *J. Appl. Phys.* **31**(2), 255–267 (1960).

[27]*A Physicist's Desk Reference*, edited by H. L. Anderson (American Institute of Physics, New York, NY, 1989), 2nd ed. of *Physics Vade Mecum*, pp. 267–268.

[28]R. M. Roberts, *The Energy Partition of Underwater Sparks*, Ph.D. Dissertation (The University of Texas at Austin, to be published).

[29]Y. B. Zel'dovich and Y. P. Raizer, *Physics of Shock Waves and High-Temperature Hydrodynamic Phenomena*, edited by W. D. Hayes and R. F. Probstein (Academic Press, New York, 1966) Vol. I., Chap. 6, pp. 269–276.

[30]J. D. Jackson, *Classical Electrodynamics* (John Wiley and Sons, New York, 1975), 2nd ed., pp. 290–292.

[31]J. W. Robinson, M. Ham, and A. N. Balaster, "Ultraviolet Radiation from Electrical Discharges in Water," *J. Appl. Phys.* **44**(1), 72–75 (1973).

[32]D. C. Kelly, *Thermodynamics and Statistical Physics* (Academic Press, New York, 1973).

[33]D. C. Gibson, "The Kinetic and Thermal Expansion of Vapor Bubbles," *Trans. ASME, J. Basic Eng.* **94**(1), 89–96 (1972).

4. SINGLE BUBBLE RESULTS

To determine that the model captures the salient features of spark-generated bubbles, results from the numerical experiments using the model equations were compared to data taken in previous research conducted at ARL:UT. The data were taken in the Gulf of Mexico in May 1990. The energy of the spark discharges ranged from about 4.5 to 68 kilojoules, and data were taken at electrode depths of 30.5, 55, and 74.5 m, ±1 m. This is the most comprehensive set of data on spark bubbles known to be available over these ranges of energy and depth. These data were used to determine the parameters in the model equations, and the resulting model was compared with the data in Sec. 4.2. The model equations were used to calculate a signature for the average energy (270 J) and depth (10.4 m) used in the multiple bubble studies in Sec. 4.3.

4.1 Parameter Determination

Model simulations were carried out using the equations developed in Chap. 3 for several values of the three parameters identified in Sec. 3.7, and the best values found are given there. In determining these parameters, the modeled acoustic signatures were compared to the measured acoustic signatures over the full

ranges of energy and depth for which data were taken in the referenced paper. Characteristics examined to determine the model parameters were the following:

1. Bubble Period
2. Radiated Acoustic Energy in the Expansion Pulse
3. Minimum Rarefaction Pressure

These characteristics were identified in Fig. 1.3, and discussed in Chap. 1. The following three parameters were identified in Sec. 3.7:

$$\alpha_M = 0.005 \qquad x = 20 \text{ Angstroms} \qquad \eta_{init} = 0.001 \quad . \qquad (3.110)$$

The determination of three parameters such as these would generally be a very difficult task, but the process was greatly simplified by examining the action of the three parameters on the acoustic signatures. Generally, the three parameters each affected something in the acoustic signature that the other parameters did not. This allowed the three parameters to be easily adjusted, as long as the adjustments were made "in order". The three parameters used, with the characteristics that they adjusted independently, were the following:

η_{init}: This parameter affected nearly all the characteristics, but the independent characteristics it affected were the initial peak pressure, and the acoustic energy in the expansion pulse. This parameter was adjusted to give the correct values for the initial peak pressure, and the acoustic energy was then generally correct also.

α_M: While this parameter had only a limited effect on the expansion pulse, it had a very large effect on the collapse pulse, and affected the bubble period

somewhat. This parameter was adjusted to match the general shape of the collapse pulse (width, rise time, etc.), but was not optimized with respect to the collapse pulse peak pressure, because of the stochastic nature of the collapse on the measured acoustic signatures.

x: This parameter tended to affect primarily the bubble period, so it was especially useful to put the fine touches on the parameter fit. Surprisingly, it did not dramatically affect the peak pressure of the expansion pulse in this model, though other studies[1] have indicated that the details of the blackbody radiation may affect the expansion pulse.

The adjustment procedure of these three parameters was repeated a number of times with similar results achieved each time. The first parameter (η_{init}) was adjusted an order of magnitude in each direction. The peak pressures on the expansion pulse varied over a range of about one-half to two times the final value chosen as the parameter was adjusted. The accommodation coefficient (α_M) was adjusted over a range from 0 to 0.02. At higher values of this parameter the collapses were very violent, but within this range the model was stable with the shape of the collapse peak resembling that of a gas bubble as the accommodation coefficient vanished. The dissipation length (x) adjusted the energy losses in the model, and because the bubble period varied as the cube root of the energy, this parameter was relatively easy to adjust. Within the range of the accommodation coefficient given above, the dissipation length could usually be adjusted to give the proper bubble period.

4.2 Sea Data Comparison

The model equations were integrated for each of the energies and depths at which data were taken, using a parameter fit for the input energy. The output signatures were then compared to the data. Several of the experimental acoustic signatures representative of the data are plotted in Figs. 4.1, 4.2, 4.3, and 4.4, with the model acoustic signatures overlaid. The agreement between the model and experiment is reasonable over the ranges of energy and depth examined. The experimental acoustic signatures, however, are asymmetric in the negative part of the overpressure, while the model signatures are symmetric. The single bubble signatures recorded in the multiple bubble studies are symmetric, so it is possible that this asymmetry is an artifact of the measurement method. The signature characteristics mentioned above were examined, along with the peak pressure of the acoustic pulse generated on the collapse.

A plot of the bubble period as a function of energy and depth is shown in Fig. 4.5. The dependence of the model on depth and discharge energy is very similar to the dependence in the data. In particular, the hydraulic efficiency did not change measurably with energy, but the average hydraulic efficiency did increase slightly with depth, from about 29% at 30.5 m to about 32% at 74.5 m. This efficiency appeared to depend weakly on the discharge parameters. For example, a few of the data points in Fig. 4.5 were taken at similar energies but with different discharge times (identified in Fig. 4.5 as open symbols). The simple model used to examine the data in the referenced report failed to pick up the dependence of the bubble period on discharge time. Unfortunately, this model does little better, despite its matching the bubble period dependence on depth and discharge energy,

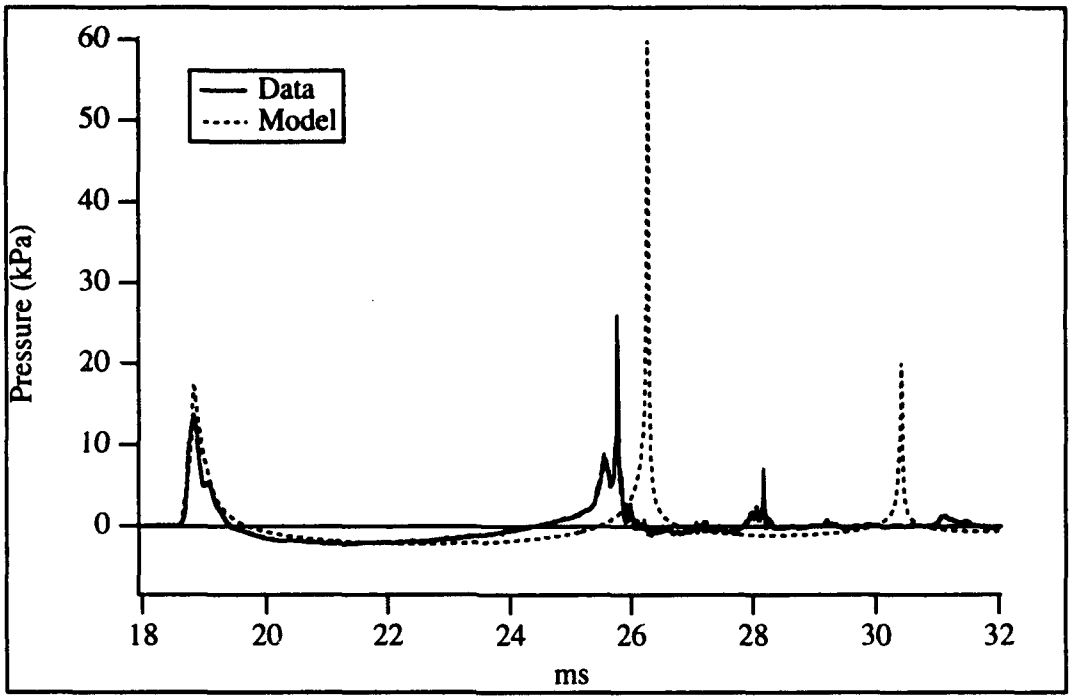

FIGURE 4.1
9.5 kJ ACOUSTIC SIGNATURE; DEPTH: 55 m

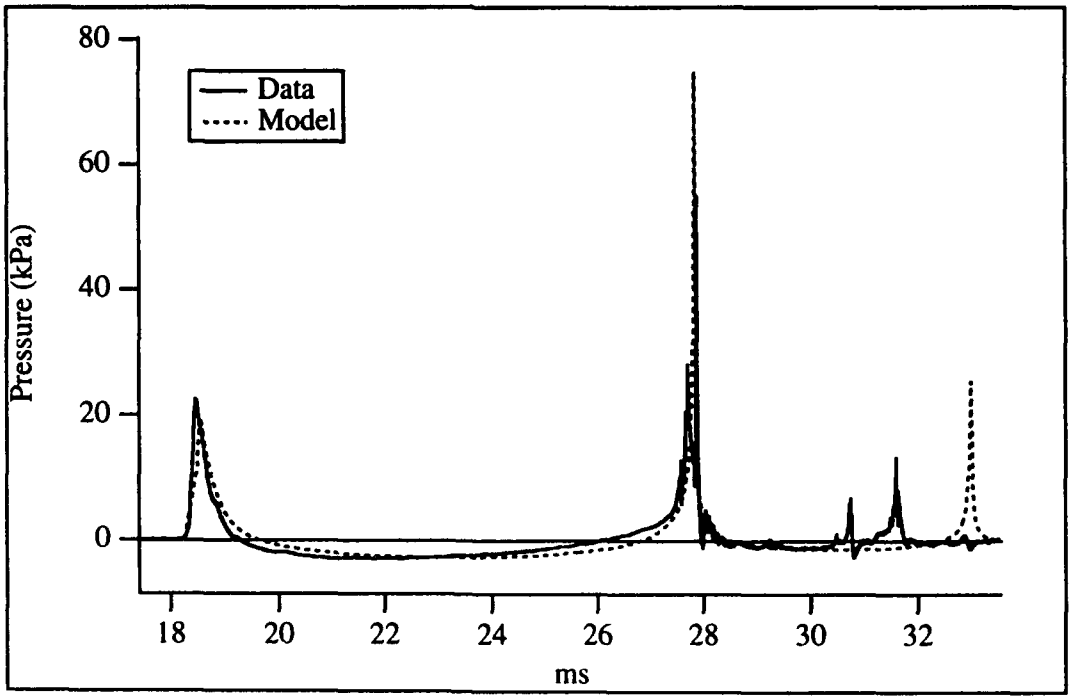

FIGURE 4.2
19 kJ ACOUSTIC SIGNATURE; DEPTH: 55 m

AS-93-275

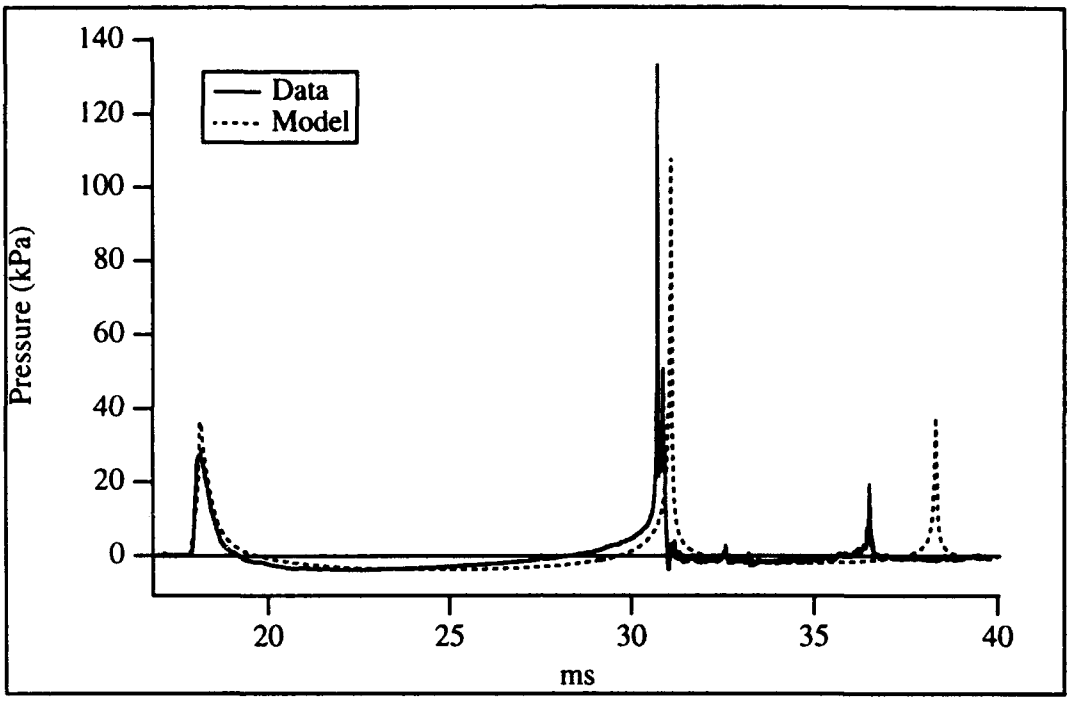

FIGURE 4.3
49 kJ ACOUSTIC SIGNATURE; DEPTH: 55 m

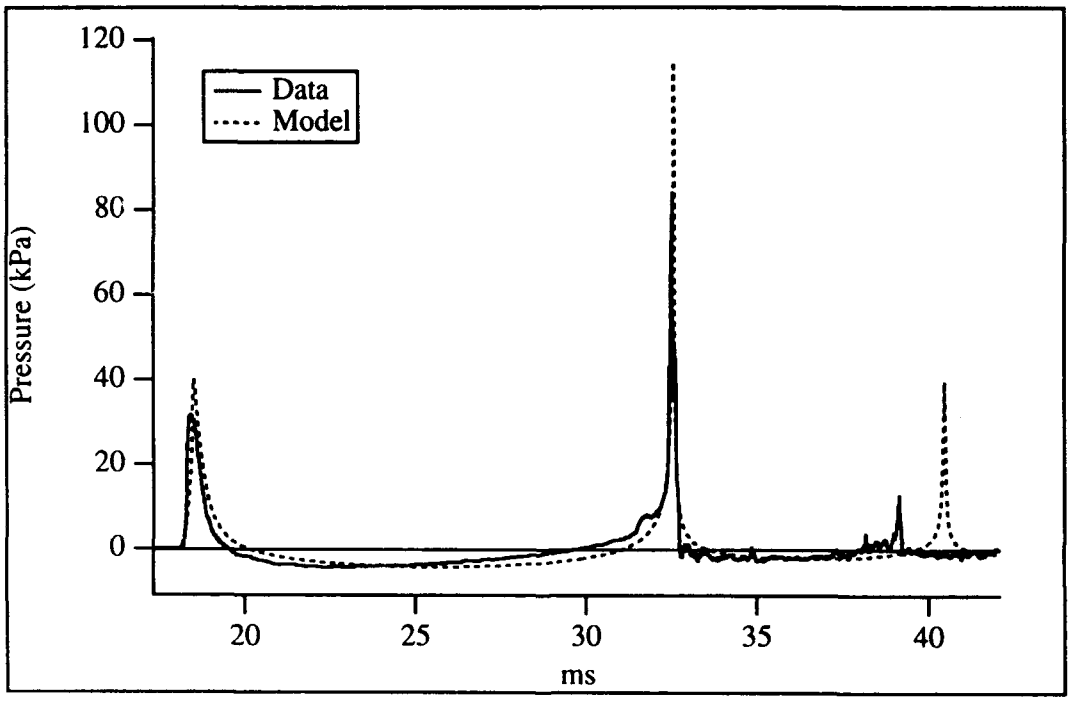

FIGURE 4.4
62.5 kJ ACOUSTIC SIGNATURE; DEPTH: 55 m

AS-93-276

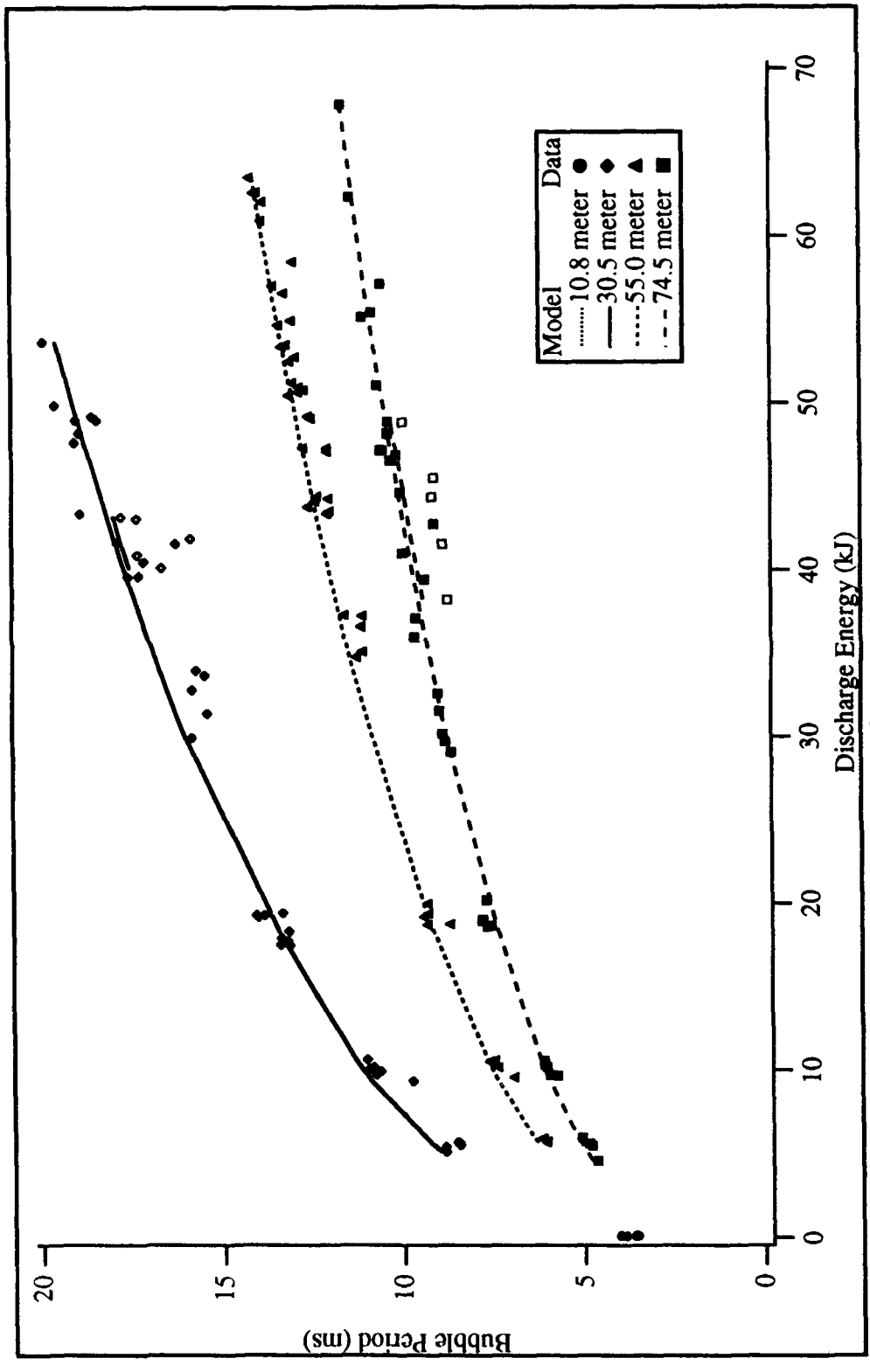

FIGURE 4.5
BUBBLE PERIOD versus ENERGY AND DEPTH

AS-93-277

predicting only about a 1% decrease in the hydraulic efficiency, while the data showed a decrease in efficiency of about 3 to 7%.

The results found are not universally accepted. The technical brief written by Gibson[2] indicated that the pulsation time of spark-generated bubbles did not obey the energy scaling given by Eq. (2.51). The study reported in that brief considered spark-discharge bubbles in water of varying temperatures, and found that for all temperatures, and especially for water near the boiling point, the scaling in Eq. (2.51) predicted a change in the bubble period as a function of energy that was too large. The study was based on the energy stored in the capacitor with no attempt to find the actual energy delivered to the cavity, and assumed that the energy delivered would be some fraction of the stored energy. Most discharge systems, however, deliver energy most efficiently in a narrow regime of discharge parameters, and the ratio of energy delivered to energy stored is rarely constant over a wide range of energy. The study by Rogers and the experimental work reported in this report measured the energy delivered to the spark cavity at the location of the discharge, removing any effect of the electrical discharge system on the energy measurements. This technique allows the electrical discharge characteristics and the production of a bubble by a given electrical discharge to be considered independently.

Plots of the peak pressures in the expansion and collapse pulses are shown in Figs. 4.6 and 4.7, respectively. The data in these plots are somewhat more stochastic than the bubble periods and exhibit no strong dependence on depth. The agreement between experiment and model is good for the initial peak, while the agreement is not as good for the collapse peak. A possible explanation for the

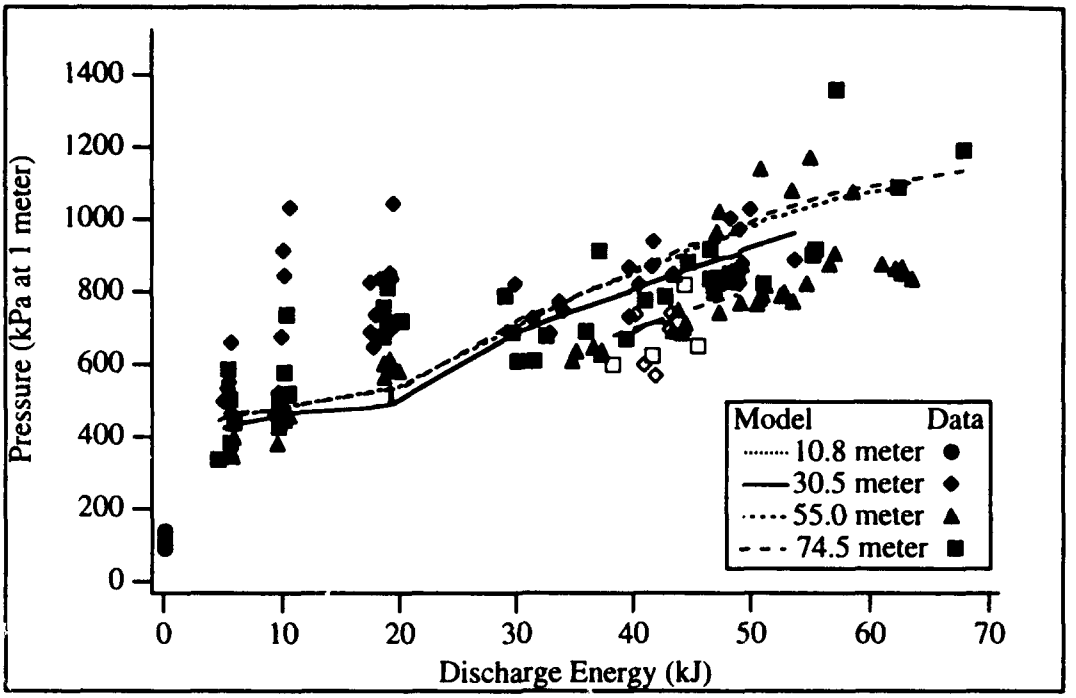

FIGURE 4.6
PEAK EXPANSION PULSE PRESSURE

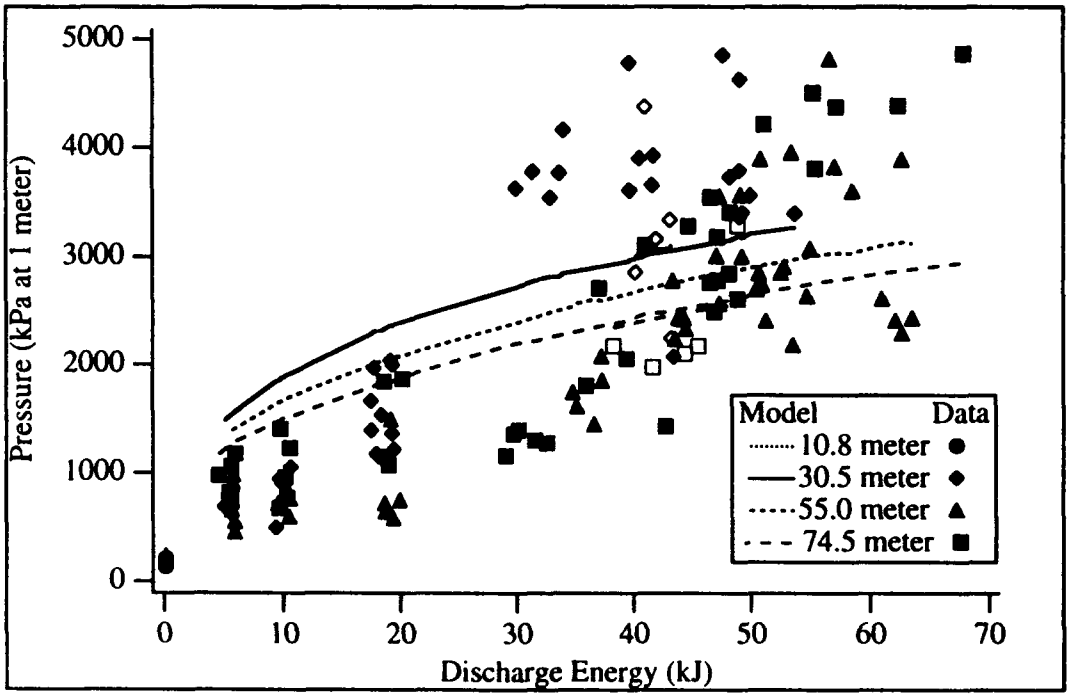

FIGURE 4.7
PEAK COLLAPSE PULSE PRESSURE

AS-93-278

poor agreement on the collapse is the more violent nature of the collapse, during which the bubble often breaks apart before reaching the minimum radius. The minimum rarefaction pressure is plotted in Fig. 4.8. The experimental and model data show a similar dependence on depth, though the values do not match exactly. The acoustic energy in the expansion pulse is plotted in Fig. 4.9. As with the peak pressures, the acoustic energy does not exhibit a strong depth dependence, and the agreement is good between model and experiment.

Of the characteristics examined above, the bubble period and minimum negative pressure exhibited a measurable depth dependence, while the peak pressures and acoustic energy in the initial peak did not. The explanation for this is that the internal pressures in the bubble at the time of the initial expansion and at the collapse are 100 - 1000 times the ambient pressure, while the internal pressure at the time of the minimum negative pressure is only about 10% of the ambient pressure. The depth dependence of the bubble period is essentially the dependence predicted by Eq. (2.51), with the slight increase in the hydraulic efficiency mentioned above.

4.3 Lake Data Comparison and Model Output

Only a small amount of information on the bubble dynamics is available from the experiments, because the only indicator is the acoustic signature measured by the hydrophone. With the model, however, more information is available. The good agreement between several characteristics of the measured and modeled acoustic signatures over wide ranges of energy and depth indicates that the model is

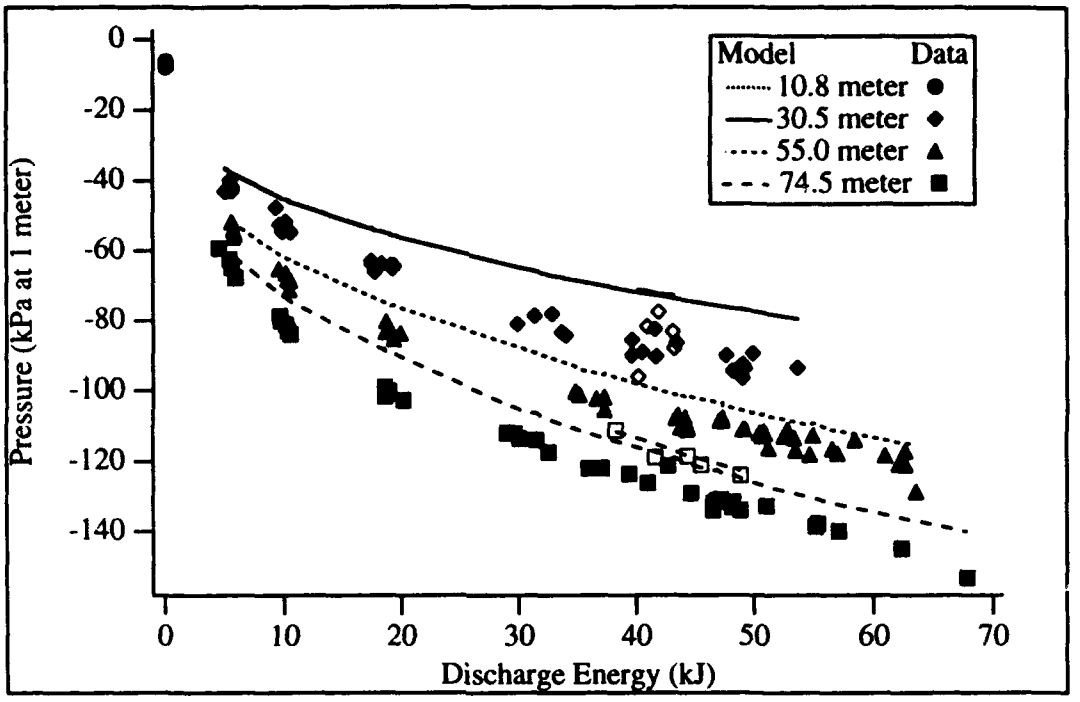

FIGURE 4.8
MINIMUM RAREFACTION PRESSURE

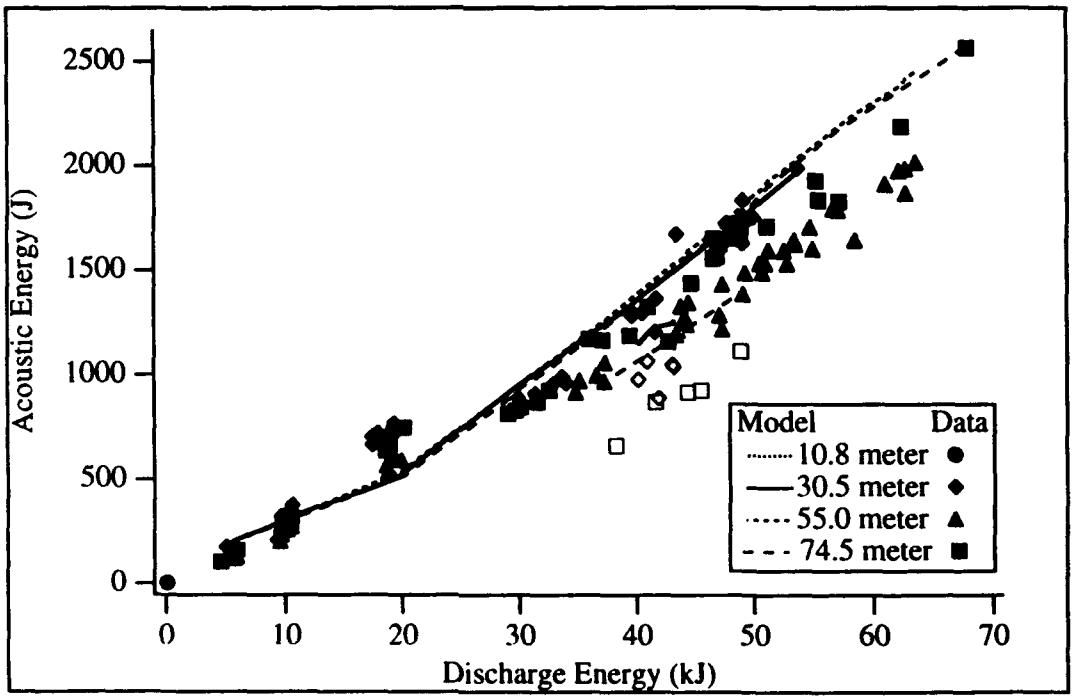

FIGURE 4.9
ACOUSTIC ENERGY IN EXPANSION PULSE

AS-93-279

a reasonable approximation to the actual bubble dynamics, at least within the ranges of discharge energy and depth for which the parameters were determined. It was mentioned in the introduction to this chapter that an energy of 270 joules and a depth of 10.4 m were used for the multiple bubble experimental studies. This energy is more than an order of magnitude lower than the lowest energy in the data used to determine the parameters, and the ambient pressure is only half of the lowest ambient pressure in that data. The general nature of the data recorded in the multiple element studies is discussed in Sec. 6.6, and a representative signature from the data collected was chosen based on the average bubble period, discharge energy, and peak expansion pulse pressure. This acoustic signature was first shown in Fig. 1.3, and is shown in Fig. 4.10 with the model acoustic signature calculated from the average input parameters. Although the discharge parameters are far from the ranges used for the model parameter fit, the match between modeled and measured signature is very good. The average hydraulic efficiency was calculated for these data to be about 35%. Plots of the model output showing the mach number and temperature for this discharge as a function of time are shown in Figs. 4.11 and 4.12, where the bubble radius has been overlaid in each plot to help identify the important characteristics. The maximum radius in the model is typically about 95% of the maximum radius predicted from the bubble period, supporting the assumption made in Chap. 2 that the spark-generated bubbles obeyed Eq. (2.47). The ratio of the maximum radius to the minimum radius (at the bubble collapse) was approximately equal to 12 for this discharge. The bubble wall mach number on expansion of the bubble is about 0.05, and it typically reaches values of –0.15 – –0.2 on the collapse. This compares reasonably to the value of

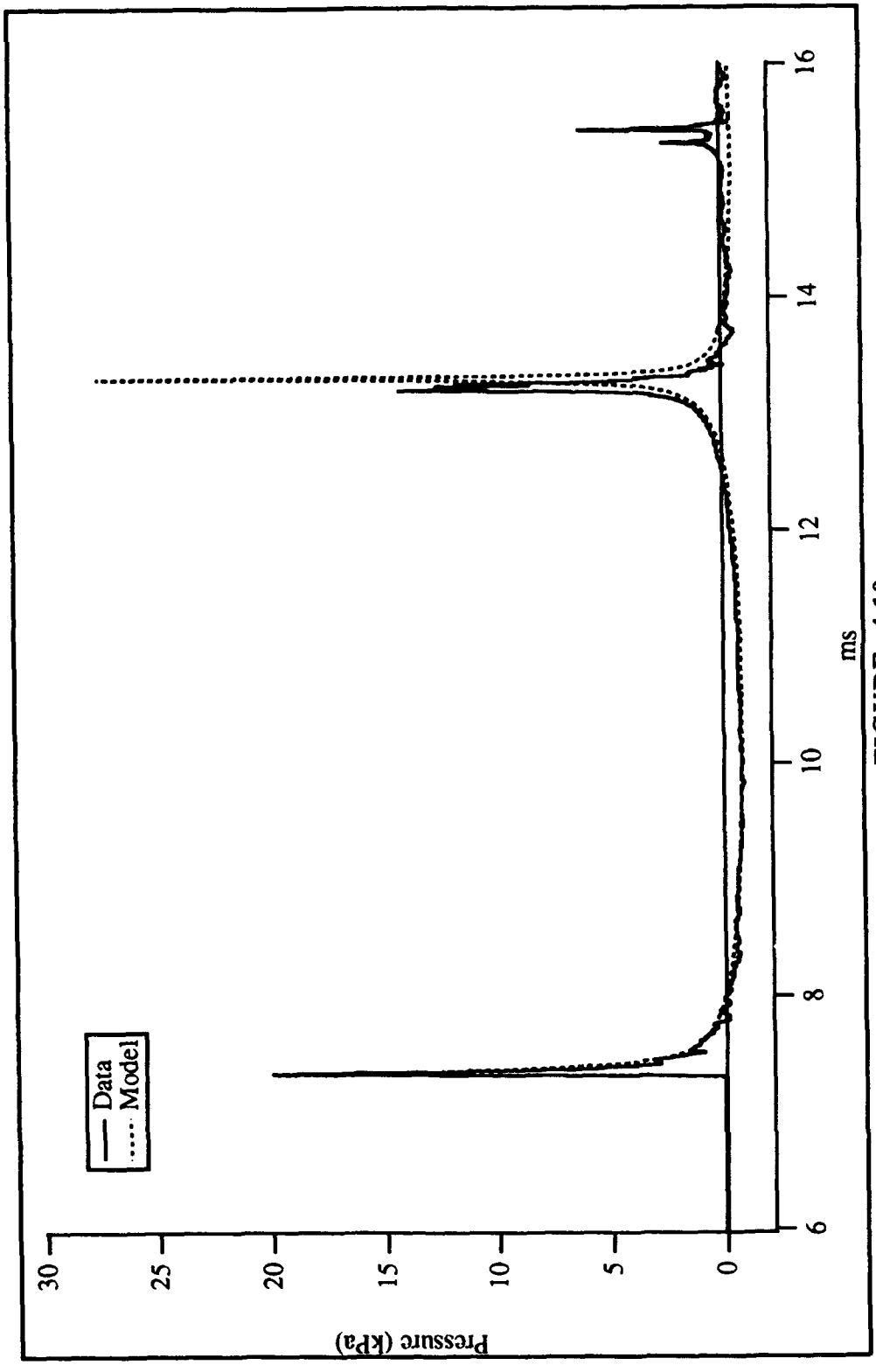

FIGURE 4.10
270 J ACOUSTIC SIGNATURE; DEPTH: 10.4 m

AS-93-280

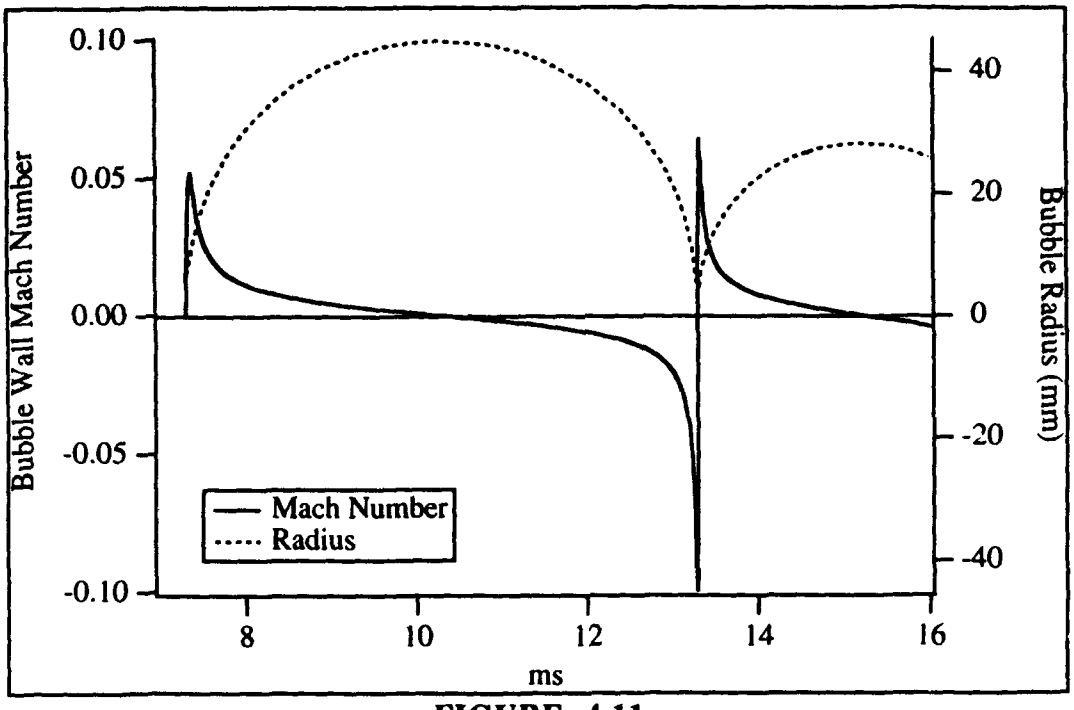

FIGURE 4.11
270 J MODEL BUBBLE WALL MACH NUMBER

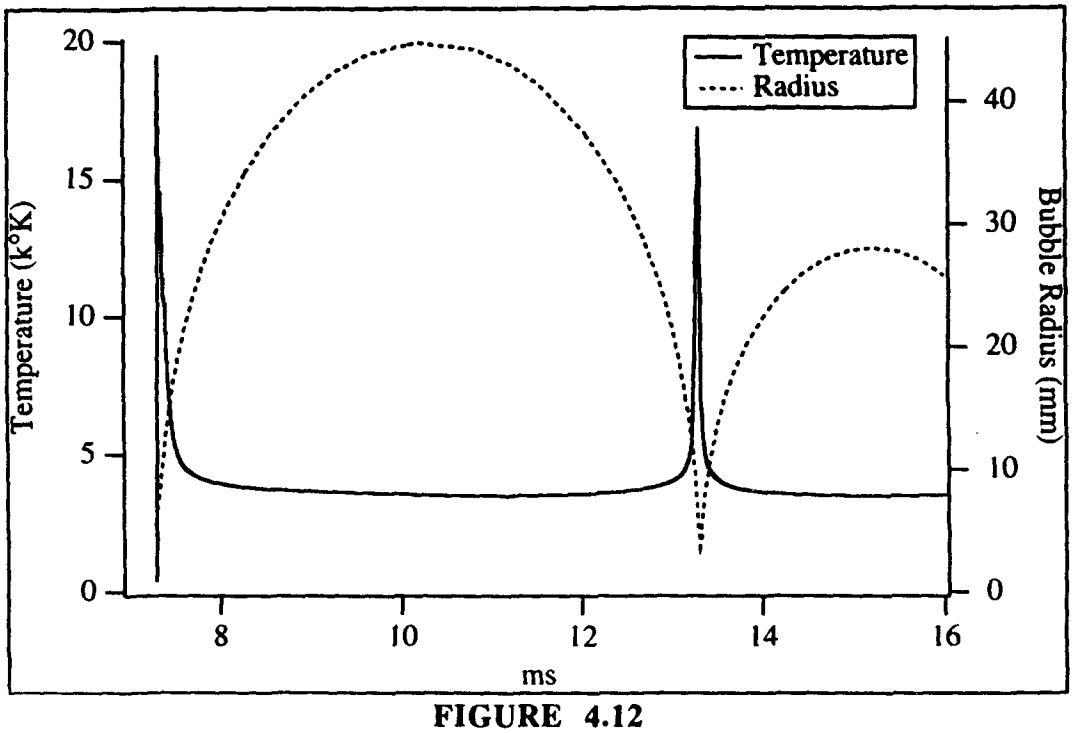

FIGURE 4.12
270 J MODEL BUBBLE INTERIOR TEMPERATURE

AS-93-281

0.07 given by Guman[3] for more energetic discharges (approximately 3 kJ) at similar depths. The peak pressure on the expansion of the bubble averages about 22 kPa for the 270 J discharges, while the model predicts about 20 kPa. A value of about 23 kPa can be calculated from data presented by Guman, for energies ranging from 750 - 1920 J, if the results in that paper are extrapolated down to this discharge energy. The model predicts peak temperatures in the bubble of about 20,000°K during the power delivery and at the collapse. Estimates of the temperature have been made on similar discharges. In a discharge that delivered about 900 J, Martin[4] found an outer layer temperature of about 30,000°K, and estimated that the internal temperature could be even higher. Calculations and measurements by Shamko[5] for discharges ranging from 140 to 780 J indicated temperatures in the range of 20 - 25,000°K.

TABLE 4.1

ENERGY BUDGET OF TYPICAL DISCHARGE

Total Energy Delivered	270 J		
Blackbody Energy Loss		65 J	(24 %)
Mass Flow Energy Loss		141 J	(52 %)
Total Energy Loss		206 J	(76 %)

An exact accounting of the energy losses from this model has not been given because of the approximate nature of the energy loss mechanisms. To allow a future comparison with more exact models, the energy budget for this particular discharge is given in Table 4.1.

4.4 Sea Water versus Fresh Water

The model developed in this study is used in sea water and fresh water without distinction. The only changes that enter the model directly are the sound speed and the density of the water. This study does not consider the conductivity of the water which affects the nature of the breakdown. This effect has been detailed in other studies.[6] In this study, the discharges are assumed to be given, and the development of the discharges in a medium is not considered. The model is therefore used without modification to describe the dynamics of a bubble in either sea water or fresh water.

---

[1]R. M. Roberts, *The Energy Partition of Underwater Sparks*, Ph.D. Dissertation (The University of Texas at Austin, to be published).

[2]D. C. Gibson, "The Pulsation Time of Spark Induced Vapor Bubbles," *Trans. ASME, J. Basic Eng.* **94**, 248–249 (1972).

[3]W. J. Guman, "Study of an Inverse-Pinch Electric Discharge Sound Source," *J. Underwater Acoust.* **17**(3), 511–521 (1967).

[4]E. A. Martin, *The Underwater Spark: An Example of Gaseous Conduction at About 10,000 Atmospheres*, Ph.D. Dissertation (University of Michigan, Ann Arbor, 1956).

[5]V. V. Shamko, "Integrated Bulk Characteristics of the Plasma in an Underwater Spark," *Zh. Tekh. Fiz.* **48**, 967–971 (1978) [English transl.: *Sov. Phys. Tech. Phys.* **23**(5), 564–567 (1978)].

[6]K. A. Naugol'nykh and N. A. Roi, *ELEKTRICHESKIE RAZRJADY V VODE* (Nauka, Moskva, 1971) [English transl.: *Spark Discharges in Water* (Applied Research Laboratories, The University of Texas at Austin, 1987), Internal Report].

5. INTERACTION MODEL

The model developed is intended to predict bubble behavior when several bubbles are performing large amplitude oscillations simultaneously. The approach used in this study describes qualitatively the interactions in airgun arrays and quantitatively the modifications to bubble dynamics by an incident sound field (see Chap. 1).

5.1 Variable Pressure Calculation

The variable pressure introduced in Eq. (3.19) describes the interaction of a bubble with any incident sound field. In this model, the variable pressure at the location of a particular bubble is presumed to be the total sum of the sound fields radiated by the other bubbles. The reflections from boundaries, for instance, could be included in the variable pressure, but this study will not include such effects. In general, the variable pressure will be a function of the number of bubbles, internal pressure and radius of the other bubbles at some previous time, and relative positions of the bubbles. The subscript "i" denotes the bubble for which the variable pressure will be calculated. The distance between bubble "i" located at $\vec{x}_i$ and bubble "j" located at $\vec{x}_j$ is denoted by r_{ij}, where r_{ij} is given by

$$r_{ij} = \left| \vec{x}_i - \vec{x}_j \right| \quad . \tag{5.1}$$

The general equation for the variable pressure at the position of the i'th bubble in an array of N bubbles is found by adding the contributions from each of the bubbles, where the pressure due to the j'th bubble at r_{ij} is given by Eq. (2.36):

$$p_v(\vec{x}_i,t) = \sum_{\substack{j=1 \\ j\neq i}}^{N} \left[p_j(r_{ij},t_r) - p_\infty \right] \tag{5.2}$$

$$t_r \equiv t - r_{ij}/c_\infty \quad . \tag{5.3}$$

The retarded time here is an approximation because it does not consider the position of the bubble wall when the pressure is radiated. The calculation of the retarded time including the moving bubble wall is an additional complication not warranted in this study.

5.2 Evaluation of the Error

In Chap. 3 it was discussed that the incident pressure waves vary in amplitude and phase over the surface of a given bubble. This pressure varies in time and space, but the model introduced in this report considers only radial movement of the bubbles and makes no allowance for any asymmetrical effects of the variable pressure on the bubble. The actual variable pressure is therefore replaced with an average variable pressure that is assumed to surround the bubble and is only a function of time. The sound speed is assumed constant and finite.

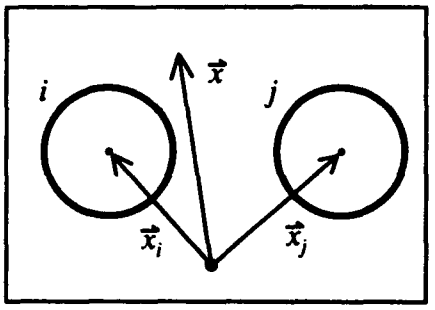

FIGURE 5.1
BUBBLE DIAGRAM
AS-93-282

Consider the two bubbles shown in Fig. 5.1. Assume that bubble "i" is the bubble of interest, and the incident variable pressure is generated by bubble "j."

The incident pressure waves radiated by bubble "*j*" will propagate past bubble "*i*" at the sound speed in the liquid. The time for the pressure wave to propagate past bubble "*i*" is given by

$$\tau_i = \frac{2R_i}{c_\infty} \quad . \tag{5.4}$$

The change in the bubble radius during this time is given approximately by

$$R_i(\tau_i) \approx R_i + \Delta R_i \approx R_i + \dot{R}\tau_i = R_i + 2R_i\dot{R}_i/c_\infty = R_i(1+2m) \quad . \tag{5.5}$$

The change in the radius is of the order of the bubble wall mach number, which has already been assumed small. This cursory examination indicates that the time scales are such that the bubble radius changes slowly with respect to the speed of propagation of a pressure wave past the bubble, so the bubble size is approximately constant as the pressure wave sweeps past. Because the liquid pressure at the surface of the bubble enters the equations of dynamics directly, it is reasonable to assume that the effective variable pressure is approximately given by the variable pressure averaged over the surface of the bubble. The form of the incident pressure is known, and can be used to calculate the average variable pressure analytically.

The pressure at any point in the liquid was given as a sum of a farfield term and an afterflow term by Eq. (2.20):

$$p(r,t) - p_\infty = \frac{R}{r} p_{\text{farfield}}(t) + \frac{R^4}{r^4} p_{\text{afterflow}}(t) \quad . \tag{2.20}$$

Although this equation is written in the incompressible form, it was explained in Chap. 2 that the only change necessary to make this equation valid to first order is to evaluate the terms on the right hand side at the retarded time (Eq. (5.13)). An

appropriate form of the pressure distribution for this study is the following:

$$p_v(\vec{x},t) = p(\vec{x},t) - p_\infty = \frac{R_j(t_r)}{|\vec{x}-\vec{x}_j|}\, p_{\text{farfield}}(t_r) + \frac{\left(R_j(t_r)\right)^4}{|\vec{x}-\vec{x}_j|^4}\, p_{\text{afterflow}}(t_r) \quad . \tag{5.6}$$

The distance between a point $\vec{x}$ and the center of bubble "j" located at $\vec{x}_j$ is denoted by r_j, where r_j is given by

$$r_j = |\vec{x}-\vec{x}_j| \quad . \tag{5.7}$$

The average variable pressure over the surface of bubble "i" is given by

$$\left\langle p_v(\vec{x},t)\right\rangle_{\text{bubble}} = \frac{1}{4\pi}\int_0^{2\pi} d\varphi \int_0^{\pi} \sin\theta\, d\theta \left[\frac{R_j}{r_j}\, p_{\text{farfield}} + \frac{R_j^4}{r_j^4}\, p_{\text{afterflow}}\right]_{t_r} \quad . \tag{5.8}$$

If the origin of the coordinate system is taken at the center of bubble "i," r_j can be written explicitly as

$$r_j = |\vec{x}-\vec{x}_j| = \sqrt{r_{ij}^2 - 2r_{ij}|\vec{x}|\cos\theta + |\vec{x}|^2} \quad . \tag{5.9}$$

The distance between the bubble centers (r_{ij}) is given by Eq. (5.9). On the surface of the bubble, $|\vec{x}| = R_i$. The choice of origin leaves no dependence on φ in r_j, so that the integral can be done immediately. If the distance between the centers of the two bubbles is given by $r_{ij} = \delta$, the integral becomes:

$$\left\langle p_v(\vec{x},t)\right\rangle = \int_0^{\pi} \frac{\frac{1}{2}\sin\theta\, d\theta\, R_j\, p_{\text{farfield}}}{\sqrt{\delta^2 - 2\delta R_i\cos\theta + R_i^2}} + \int_0^{\pi} \frac{\frac{1}{2}\sin\theta\, d\theta\, R_j^4\, p_{\text{afterflow}}}{\left(\delta^2 - 2\delta R_i\cos\theta + R_i^2\right)^2} \quad . \tag{5.10}$$

This integral is easily done with the result given by

$$\left\langle p_v(\vec{x},t)\right\rangle_{\substack{\text{bubble}\\ |\vec{x}|=R_i}} = \frac{R_j}{\delta}\, p_{\text{farfield}} + \frac{R_j^4}{\delta^4}\, p_{\text{afterflow}}\, \frac{\delta}{4R_i}\left[\frac{1}{(1-R_i/\delta)^2} - \frac{1}{(1+R_i/\delta)^2}\right] . \tag{5.11}$$

The immediate result worth noting is that the average variable farfield pressure is given exactly by the variable farfield pressure at the center of bubble "i." The afterflow term is a little more difficult to evaluate, but some insight is gained by

examining when this term is likely to have an effect. The average variable pressure can be written in the form

$$\left\langle p_v(\vec{x},t)\right\rangle_{\substack{\text{bubble}\\ |\vec{x}|=R_i}} = \frac{R_j}{\delta} p_{\text{farfield}} + \frac{R_j^4}{\delta^4} p_{\text{afterflow}} \chi_i \tag{5.12}$$

$$\chi_i = \frac{\delta}{4R_i}\left[\frac{1}{(1-R_i/\delta)^2} - \frac{1}{(1+R_i/\delta)^2}\right] . \tag{5.13}$$

If $\delta \gg R_i$, then $\chi_i \to 1$, and the average value of the afterflow term is given by its value at the center of the bubble. The afterflow term is likely to have the greatest effect on the bubble dynamics when the magnitude of the bubble wall velocity is largest. The model results in Sec. 4.3 show that for the bubbles used in the multiple bubble studies, the bubble wall mach number reaches a value of approximately -0.1 at $R_i \approx \frac{2}{11} R_{\max}$. The minimum separation possible between the bubbles (when the bubble walls touch at $R_i = R_{\max}$) will be $\delta_{\min} = 2R_{\max}$. Then $\delta_{\min}/R_i \approx 11$, which gives a value of $\chi_i \approx 1.02$. This is a negligible error in view of the other measurement errors in the experiment, indicating that the average variable pressure on the surface of bubble "i" was well approximated by the variable pressure evaluated at the center of the bubble ($\vec{x}_i$).

One other source of error that should be considered is the possibility that the average variable pressure is a poor description of the relevant physical effects when the bubble separation is small. The farfield term of the variable pressure, which varies as r^{-1}, changes slowly across the bubble, but the afterflow term of the variable pressure changes much more rapidly across the bubble because of the r^{-4} dependence. At the closest separations, the afterflow term can have some influence on neighboring bubbles, and the possibility exists that the bubble may develop asymmetrically, with changes in the bubble dynamics that have not been addressed.

This indicates that even replacing the pressure at the center of the bubble by the average pressure over the bubble may not be a sufficiently good description of the interaction between bubbles when the afterflow terms are important. A study done by Shima and Tomita[1] describes the interaction of a bubble with an incident pressure wave. They found that the pressure wave acting on the bubble could significantly affect its dynamics, if the pressure wave was sufficiently high amplitude. These bubbles tended to collapse more rapidly than an isolated bubble, and often became asymmetrical as they collapsed, with higher pressures induced on the collapse.

---

[1]A. Shima and Y. Tomita, "Impulsive Generation by Bubble/Pressure-Wave Interaction," *AIAA Journal* **26**(4), 434–437 (1988).

6. EXPERIMENTAL APPARATUS

An experimental apparatus was designed and constructed to measure the effects and nature of the interaction. The final apparatus design was the result of several earlier experiments that were performed at ARL. The most recent large-scale experiments were the ones already mentioned by Rogers[1] that were performed in 1990. The multiple element interaction study described in this report began with a small two-element discharge system[2] to determine the size of the effects that might be observed and to determine what equipment would be required for a larger study. The delivered energy of this first multiple element system was approximately 70 J per channel, with voltages of about 2 kV. High speed photographs of the bubbles generated by this system, while not very useful quantitatively, aided greatly in the insights that went into developing the model outlined in Chap. 3. Indications in these early efforts were that the breakdown times were far too stochastic to allow the elements to interact effectively, as the first element to fire would often be near its collapse before the second element would fire. An investigation was therefore made into the design of the electrodes, calculating numerically the relative electric field strengths between various designs, in hopes of improving the breakdown characteristics. The dimensions used for the

electrodes in this experiment were determined by combining the information from those calculations and some empirical studies.

Other benefits were realized by going to slightly higher energies. An increase in energy serves to increase the bubble period (see Eq. (2.51)), allowing a greater time for the elements to interact, while simultaneously removing some of the variability in the breakdown time (because of the higher voltages). The maximum energy that could be used for these studies was limited by the experimental facilities, motivated by the desire for acoustic signatures without reflections. Preliminary modeling of interaction effects[3] gave indications of interesting experiment parameters for multiple element studies, and provided insight regarding the size of the effect to be observed.

6.1 Experiment Layout

All the multiple element data were taken at the ARL Lake Travis Test Station in September 1992. The general layout at Lake Travis is shown in Fig. 6.1, and photographs of the equipment in the staging area at Applied Research Laboratories are shown in Figs. 6.2 and 6.3. The equipment was positioned along the edge of a floating barge on the lake, and the water depth under the barge ranged from about 22 to 30 m. The lake surface ranged from very calm to very rough (wave heights up to 1 m), and the water temperature was about 27°C. A clear acoustic signature (without reflections) was obtained by carefully positioning the electrodes and hydrophones as shown in Fig. 6.1, and considering the propagation times between the electrodes, hydrophones, and the lake surface and bottom. These

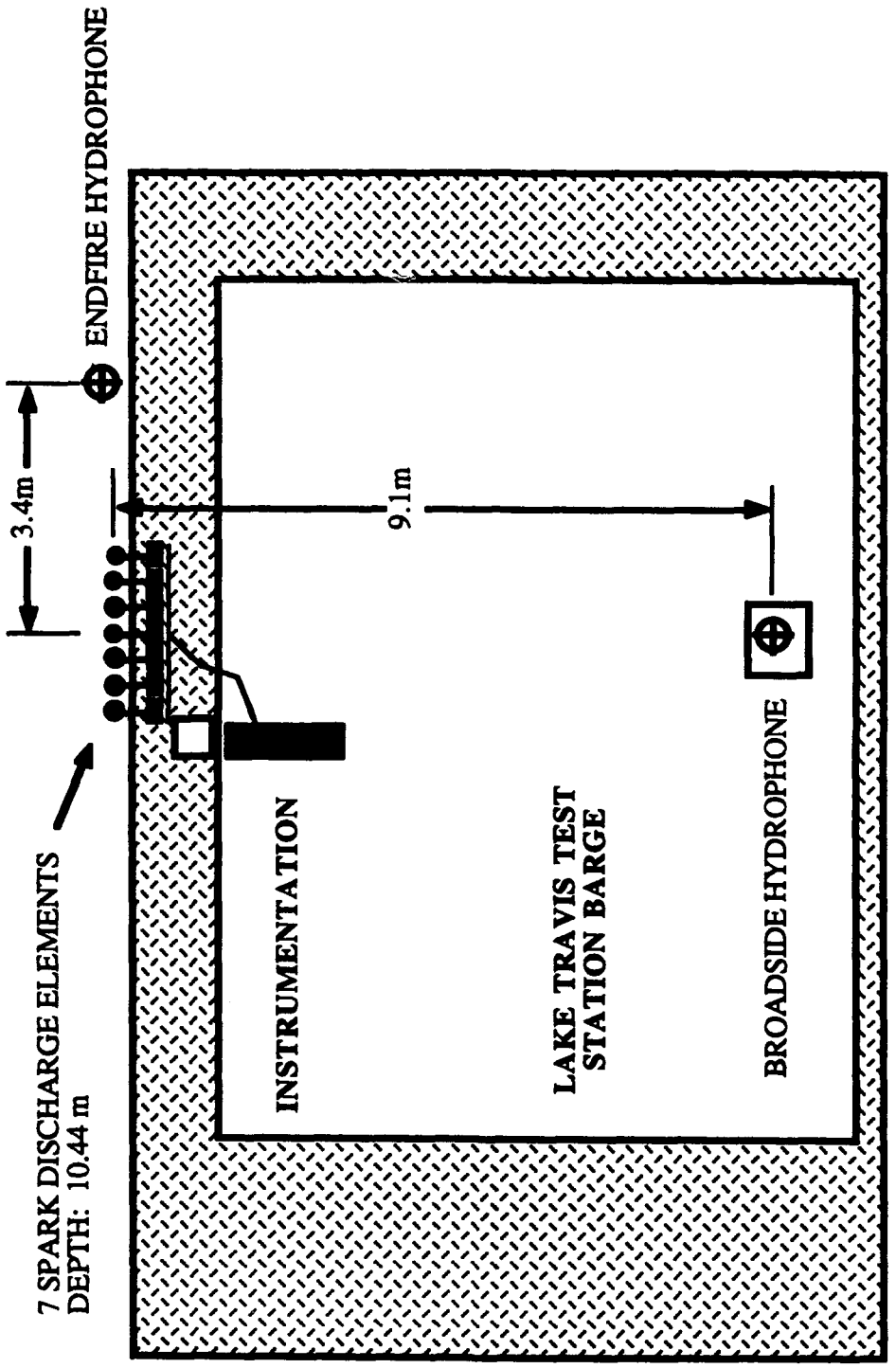

FIGURE 6.1
EXPERIMENT SCHEMATIC

AS-93-283

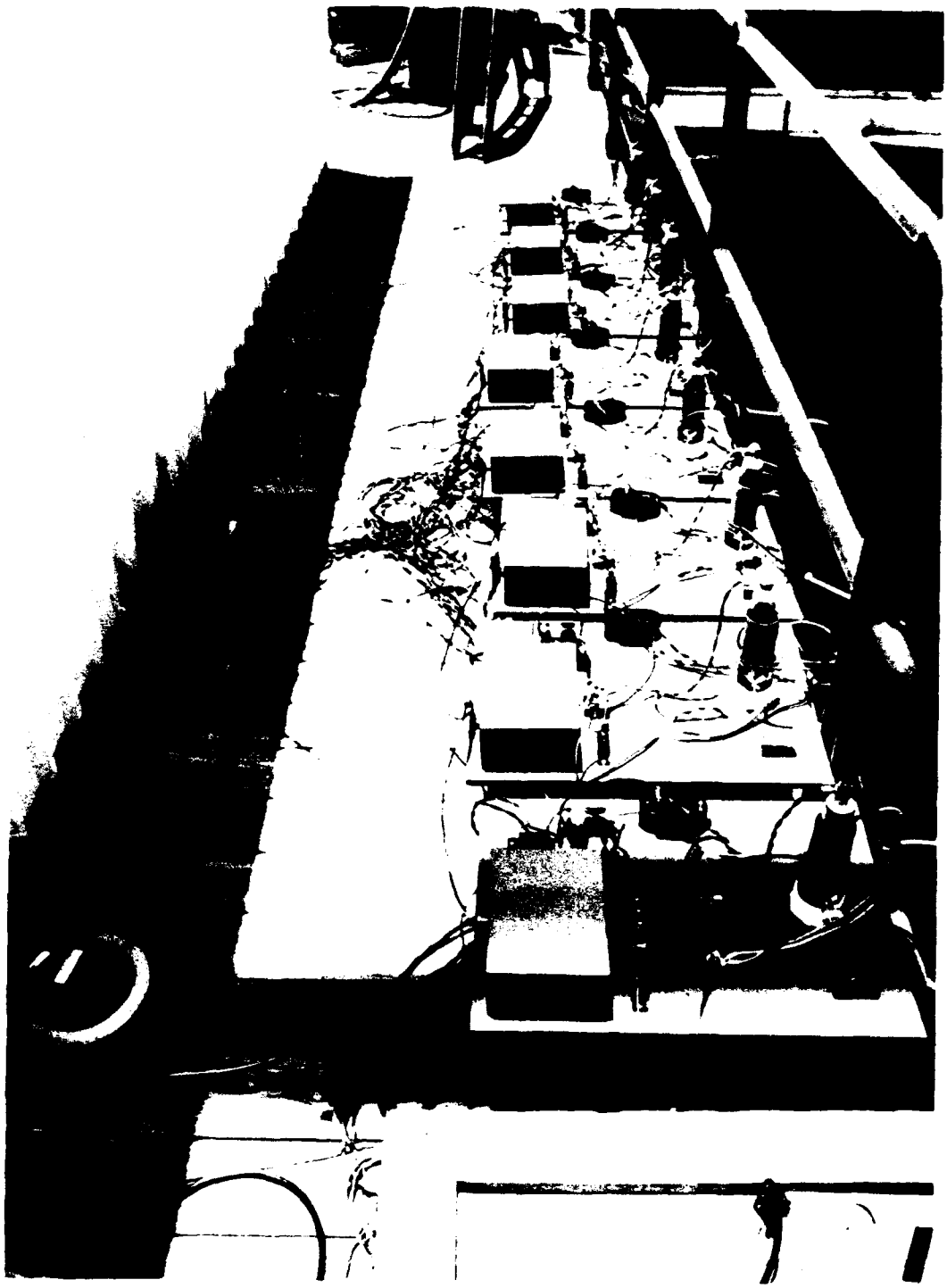

FIGURE 6.2
SPARK DISCHARGE EQUIPMENT

7819-23

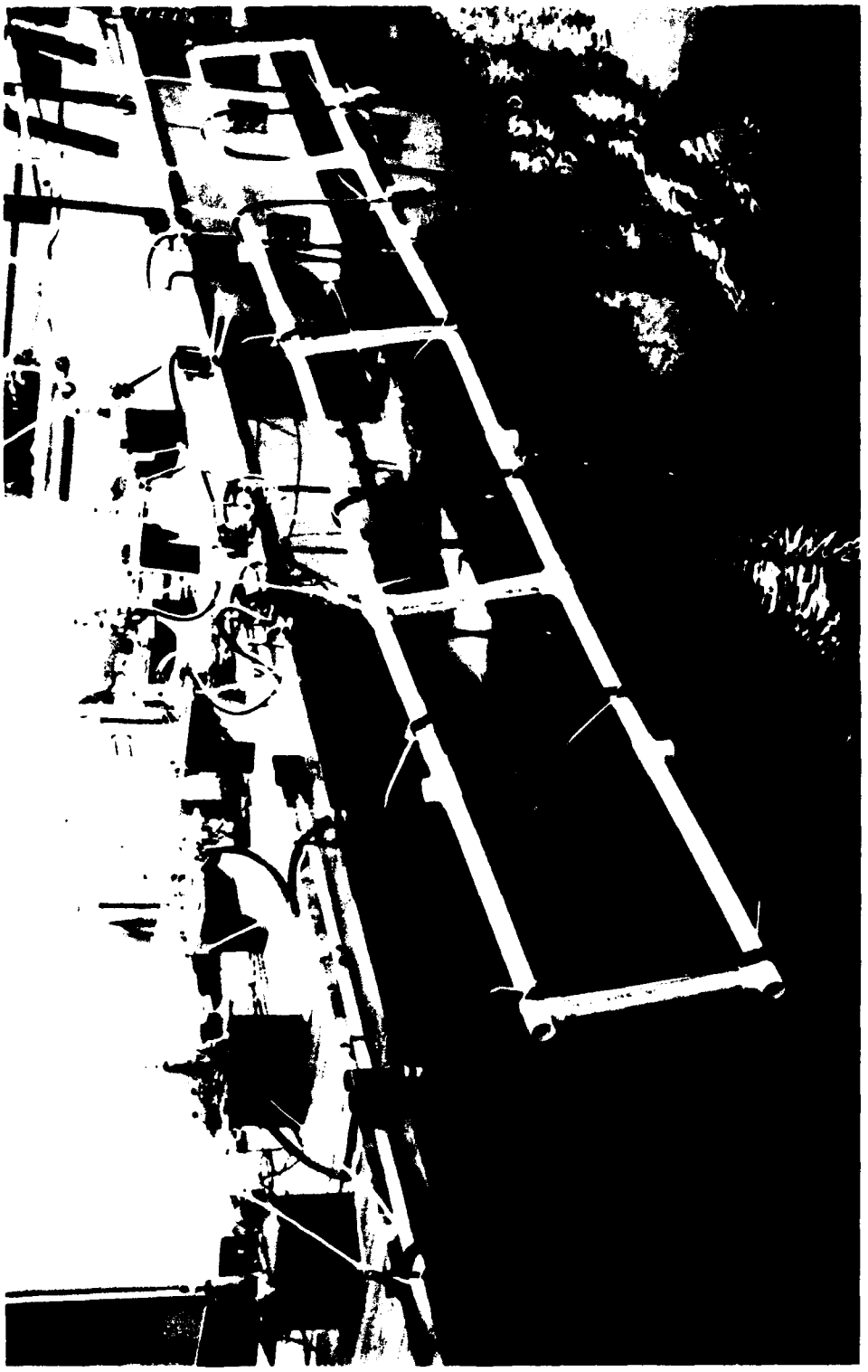

FIGURE 6.3
SPARK DISCHARGE EQUIPMENT AND RACK

restrictions limited the hydrophone distance from the array, because acoustic signatures without reflections could not be obtained for the largest number of elements at the widest spacing. To carefully control spacing between the bubbles, the junctions were mounted on a rack constructed of 1½ in. PVC (PolyVinyl Chloride), visible in Fig. 6.3. Several "tee" connections were used to keep the rack open to the water. This served to reduce the number of air bubbles trapped inside the rack. Seven elements were fastened to the rack at several uniform spacings between elements. Data taken at each spacing included sets of three, five, and seven elements at the nominal spacing, sets of three elements using two and three times the nominal spacing, and sets of each single element. The single element data distributed in this way turned out to be very valuable in tracking down problems during analysis. The spacings may be characterized by the maximum diameter of an isolated bubble using Eq. (2.47) to determine the maximum diameter from the bubble period. The spacings used are shown in Table 6.1. All measurements were made from the center of the rack to reduce any accumulated error in the spacings. The error at each position was determined to be a maximum of about 0.013 m, so the error between any two elements was less than about 0.026 m.

To provide a consistent reference in discussing the data, the elements were numbered from one end, 1 through 7. The center channel, with voltage and current information recorded for each of the multiple element shots, was element number 4. The data sets then consisted of the data sets shown in Table 6.2 taken at each nominal spacing.

TABLE 6.1

EXPERIMENT CONFIGURATIONS

Element Spacings		Number
(meters)	(bubble diam.)	of Elements
2.13	22.4	3
1.45	15.2	3
1.42	14.9	3
0.97	10.1	3
0.71	7.5	3, 5, 7
0.57	6.0	3
0.48	5.1	3, 5, 7
0.38	4.0	3
0.29	3.0	3
0.19	2.0	3, 5, 7
0.10	1.0	3, 5, 7

TABLE 6.2

DATA SETS AT EACH SPACING

Total Number of Elements	Element Numbers
7	1 – 7
5	2 – 6
3	3, 4, 5
3	2, 4, 6
3	1, 4, 7
1	Each (7 Groups Taken)

A total of about ten shots were usually taken for each set, except for the individual elements, where six shots were taken on the center element (which had full instrumentation), and four shots on each of the other elements (which had only limited instrumentation).

6.2 Spark Discharge Equipment

The experimental apparatus consisted of seven individual spark discharge channels. A simple diagram of a typical spark discharge system was shown in Fig. 1.1. The entire circuit for a single channel is shown in Fig. 6.4. Each channel used a 50 μF capacitor as its primary energy storage device. The capacitor was discharged through an ignitron tube to a 12 meter long eight-conductor cable. Each conductor in the cable was 10 gauge stranded copper. Four conductors in the cable were used for each polarity. An electrode junction for mounting the electrodes was attached at

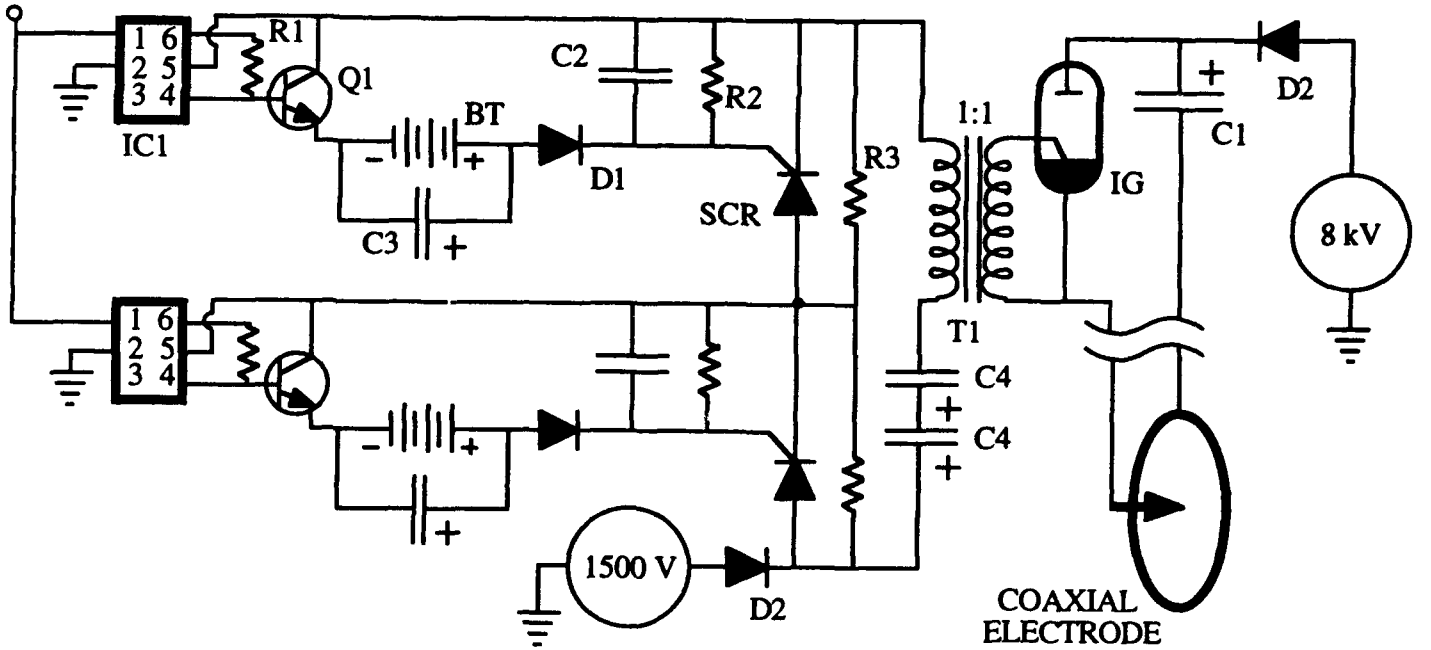

IC1	4N26 OptoIsolator	T1	HV Isolation Transformer
Q1	D44H11 NPN Transistor	BT	3 X 9 V Batteries
D1	1N4007 Rectifier	IG	EEV BK7218H Ignitron
D2	ECG 548 12 kV Rectifier	SCR	IRKT26-10 SCR
C1	50 µF Discharge Capacitor	R1	10 kΩ, 1/8 W
C2	0.012 µF	R2	1 kΩ, 1 W
C3	10 µF Tantalum	R3	1 MΩ, 2 W
C4	0.5 µF, 3000 V		

FIGURE 6.4
DISCHARGE CIRCUIT DIAGRAM

AS-93-286

the bottom of the cable. This junction and the electrodes are discussed in the next section.

An ignitron tube is a gas discharge tube, able to carry heavy currents and control high voltages. The tube used was an EEV BK7218H. This ignitron has a molybdenum anode and is intended for use in capacitor discharge applications. An external excitation circuit was required to fire the ignitron. The excitation circuit used an International Rectifier dual thyristor module IRKT26-10 to switch a pair of ½ μF capacitors charged to 1600 V into the ignitron igniter pin through a high voltage isolation transformer. The thyristor module was triggered by a dual optically isolated circuit in response to a pulse input. All circuits and the ignitron tube were mounted on a ½ in. sheet of gray PVC that was fastened to the top of the primary capacitor. A sideview photograph of the circuit layout is shown in Fig. 6.5.

6.3 Junction and Electrodes

The junctions visible at the bottom of the cables in Fig. 6.3 were constructed to terminate the cables and provide flexible attachments for the electrodes. The junctions were designed in such a way as to be readily adaptable to several different types of electrodes but easy to build and use. The body of each junction was a phenolic cylinder (3 inch diameter) that held a brass bushing for connection of the anode from below and grounding points for the cathode. The cables were attached at the screws on top of the cylinder, with current carried to the center bushing by means of a brass plate and to the cathode points by screws through the phenolic cylinder. After the cables were attached, the entire top of the cylinder was encased in urethane to provide stress relief and insulation.

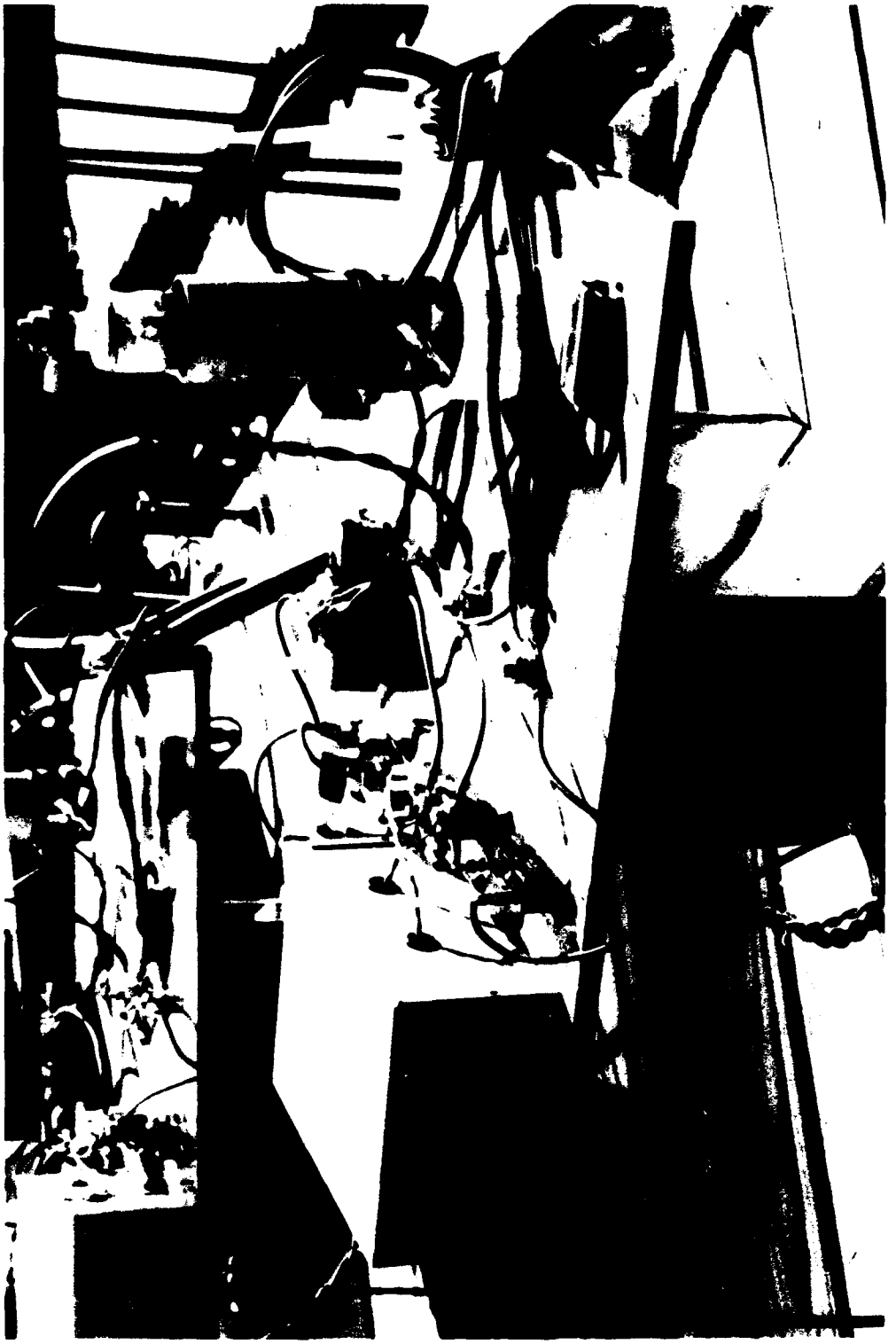

FIGURE 6.5
DISCHARGE CIRCUIT LAYOUT

Several designs have been used for electrodes to generate spark bubbles for sound source research and for lithotripsy. The typical approach is to use two electrodes in a point-point or point-plate gap configuration. However, the electrodes used in these experiments were constructed in a coaxial geometry, with a center anode and an outer surrounding cathode. An end-view of the electrode and the junction discussed above is shown in Fig. 6.6. The coaxial electrode design combines two electrode designs outlined in the literature. The simplest of these is the coaxial cable electrode, used extensively by Naugol'nykh,[4] consisting simply of a piece of coaxial cable with the insulation stripped back to provide a remote ground. This electrode is very simple to build, but does not last very long and is not consistent in its behavior over a number of shots. Guman developed an electrode he termed the "inverse–pinch" design.[5] This was essentially a cylindrical electrode, with two disks along the cylinder separated by an insulator. The current flowing in an arc from the anode to the cathode in this design will be forced out away from the electrode as a result of the magnetic forces on the electric current. This effect is the reason the electrode was termed the inverse–pinch electrode, in reference to the opposite effect of an electric current to pinch in on itself due to the magnetic forces from its own current. The coaxial cable electrode has these benefits but suffers because of the durability problems. The electrodes used in these experiments are both coaxial and inverse pinch. The general design was developed in earlier experiments at ARL, and minor modifications of the design suited it for use in these experiments also. This electrode unit was designed in such a way that it could be easily replaced in the apparatus. Attaching the unit to the junction required

FIGURE 6.6
COAXIAL ELECTRODE AND JUNCTION

screwing it into the brass bushing and attaching ground straps from the cathode to the grounding points on the junction. The anode (center electrode) is machined from press-sinter-infiltrated tungsten-copper. This material has electrical conductivity 41% that of copper and Rockwell Hardness B of 103. It was developed for use under extreme arcing conditions in gas and oil circuit breakers and power switching equipment. It was chosen for its good durability and resistance to erosion. The cathode (outer electrode) is machined from yellow brass, and is easily machinable. The brass is more susceptible to erosion, but this is not a major problem for the cathode. After the two electrodes were machined, the assembly, as shown in the figure, was potted with urethane to provide insulation and structural support. The urethane used for the electrode potting and for the junction was PR–1547 polyurethane, a high tensile strength chemically curing compound with good resistance to cold flow and 300 V per mil dielectric strength. A compound of PR–1525 was also tried, but proved unsatisfactory structurally. The electrode dimensions used were the following:

0.381 cm	Anode diameter
0.762 cm	Cathode inner diameter
1.43 cm	Cathode outer diameter
0.191 cm	Spark gap

These electrodes typically lasted a few hundred shots at the discharge energies that were used.

6.4 Instrumentation

All the data taken were stored on a pair of Nicolet Model 4094–C Digital Storage Oscilloscopes with Model 4562 plug-in modules. These oscilloscopes had a maximum sampling rate of 2 MHz, a bandwidth of about 600 kHz, and 12-bit resolution.

Electrical data were taken on one channel at a time in these experiments. Voltage at the electrode was measured on the center channel only by shunting the anode and cathode with a high known resistance (10 kΩ) at the junction and measuring the resulting current with a Pearson Model 110 Current Transformer, passing the wire through the transformer ten times. Current measurements were made on each channel by passing the power cables directly through Model 101 transformers from the same manufacturer. The output from the transformers measuring the current was attenuated by a factor of ten with a decade attenuator.

Two transducers (hydrophones) provided acoustic data. Most of the signatures shown were taken with a Naval Research Laboratory USRD Series F42C Hydrophone Serial 121. This hydrophone had a reasonably flat frequency response from about 1 Hz - 20 kHz. The response was low from about 20 - 60 kHz, and a strong resonance existed at about 80 kHz. This resonance was visible as a ringing on the data, excited by the large amplitude pressure spikes in the acoustic signature. A TR225 hydrophone was also used to aid in determining bubble periods from an endfire position. Although the TR225 had a poorer frequency response, it did not exhibit the strong resonance of the F42C and was therefore useful in picking out certain features of the acoustic signature.

Several times in the previous chapters the term "farfield" was mentioned. The term discussed previously referred to the farfield of the bubble, and is a different farfield than the one normally considered when discussing arrays of elements. A measurement is generally considered to be made in the farfield of an array if the distance between the measurement location and the array is much greater than the separation between elements. The measurement distance used was about five times greater than the largest separation used for three elements, and about 15 times greater than the largest separation used for five and seven elements, so these measurements were barely made in the farfield. A larger separation between hydrophone and array was not possible because of the restrictions indicated earlier. At the smaller and intermediate separations, the measurement distance was 20 to 100 times the distance between elements, so for these cases the farfield conditions were satisfied.

6.5 Experiment Parameters

The primary spark discharge capacitors were typically charged to between 2 and 6 kV, resulting in stored energies of 100 - 900 J, with about 5 kV (625 J) being used almost exclusively for the multiple bubble studies. The discharge circuit was somewhat under damped, and the energy delivered to the electrodes was about 45% of the stored energy. Although the energy delivery was more efficient at lower voltages, the variation in the breakdown time increased. Because of the difficulties in determining the bubble periods from the acoustic data, it was advantageous for the discharges to begin simultaneously; therefore, the highest possible voltages were used. The charging supply used was capable of about 8 kV, and the ignitrons

were usable to about 15 kV. A maximum charging voltage of 6 kV was chosen based on some preliminary destructive tests that were performed, and a standard voltage of 5 kV provided a good compromise between breakdown time variability and equipment durability. When the capacitors were charged to 5 kV, the peak current was typically about 15 - 20 kA. As was mentioned in Sec. 3.5, the discharges tended to be under damped, with three measurable power lobes. A typical load voltage and discharge current were shown in Fig. 1.2, and the associated discharge power and energy were shown in Fig. 3.5. The discharge times were typically a total of about 100 to 120 μs, with each lobe about 30 - 40 μs long. As can be seen in the plots, the current in these experiments reversed to about 40% of its peak value, while the final lobe reached about 20% of the peak current. The power typically peaked at about 10 MW.

6.6 Single Bubble Results

It was mentioned in Sec. 6.1 that at each separation considered in the multiple element experiments, data were also taken for each single element. These data were instrumental in determining the statistics of the spark-generated bubbles, particularly with respect to the variation in the bubble period. The charging voltage was fixed at 5 kV for these experiments, but the energy and bubble period each tended to vary somewhat with each discharge. An attempt to normalize the bubble period according to the exact energy discharge did not result in sufficiently improved results, so the bubble periods were not normalized for this analysis. The distribution of electrical energy delivered is described by the mean and standard

deviation:

$$\overline{E_{\text{discharge}}} = 270\ \text{J}, \overline{E_{\text{discharge}}} = 270\ \text{J}, \qquad \sigma = 21\ \text{J} \quad . \tag{6.1}$$

A histogram showing the distribution of the bubble periods is shown in Fig. 6.7. The mean value and standard deviation for the bubble period were the following:

$$\bar{\tau} = 6.07\ \text{ms}, \qquad \sigma = 0.22\ \text{ms} \quad . \tag{6.2}$$

The breakdown times tended to group around two mean values, as shown in Fig. 6.8. The two mean values, and their standard deviations were these:

$$(14\%) \qquad \overline{t_{\text{init},1}} = 75\ \mu\text{s}, \qquad \sigma_1 = 23\ \mu\text{s} \tag{6.3}$$

$$(86\%) \qquad \overline{t_{\text{init},2}} = 457\ \mu\text{s}, \qquad \sigma_2 = 69\ \mu\text{s} \quad . \tag{6.4}$$

The percentages listed to the left indicate the percentage of the time that a given breakdown time fell into one group or the other.

The reason that the breakdown times exhibited this dual distribution is unknown. One hypothesis is that the charging voltages used in combination with the dimensions of the electrodes led to breakdowns of the gap that were usually in the "thermal" breakdown regime but occasionally in the "streamer" breakdown regime. These two regimes characterize the details of the physical processes involved in the bridging of the gap between the anode and the cathode. The work by Martin[6] and Naugol'nykh[7] describe these two processes. In the thermal breakdown, the small current that flows before the main discharge heats the water and forms a gas bridge between the two electrodes. This process is the slower of the two, with the breakdowns sometimes taking several ms. The streamer breakdown occurs at higher electric field strengths (about 36 kV/cm),[4] and results when narrow streams of plasma form at the tip of the anode. The growth of these streamers is driven by the electric field strength at the end of the streamer. This

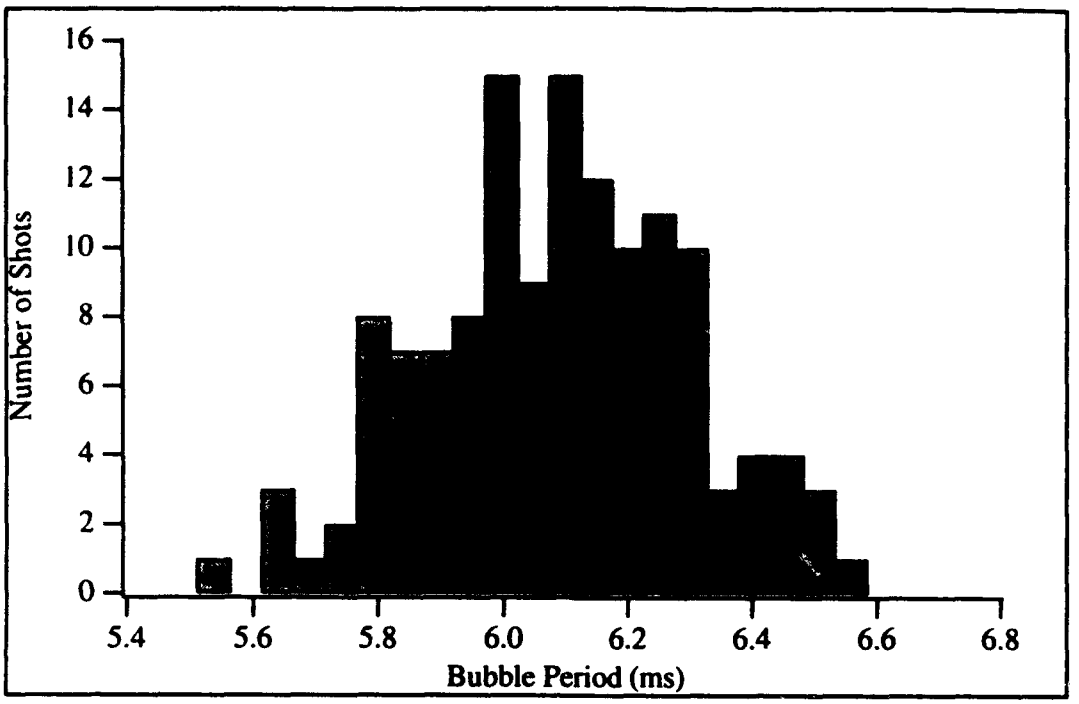

FIGURE 6.7
BUBBLE PERIOD HISTOGRAM

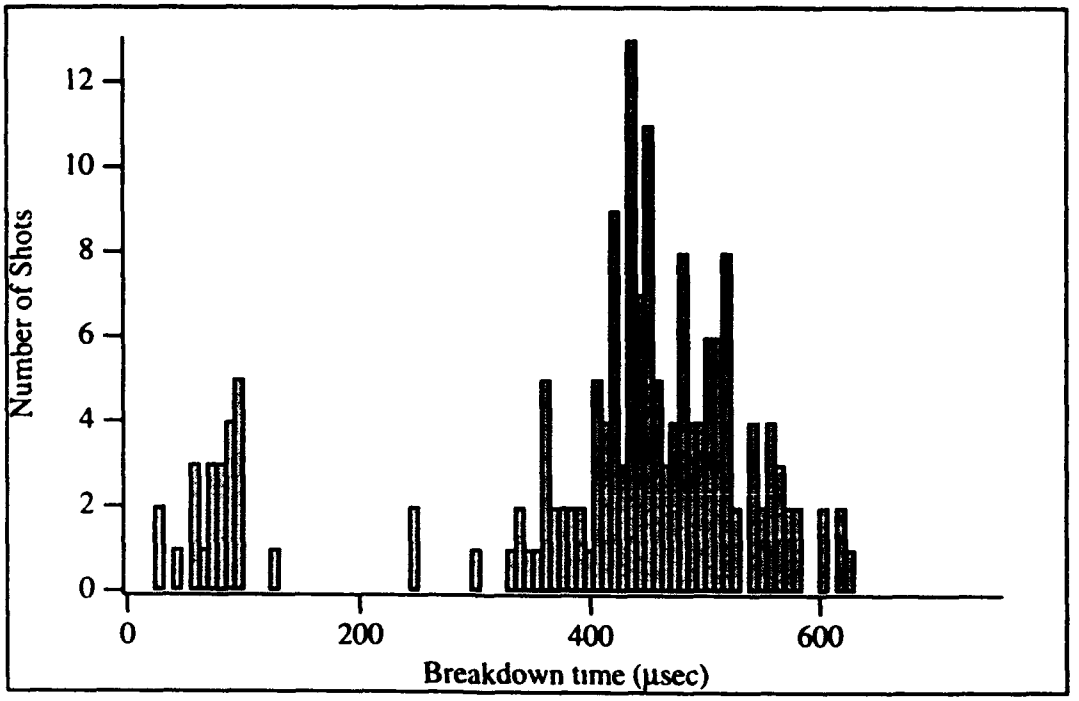

FIGURE 6.8
BREAKDOWN TIME HISTOGRAM

AS-93-289

process is much faster than the thermal breakdown, with breakdown times on the order of 10 to 100 μs. The two breakdown regimes have breakdown times consistent with the times observed in these experiments. The electric field strength of the electrodes used was estimated using the numerical simulation mentioned at the beginning of this chapter, and was found to be approximately 6.5 (kV/cm)/kV. At a capacitor voltage of 5 kV, the electric field strength was therefore 30 - 35 kV/cm, placing the breakdown in the transitional regime between the two mechanisms, consistent with the dual breakdown characteristics observed.

One other point of support concerns the effect of the breakdown mechanism on the hydraulic efficiency. The hydraulic efficiency of these discharges was reported in Chap. 4 to be about 35%, which is slightly higher than the efficiencies reported in that chapter for the sea data. Ryabinin[8] found that the hydraulic efficiency was greatest for breakdowns near the transition between the two breakdown mechanisms, and reported values of 37 to 40%.

---

[1]R. L. Rogers, *Intermediate Energy Tests and Analysis of a Plasma Sound Source* (Applied Research Laboratories, The University of Texas at Austin, 1992), Report ARL–TR–92–15.

[2]J. A. Cook, "Studies of Various Electrode Configurations for a Plasma Sound Source," *J. Acoust. Soc. Am. Suppl. 1* **88**, S168 (1990).

[3]J. A. Cook, "Mutual Coupling Effects Between Elements in a Spark Source Array," *J Acoust. Soc. Am.* **90**(4), Pt. 2, 2350 (1991).

[4]K. A. Naugol'nykh and N. A. Roi, *ELEKTRICHESKIE RAZRJADY V VODE* (Nauka, Moskva, 1971) [English transl.: *Spark Discharges in Water* (Applied Research Laboratories, The University of Texas at Austin, 1987), Internal Report].

[5]W. J. Guman, "Study of an Inverse-Pinch Electric Discharge Sound Source," *J. Underwater Acoust.* **17**(3), 511–521 (1967).

[6]E. A. Martin, "Experimental Investigation of a High-Energy Density, High-Pressure Arc Plasma," *J. Appl. Phys.* **31**(2), 255–267 (1960).

[7]K. A. Naugol'nykh, "Electrical and Hydrodynamical Characteristics of an Impulsive Corona in Water," *Akust. Zh.* **13**(3), 417–426 (1967) [English transl.: *Sov. Phys. – Acoust.* **13**(3), 352–359 (1968)].

[8]A. G. Ryabinin and G. A. Ryabinin, "Gas-Bubble Energy in an Underwater Electrical Discharge," *Zh. Tekh. Fiz.* **46**, 881–884 (1976) [English transl.: *Sov. Phys. Tech. Phys.* **21**(4), 512–514 (1976)].

7. MULTIPLE BUBBLE RESULTS

A total of 360 shots were recorded from 25 - 29 September 1992, and the data from those shots are presented in this chapter.

7.1 Signatures

Typical acoustic signatures recorded in the multiple element studies at a separation of 0.48 m are shown in Figs. 7.1 (one element), 7.2 (three elements), 7.3 (five elements), and 7.4 (seven elements). Corresponding model acoustic signatures, calculated with the random input discharges mentioned in Chap. 1, are shown in Figs. 7.5 (one element), 7.6 (three elements), 7.7 (five elements), and 7.8 (seven elements). The variability in the breakdown times leads to a larger total width of the group of initial and collapse peaks, while the scatter in the bubble periods tends to increase the width of the group of collapse peaks. Besides these effects, both groups of peaks will tend to be wider at the largest separations because of geometric effects (the broadside hydrophone is farther from the end elements than from the center elements).

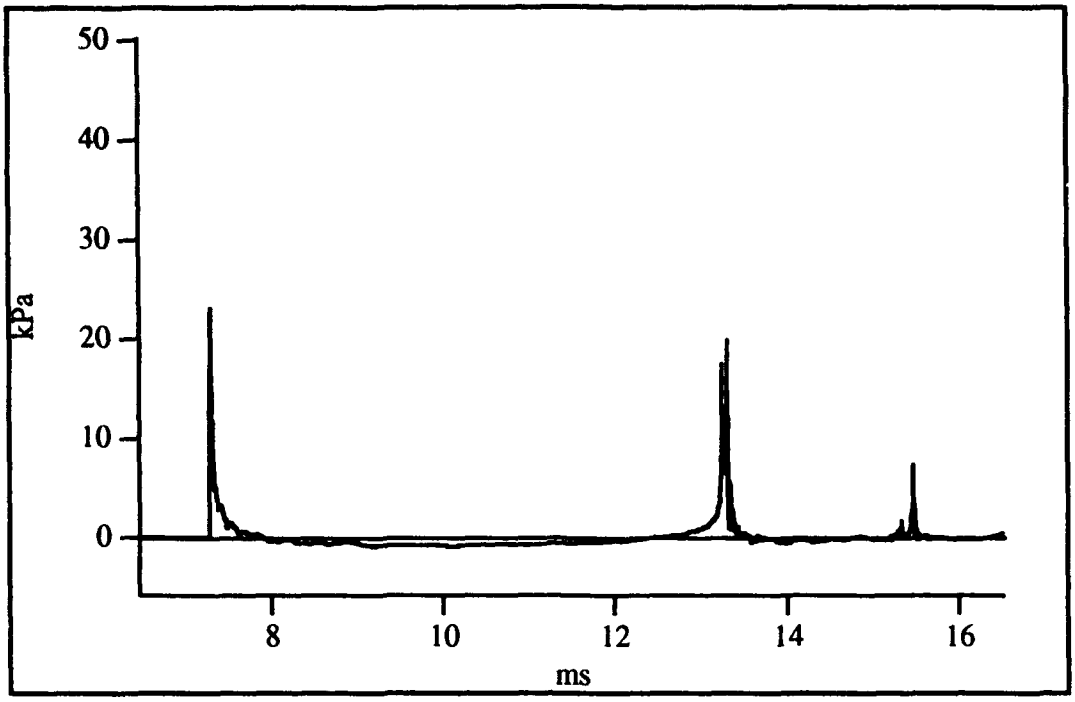

FIGURE 7.1
270 J MEASURED SIGNATURE, ONE ELEMENT

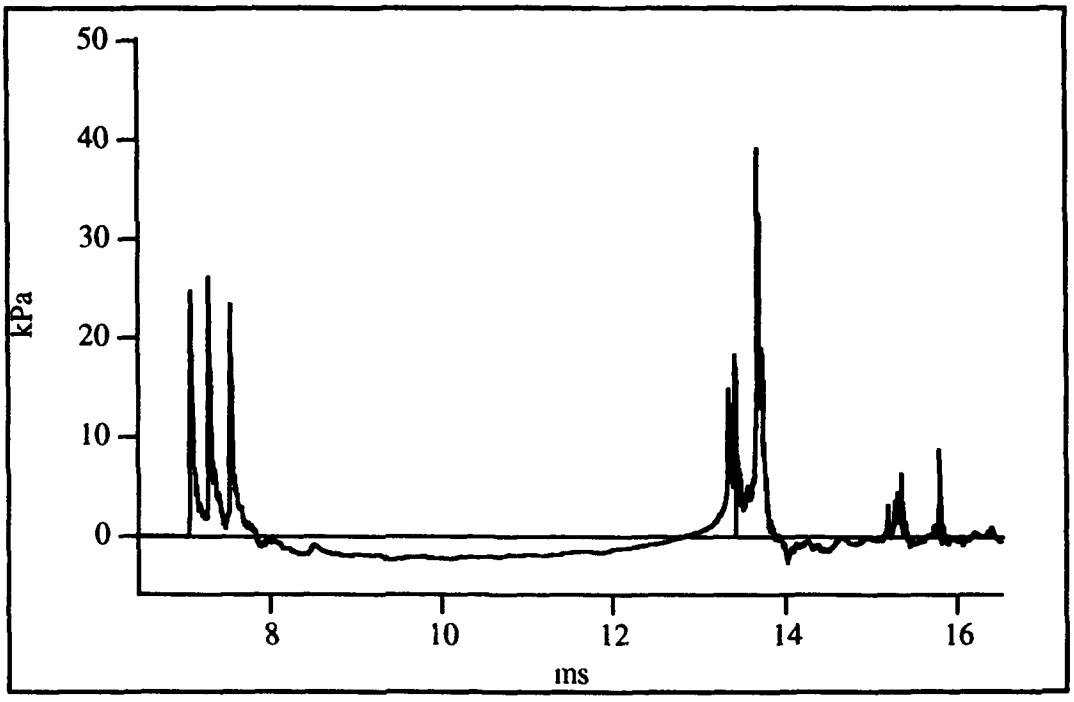

FIGURE 7.2
270 J MEASURED SIGNATURE, THREE ELEMENTS AT 0.48 m

AS-93-290

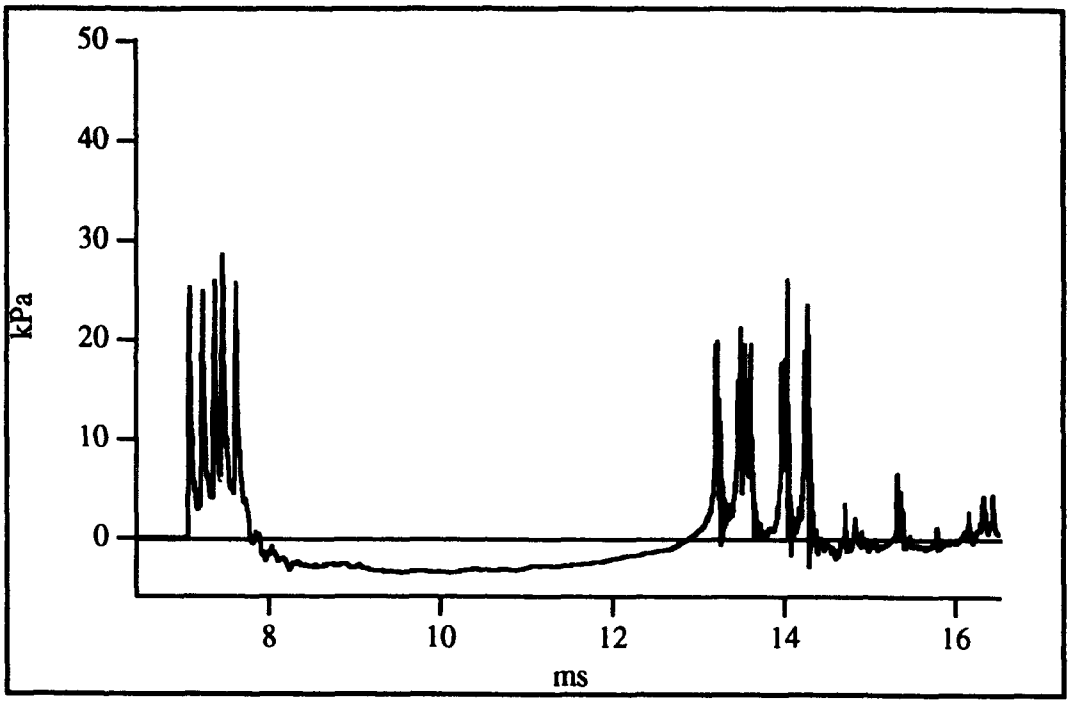

FIGURE 7.3
270 J MEASURED SIGNATURE, FIVE ELEMENTS AT 0.48 m

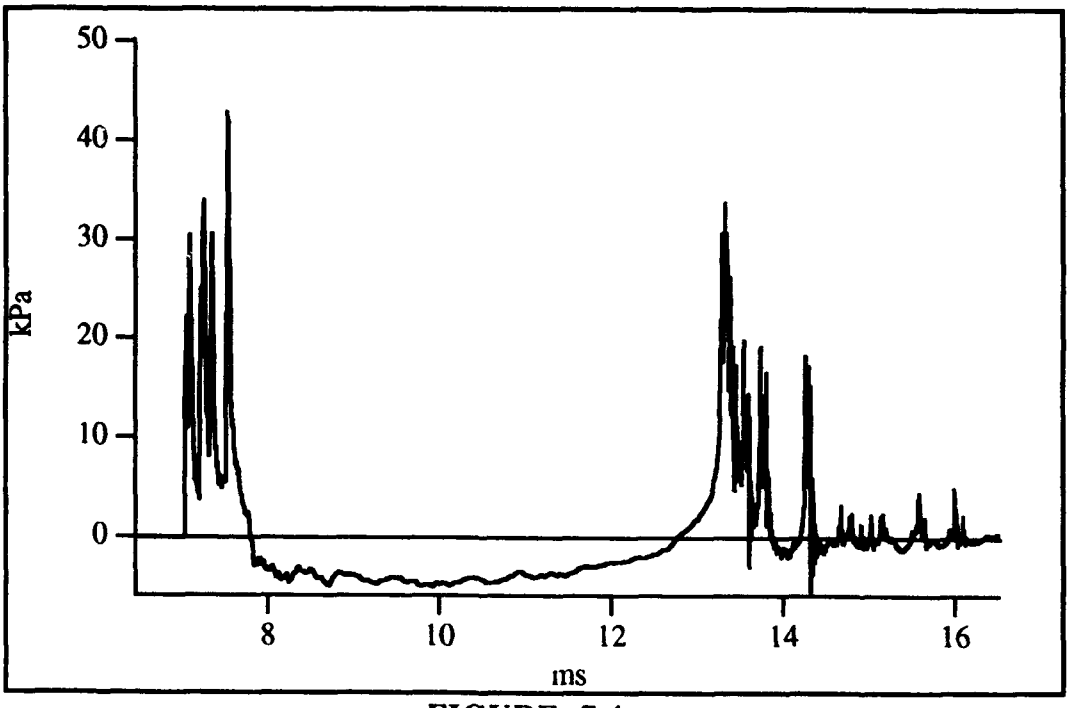

FIGURE 7.4
270 J MEASURED SIGNATURE, SEVEN ELEMENTS AT 0.48 m

AS-93-291

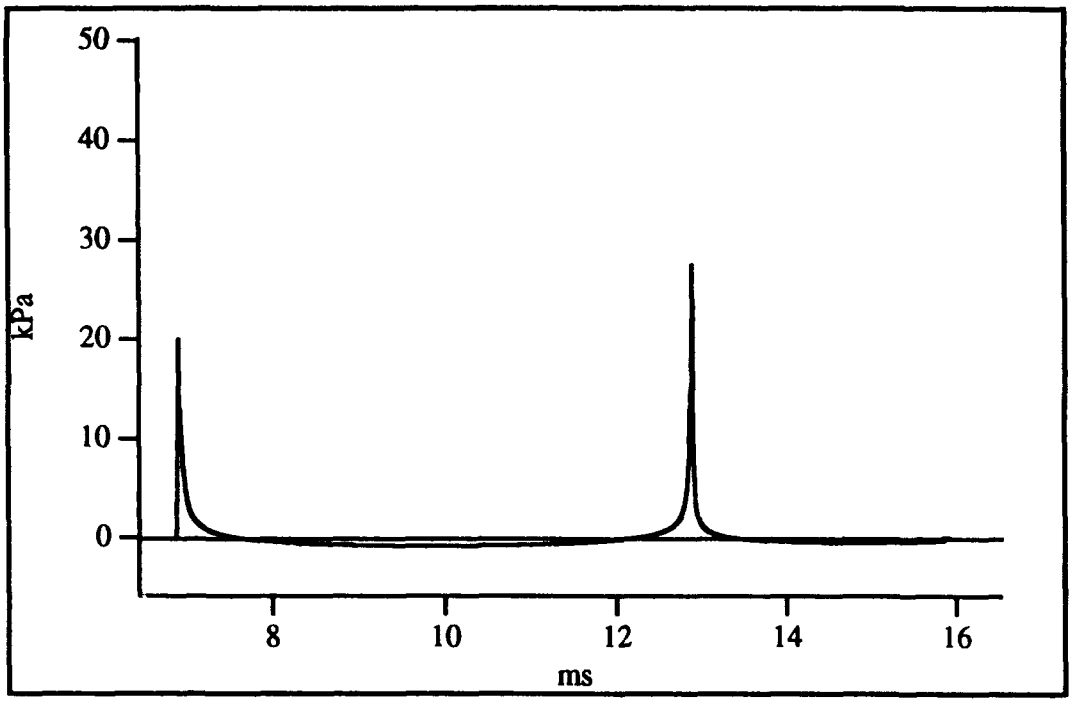

FIGURE 7.5
270 J MODELED SIGNATURE, ONE ELEMENT

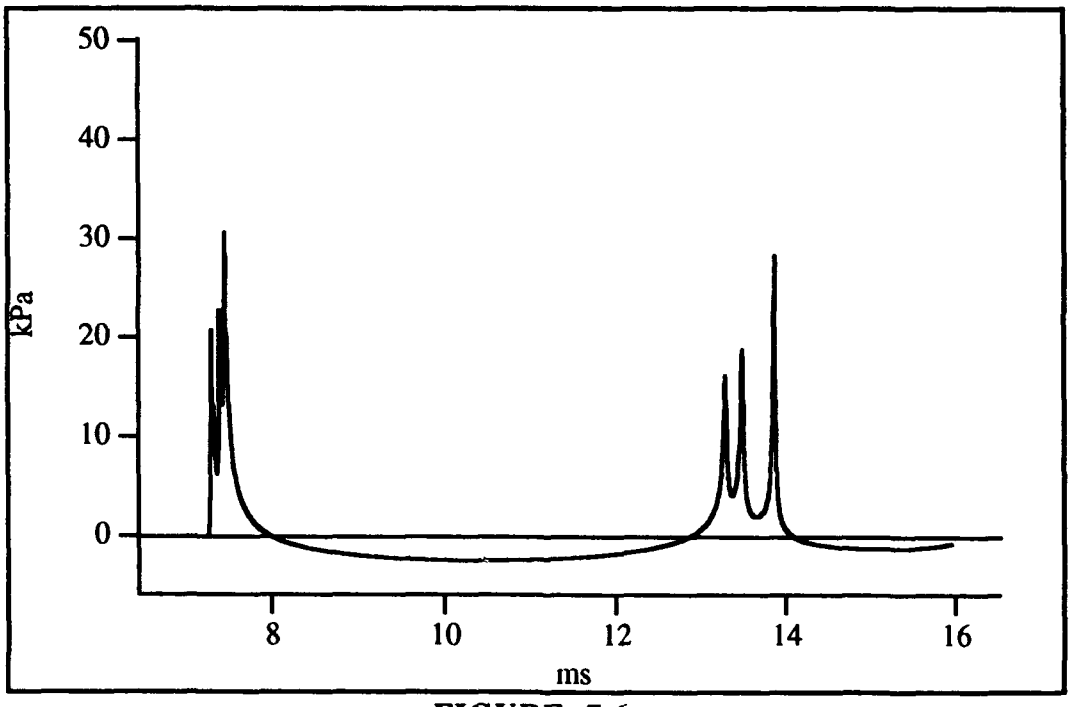

FIGURE 7.6
270 J MODELED SIGNATURE, THREE ELEMENTS AT 0.48 m

AS-93-292

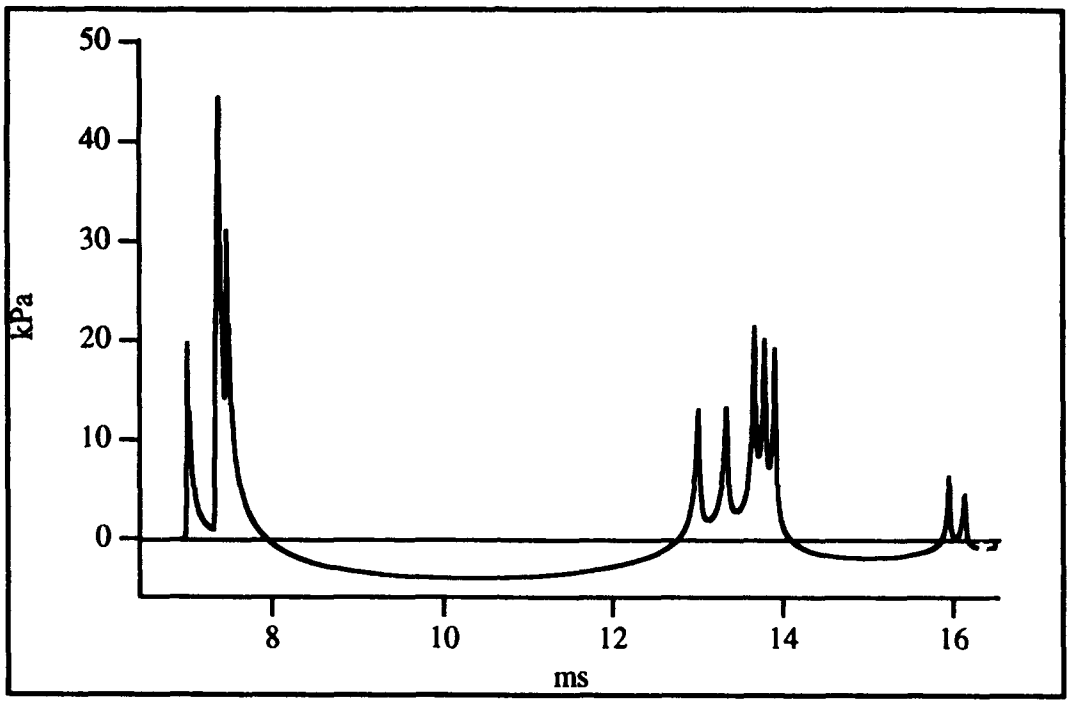

FIGURE 7.7
270 J MODELED SIGNATURE, FIVE ELEMENTS AT 0.48 m

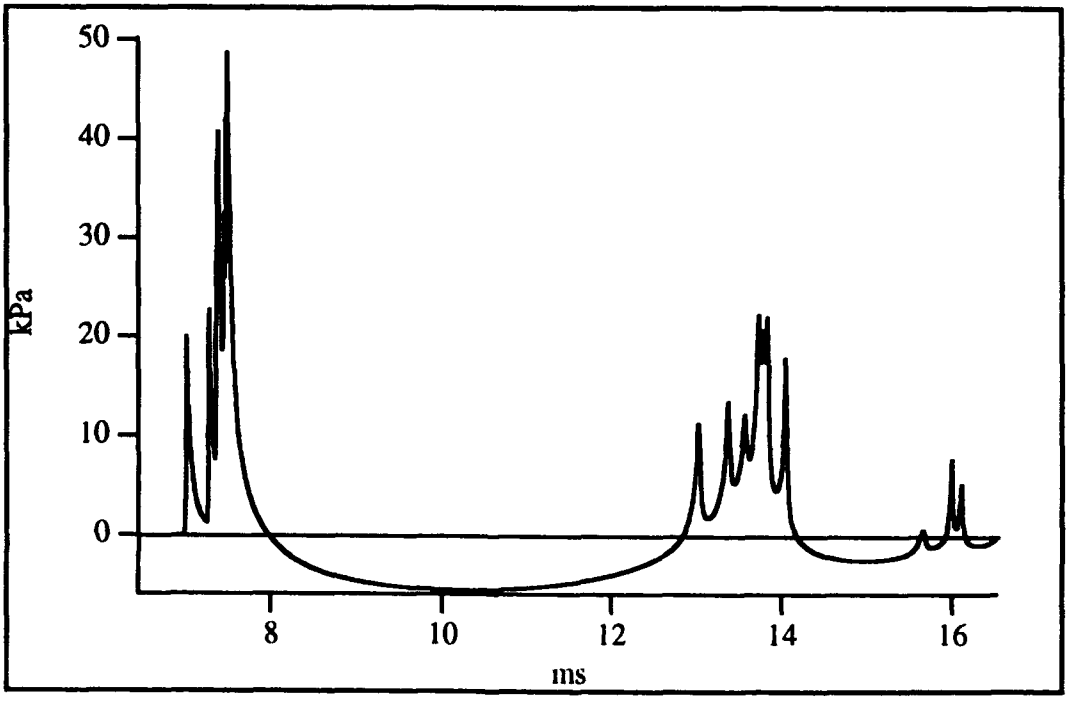

FIGURE 7.8
270 J MODELED SIGNATURE, SEVEN ELEMENTS AT 0.48 m

AS-93-293

7.2 Bubble Periods

The interaction between elements appears to be a function of element spacing and number of elements, and the bubble period appears to be one of the most easily observed manifestations of the interaction. One of the greatest difficulties in looking at this type of data is determining which part of the acoustic signature goes with which bubble. Two hydrophones were used to collect acoustic data. One hydrophone was placed in a broadside position, and one in an endfire position, as labeled in Fig. 6.1. The broadside hydrophone gives the main lobe of the acoustic beam pattern, while the endfire hydrophone gives valuable additional data on the bubble periods. The bubble periods are easily resolved by the endfire hydrophone when the separation between elements is large and a small number of elements is used. For instance, when the elements were at their largest separation (0.71 m), the endfire hydrophone had a resolution of 474 μs between elements, while the broadside hydrophone at the same separation had resolution of only 16 μs between the three center elements. Even with the resolution available from the endfire hydrophone, however, it was impossible to determine the individual bubble periods when more than three elements were used, and a slightly different approach had to be taken. The procedures were as follows.

One-Element Data: When only a single element was used, the bubble period was simply measured directly from the hydrophone signatures. If the bubble period was slightly different as measured by the two hydrophones (usually because of the different frequency response of the two hydrophones), the bubble periods from the two hydrophones were averaged.

Three-Element Data: When the separation was large, the bubble periods were well resolved, but as the elements were moved closer and began to interact, resolution of the bubble periods became more difficult. The process selected recorded the position of each peak on each of the two recorded signatures (broadside and endfire), and put combinations of the peaks together in such a way that unique bubble periods consistent with both hydrophone signatures could be determined. In cases where this could not be done, the data were discarded (this only happened on one or two shots). After the bubble periods for each data set were recorded, an Average and a Maximum Bubble Period were determined for each shot. These average and maximum bubble periods were then averaged within each set to determine the general behavior of the elements at a given spacing.

Five-, Seven-Element Data: It was impossible to determine individual bubble periods for all elements in any of the cases examined. A different method of analysis therefore had to be found. In examining the data, it was determined that the only clear objective measure of the bubble periods was in determining where the group of initial peaks and collapse peaks started and ended. The Minimum and Maximum Bubble Periods were then determined by recording the times of the first and last expansion peaks and collapse peaks, as measured by the broadside hydrophone, and subtracting them to maximize and minimize the differences:

$$\tau_{max} = t_{collapse,2} - t_{expansion,1} \tag{7.1}$$

$$\tau_{min} = t_{collapse,1} - t_{expansion,2} \quad . \tag{7.2}$$

As was mentioned earlier, part of the spread in these bubble periods will be geometric (the distance from each of the elements to the hydrophone is slightly different), but the maximum effect from this will occur when the element separation is largest, and is not noticeable when the elements are at their closest separation. These minimum and maximum bubble periods were analyzed similarly to the bubble periods in the three-element case.

The bubble period as a function of element separation is shown in Figs. 7.9(a), 7.10, and 7.11(a) for each number of elements. On the five- and seven-element graphs, the data point at 22.4 bubble diameters is not a real data point, but is instead the average of the single isolated bubble data, with error bars at plus or minus one standard deviation. This point was placed at 22.4 bubble diameters for consistency with the three-element graph.

An examination of the data indicates a problem with the data sets that included element number 1 at a nominal spacing of 0.19 m. These sets include the seven-element data set at 2.0 bubble diameters and the three-element data set at 6.0 bubble diameters. The single element data for element number 1 at this spacing indicated that a minor problem affected the behavior of the bubble generated. Although the element continued to fire, it did so with a somewhat reduced bubble period. Because of the difficulty in replacing this data set, the data were examined in hopes of finding a reasonable method for dealing with the bad element. The five-element data set at this spacing and the other two three-element data sets at this spacing were unaffected, because they did not include element number 1. The

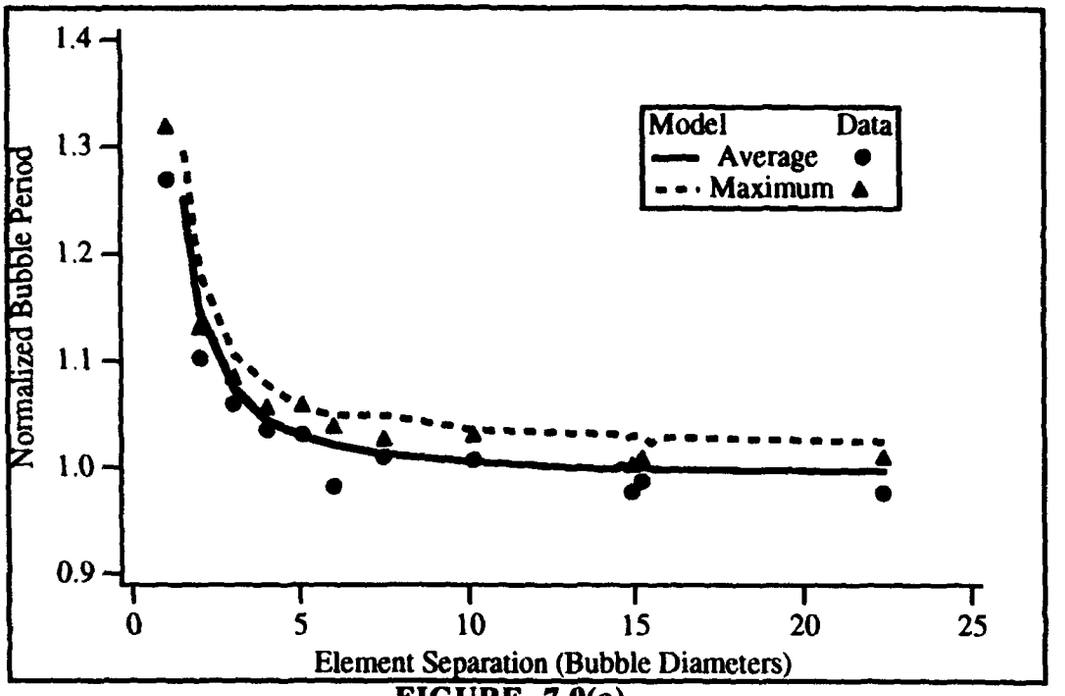

FIGURE 7.9(a)
THREE ELEMENTS, BUBBLE PERIOD

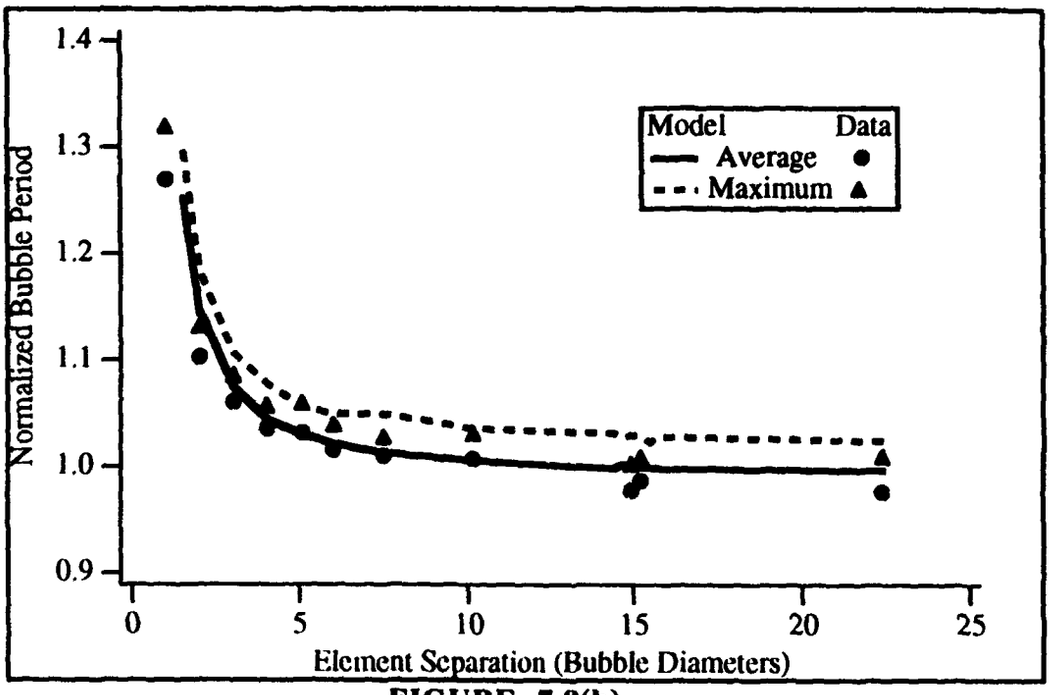

FIGURE 7.9(b)
THREE ELEMENTS, BUBBLE PERIOD: CORRECTED

AS-93-294

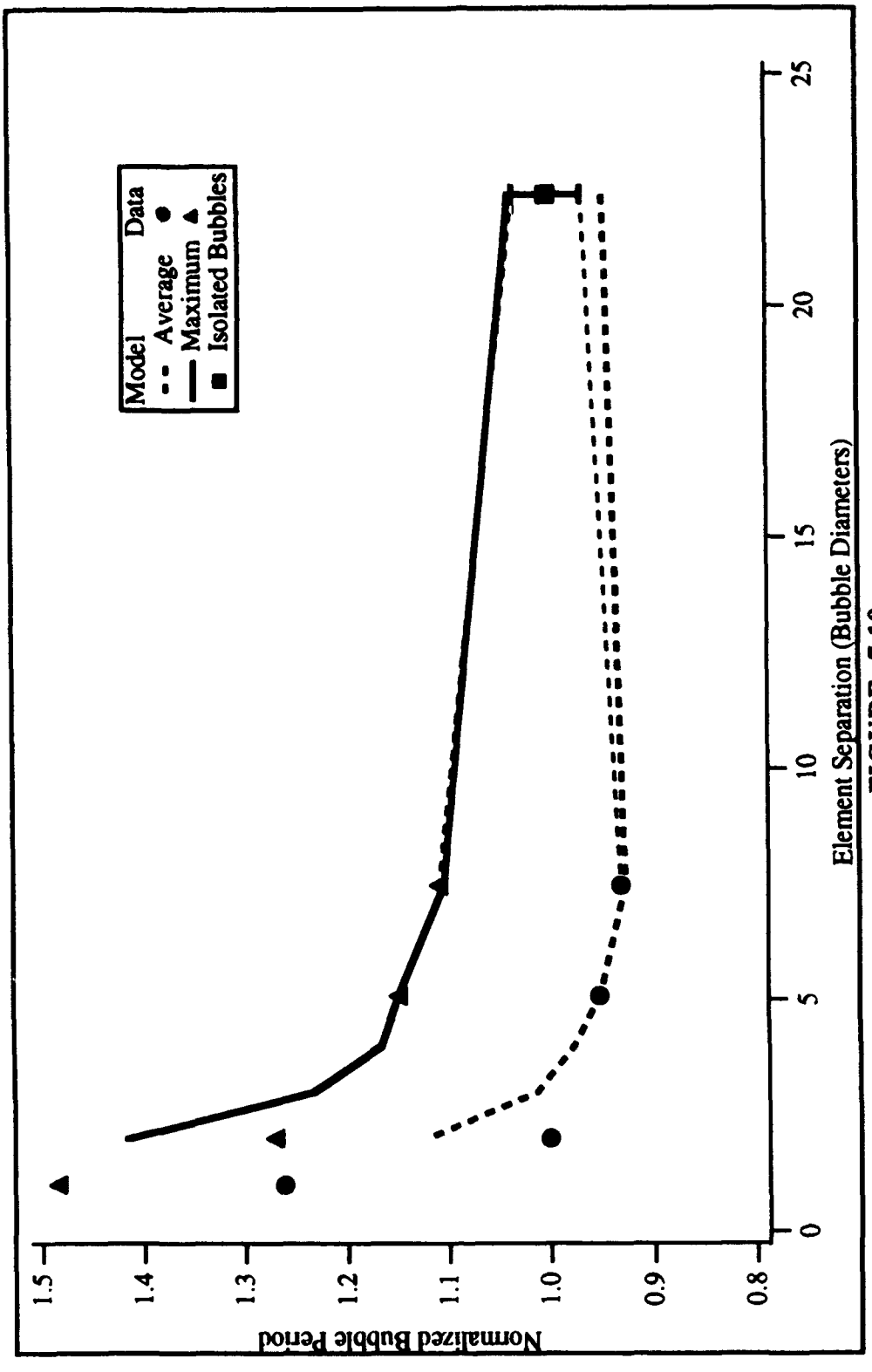

FIGURE 7.10
FIVE ELEMENTS, BUBBLE PERIOD

AS-93-295

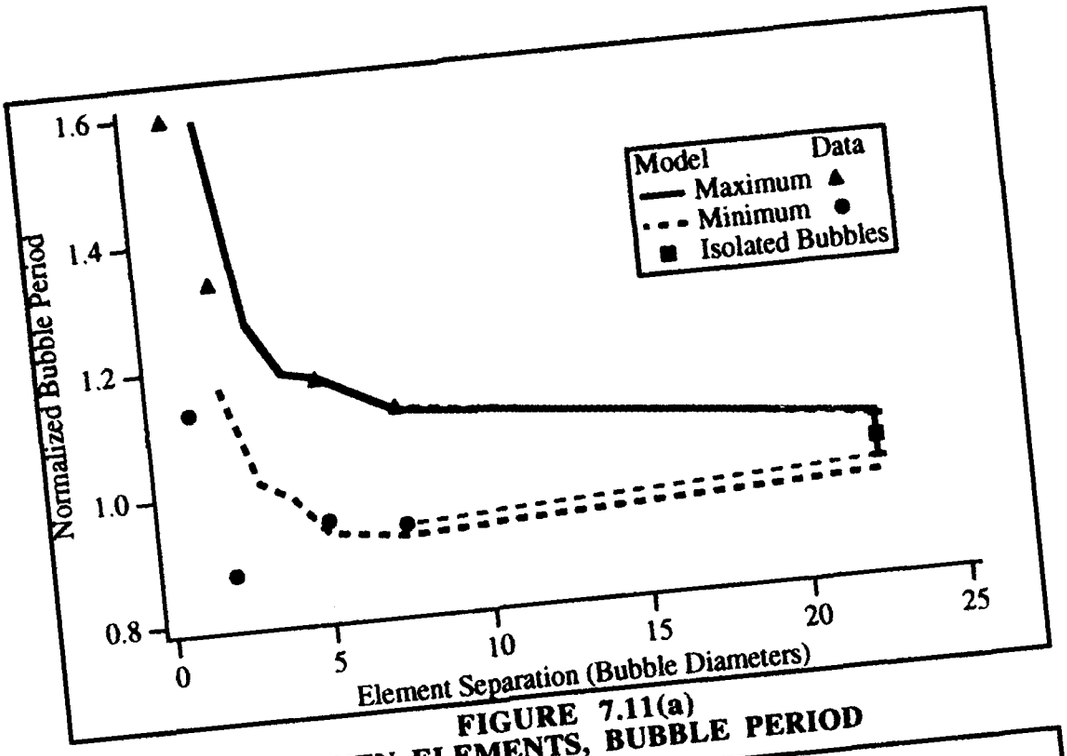

FIGURE 7.11(a)
SEVEN ELEMENTS, BUBBLE PERIOD

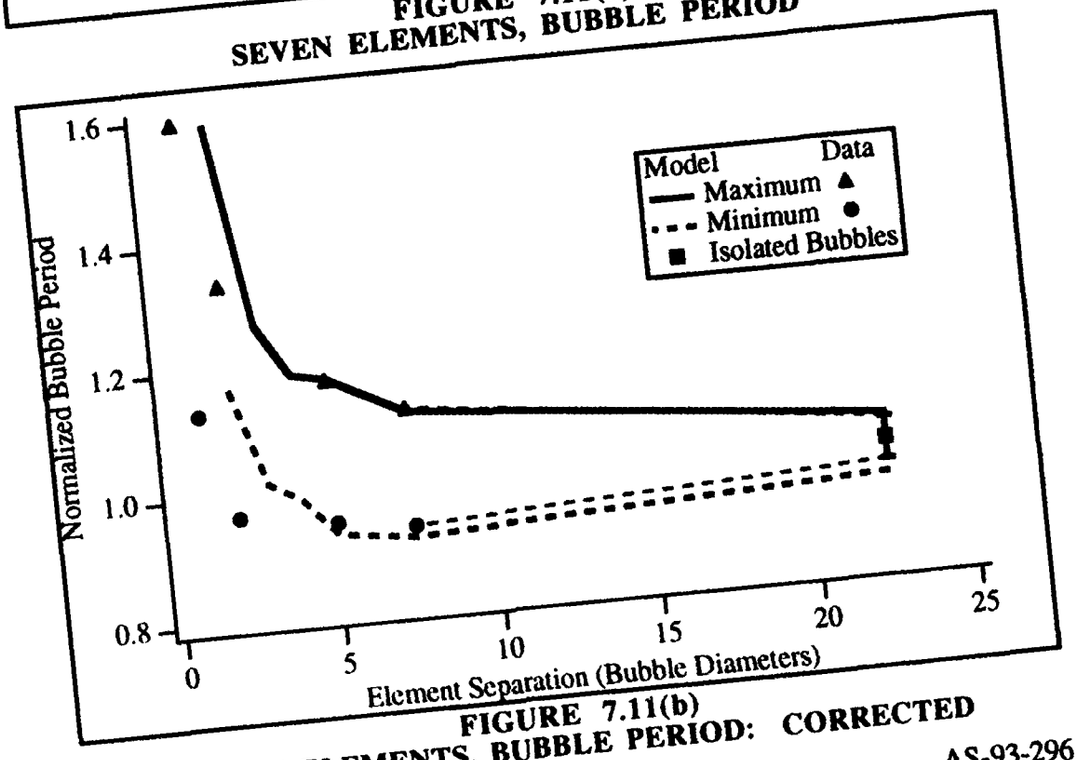

FIGURE 7.11(b)
SEVEN ELEMENTS, BUBBLE PERIOD: CORRECTED

AS-93-296

results in these sets indicated that the other elements appeared normal. It was therefore determined that the data would be analyzed with the following modifications.

Three-Element Data: If the shortest bubble period was less than one standard deviation below the overall average bubble period, that bubble period would be replaced with the average of the other two bubble periods. It was determined that about half of this data set contained such a period, and in no case did a single shot contain more than one such bubble period. This tends to support the hypothesis that the problem was intermittent and involved one element.

Seven-Element Data: In measuring the minimum bubble period, the first collapse peak was ignored, and the minimum bubble period was calculated using the second collapse peak. The maximum bubble period measurement was not affected.

The results of this modified analysis are shown in Figs. 7.9(b) and 7.11(b). It can immediately be seen that the modification of one point in the three-element graph and one point in the seven-element graph made a considerable difference in the appearance of the data.

The agreement between model and experiment is generally good, although the model predicts a larger change in the bubble period at the smallest separations. A small "glitch" appears on both the experimental and model data at a separation of about 15 bubble diameters (1.5 m) in Fig. 7.9(a) and 7.9(b). It is not currently

known why this occurs. The time delay at this separation is about 1 millisecond, and the magnitudes of the initial pressure peak and minimum pressure at the surface of a neighboring bubble are about 150 kPa and –6.0 kPa, respectively. One possible explanation is that the glitch represents the onset of interaction. The internal pressure (and therefore the liquid pressure near the bubble wall) at the maximum bubble radius in the model is about 11 or 12 kPa, and a close examination of the graph shows that the maximum bubble period is affected more than the average bubble period. The center element in an array of elements was generally observed in the model to have the longest bubble period, if the energy delivered to each of the elements was equal. Therefore, the glitch on both the model and the data maximum bubble period probably corresponds to the center element. The sum of the internal pressure of the center element and the overpressures from the two outer elements are very close to zero at this separation, and it will be discussed in Sec. 7.3 that the elements will interact in such a way as to keep the total pressure from vanishing. The weak point in this argument is that the model prediction of the internal pressure may not be valid, depending on whether the modeling of the mass flow is accurate. The internal pressure may be as low as the water vapor pressure (2 - 3 kPa, depending on the ambient temperature), as the bubble wall velocity vanishes at the maximum radius, and the bubble contents are very likely in equilibrium.[1] Alternatively, if it is assumed that the internal pressure is about 11 - 12 kPa, and that this pressure is the vapor pressure, then a value of about 320°K can be calculated from Eq. (3.63) for the temperature at the bubble wall. This is only an increase of about 20°K from the ambient temperature, and considering the remarks made previously about the possible

increase of the temperature at the bubble wall as a result of mass flow, this may be a reasonable value. The internal pressure calculated from the measured pressure signature, assuming R_{max} is given by Eq. (2.47), is about 9 kPa.

7.3 Acoustic Radiation

When several noninteracting acoustic radiators are arrayed together, the pressure signature in the farfield of the array is given by the sum of the individual pressure signatures from each of the radiators. If the other radiators do not significantly alter the medium in which a given radiator is vibrating, then the radiators do not interact, and the pressure signature of the array is given by a superposition of the pressure signatures of each of the radiators acting alone. If, however, the radiators do significantly alter the medium, then the radiators do interact, and a superposition of the individual signatures will not give the correct results for the pressure signature of the array. For example, consider again the case of two bubbles separated a distance δ (Fig. 5.1). When the bubbles are at their maximum radius, the radiated overpressure is at its minimum value. A restriction on the pressure is that the total pressure (the sum of the two overpressure signatures and the ambient pressure) must be greater than zero (a total pressure of zero here would be a perfect vacuum). This restriction implies an inequality for the distances:

$$p_\infty + \frac{r_1}{r_1}\left[p_B - p_\infty\right] + \frac{r_1}{r_2 - r_1}\left[p_B - p_\infty\right] > 0 \quad \Rightarrow \quad r_2 > r_1 \frac{p_\infty}{p_B} \quad . \tag{7.3}$$

In this equation, r_1 and r_2 are the distances from the centers of the two bubbles. The total pressure reaches its minimum value at the surfaces of the two bubbles. If r_1 is set to R_{max}, then

$$r_2 > R_{max} \frac{p_\infty}{p_B} \quad . \tag{7.4}$$

The values for the experiments performed in this study are the following:

$$p_B = 9\,\text{kPa} \;@\; R = R_{max} \tag{7.5}$$

$$p_\infty = 207\ \text{kPa} \qquad R_{max} = 0.044\ \text{m} \quad . \tag{7.6}$$

When these values are substituted into Eq. (7.4), a minimum value of about 1 meter is found for r_1. The implication of this finding is that in this experiment the two elements must interact (and the acoustic signature must be modified) when the elements are spaced less than 1 meter apart. This distance corresponds to about 10 bubble diameters under the conditions of this experiment, which is approximately the separation at which the model began to predict some interaction.

To gain insight into this element interaction, the acoustic radiation can be characterized by examining the peak of the power spectrum. The power spectrum is a function of frequency obtained by squaring the magnitude of the Fourier transform of the acoustic signature measured in the farfield. The integral of the power spectrum gives the total radiated acoustic energy, in a manner similar to that noted in Chap. 1. If the radiation is not spherically symmetric (as happens with an array of multiple elements), then the power spectrum is also a function of angle with respect to the array orientation. To keep the analysis simple, the power spectrum will be considered at a fixed measurement location. This analysis will

provide sufficient insight into the radiation characteristics, and the angle dependence of the power spectrum can be neglected in this case.

The power spectrum was calculated for each of the measured broadside hydrophone signatures. The broadside hydrophone was placed in the same location for all the data recorded. The power spectrum for the experimentally measured single-element signatures in Fig. 4.10 is shown in Fig. 7.12, and the spectrum for the model signature in Fig. 4.10 is overlaid. The shape of these spectra is typical for the acoustic signatures from single spark-generated bubbles over wide ranges of energy and depth. The frequency of the peak in the spectrum corresponds roughly to the bubble period, as was mentioned in Chap. 2 ($f_{peak} \approx \tau^{-1}$). The model spectrum shown is similar to the experimental spectrum, although the peak of the model spectrum is about 40% higher. For comparison, the power spectrum of a multiple element shot (the acoustic data of Fig. 7.4) is shown in Fig. 7.13, with the corresponding model power spectrum (from the shot in Fig. 7.8) overlaid. The agreement between these two spectra is very good at the lower frequencies. The structure in the higher frequencies varies, depending on the relative timing of the discharge initiations, and the structure shown in these two spectra is typical. The peaks of the power spectra of multiple element signatures can be characterized by normalizing the peak values to the peak value of the spectrum of the single elements. Power spectra of one, three, five, and seven elements at separations of 0.19, 0.48, and 0.71 m were examined. The normalized power spectrum peak values are shown in Fig. 7.14. The solid line on the graph noted as superposition is the predicted normalized power spectrum peak using linear superposition (simply the number of elements squared, since the pressure is proportional to the number of

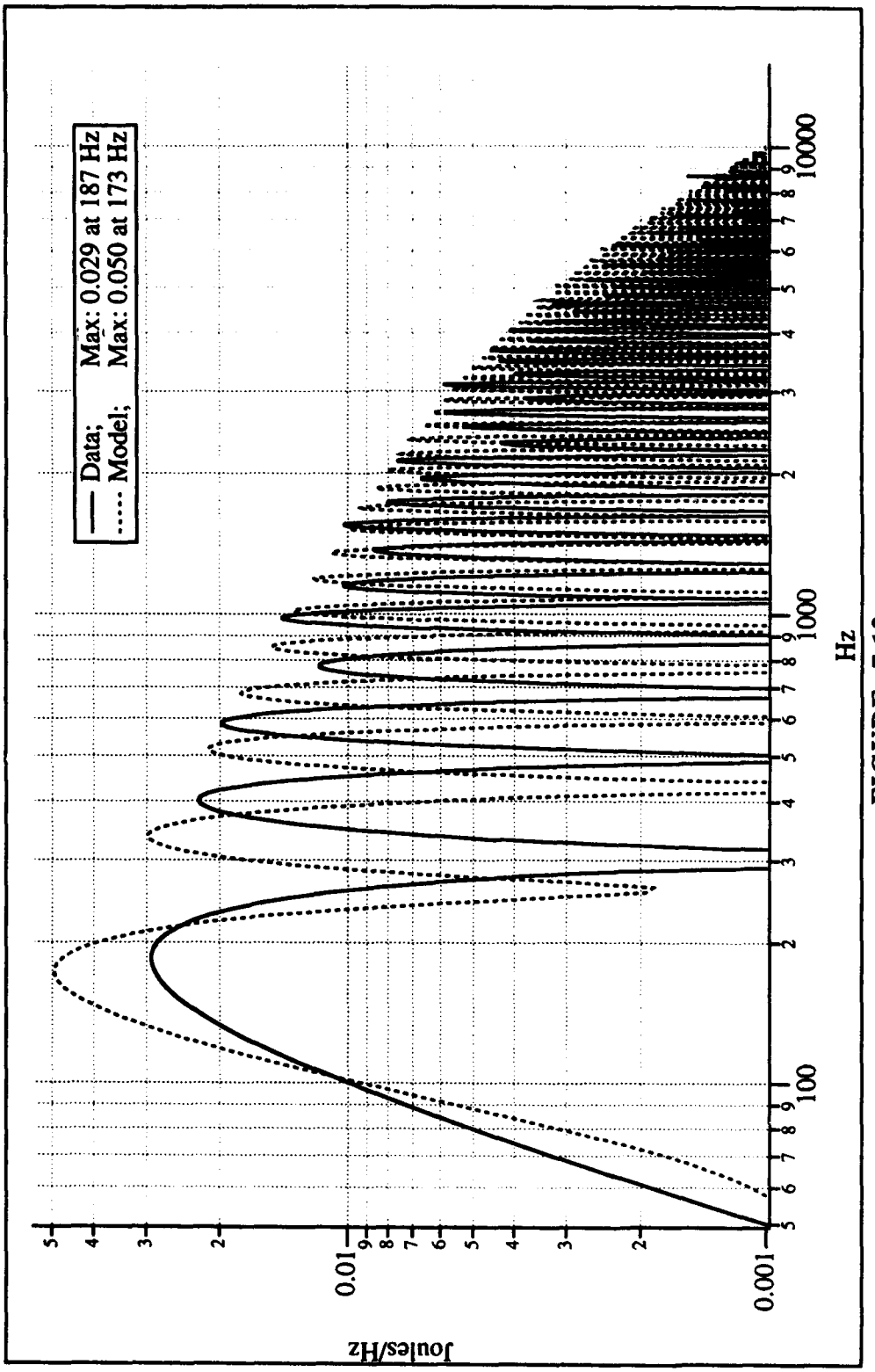

FIGURE 7.12
ACOUSTIC POWER SPECTRUM: ONE ELEMENT

AS-93-297

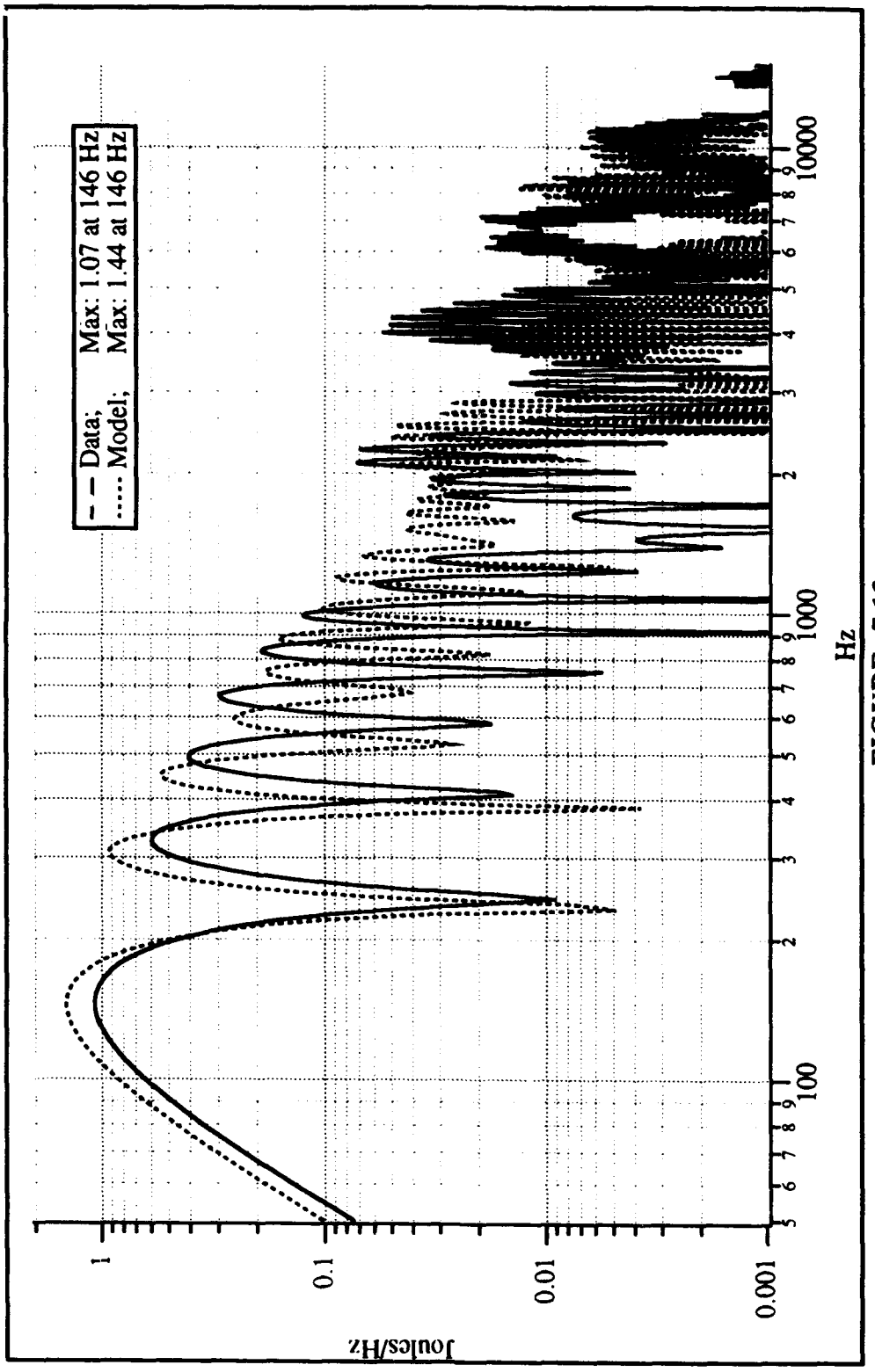

FIGURE 7.13
ACOUSTIC POWER SPECTRUM: SEVEN ELEMENTS at 0.48 m

AS-93-298

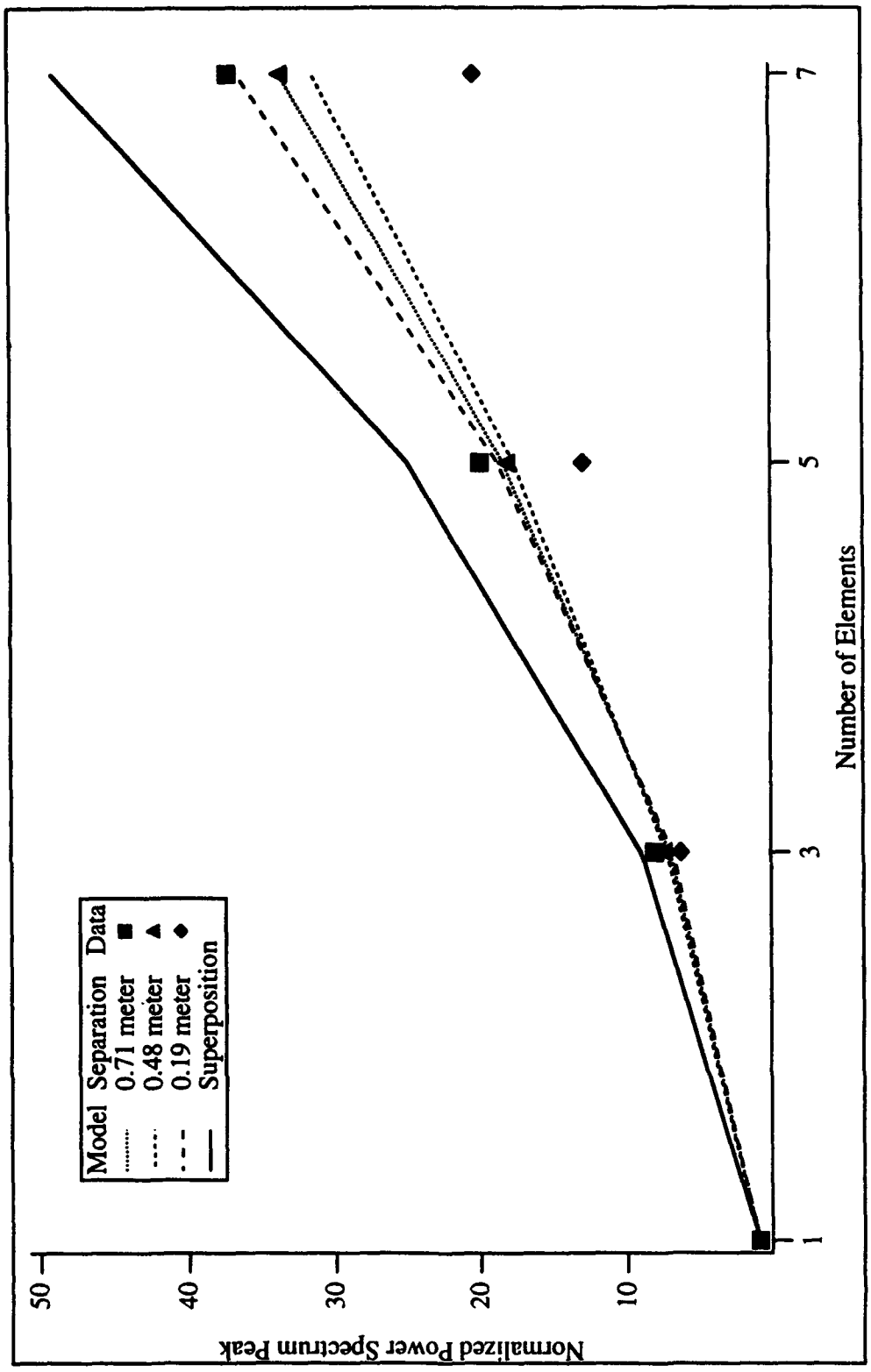

FIGURE 7.14
NORMALIZED POWER SPECTRUM PEAK VALUES

AS-93-299

elements). The interaction serves to reduce the peak of the power spectrum, and at the two wider separations the model predicts an effect larger than the effect observed, as it did for the bubble period. Although the model describes the interaction effects on the power spectrum at separations of 0.48 m and 0.71 m, it does not describe the effects at 0.19 m. Note that the dashed line for the 0.19 meter separation does not go with the upper two points, but with the lower two points, and the model predicts an increase in the power spectrum peak, as opposed to the data, which shows a sharp drop at this separation.

---

[1]M. S. Plesset and A. Prosperetti, "Bubble Dynamics and Cavitation," *Ann. Rev. Fluid Mech.* **9**, 145–185 (1977).

8. CONCLUSIONS

The model developed in Chap. 3 described several important characteristics of isolated spark-generated bubbles. The parameters determined using the methods outlined in Sec. 4.1 allowed the model to predict the time evolution of the bubbles from a given class of similar discharges. The model did not, however, capture all the subtleties of the internal dynamics, because it did not correctly calculate the acoustic signatures from the discharges with longer discharge times, despite picking up the shift in hydraulic efficiency with depth. Part of the problem may lie in the use of the parameterized discharges. The use of sampled data for all the discharges may have resulted in a better match. Further study is needed to determine how crucial the exact discharge characteristics are for the model. The predictions by the model of the other characteristics of the acoustic signature indicated that the model equations were a reasonable approximation to the gross features of the internal dynamics, and the model was useful in calculating these characteristics from a given discharge. Unfortunately, the ability of the model to significantly enhance the bubble period information available from Eq. (2.51) is somewhat questionable, because the scaling of the bubble period with energy is given very closely by that equation.

The interaction model developed in Chap. 5 provided information regarding the dynamics of multiple spark-generated bubbles. The acoustic signatures shown in Chap. 7 show a strong similarity between the measured signatures and modeled signatures. The graphs of the bubble period versus the separation of the spark elements show reasonable agreement between the measured and modeled data for each of the cases considered. The agreement is especially good for the three-element data. The five- and seven-element data also showed reasonable agreement, but had lower resolution than the three-element data. The shape of the modeled power spectrum for a single element was similar to the shape of the measured power spectrum, but the peak value was somewhat higher. The comparison of the two multiple element spectra indicated that the spectra were very similar at the lower frequencies, with variations due to the randomness in the discharges starting at around 1.5 kHz, or about ten times the fundamental frequency.

The minimum interaction distance for two bubbles was found in Eq. (7.4) to scale as the maximum bubble radius. The actual distance at which the interaction becomes noticeable may be somewhat larger, but will certainly be no smaller than the distance given. If more than two elements are present, the distance calculated as the minimum interaction distance will be larger. For the seven-element array, a minimum interaction distance is calculated in a procedure similar to the one given above to be about 35 bubble diameters. In any case, the interaction manifests itself in the addition of the pressure signatures differing from superposition well before the changes in the bubble period become noticeable. According to Eq. (2.55), typical linear arrays may have separation distances on the order of 10 - 50 bubble diameters depending on the depth and desired directivity of the beam. For such an

array, the interaction effect on the peak of the power spectrum will probably be much more important than the effect on the bubble period.

A limited number of simulations were carried out with nine elements in a 3 x 3 two-dimensional array. However, these results are not presented in this report and no experimental investigations were done. Indications were that the conclusions reached in the one-dimensional case were probably also valid in the two-dimensional case, except that the effects are sufficiently larger that the shift in the bubble period may start to have a non-negligible effect for separations that would be used in such an array.

APPENDIX A: MODEL EQUATIONS

The following equations are integrated simultaneously:

$$\left(1-\frac{\dot{R}}{c_\infty}\right)R\ddot{R}+\frac{3}{2}\left(1-\frac{\dot{R}}{3c_\infty}\right)\dot{R}^2=\left(1+\frac{\dot{R}}{c_\infty}\right)\left(h_B-\frac{p_v(\vec{x}_i,t)}{\rho_\infty}\right)+\frac{R}{c_\infty}\dot{h}_B \tag{3.27}$$

$$\eta=\left(1-\frac{P}{g}\frac{\partial g}{\partial \alpha}\left(\frac{\partial \alpha}{\partial P}\right)_T\right)^{-1} \tag{3.81}$$

$$\dot{T}=\frac{3g\Re T}{c_v PR}\left[q-\dot{R}\left(\left(\frac{\partial U}{\partial V}\right)_{T,M}+P\right)\right] \tag{3.91}$$

$$\dot{P}=\eta P\left[\left(\frac{\partial g}{\partial \alpha}\frac{1}{g}\left(\frac{\partial \alpha}{\partial T}\right)_p+\frac{1}{T}\right)\dot{T}+\frac{3g\Re T}{PR}\dot{m}_T-\frac{3\dot{R}}{R}\right] \quad . \tag{3.92}$$

The terms in Eq. (3.27) are described in Sec. 3.1, and the differentials in Eqs. (3.81), (3.91), and (3.92) are given in Eqs. (3.93) through (3.103). The terms pertaining to heat flow (q) and mass flow ($\dot{m}_T$) in Eq. (3.91) and (3.92) are given in Sec. 3.3. The variable pressure in Eq. (3.27) describes the interaction between elements, and is given by:

$$p_v(\vec{x}_i,t)=\sum_{\substack{j=1\\ j\neq i}}^{N}\left[p_j(r_{ij},t_r)-p_\infty\right] \tag{5.2}$$

$$t_r\equiv t-r_{ij}/c_\infty \quad . \tag{5.3}$$

The terms not identified explicitly in the Appendix or in the text can be found in the Glossary.

APPENDIX B: SECOND ORDER EQUATION OF DYNAMICS

The second order equation of bubble dynamics from Lezzi and Prosperetti was given in Chap. 3 as

$$\left(\frac{R}{c_\infty}\ddot{R}\right)^2+\left[1-\frac{3}{2}\frac{\dot{R}}{c_\infty}\left(1-\frac{38}{15}\frac{\dot{R}}{c_\infty}\right)\right]R\ddot{R}+\frac{3}{2}\left[1-\frac{5}{6}\frac{\dot{R}}{c_\infty}\left(1-\frac{52}{25}\frac{\dot{R}}{c_\infty}\right)\right]\dot{R}^2= \tag{3.110}$$
$$\left(1+\frac{\dot{R}}{2c_\infty}\right)\left[h_B-\frac{p_v(t)}{\rho_\infty}\right]+\frac{\dot{R}}{c_\infty}\left(1-\frac{3}{2}\frac{\dot{R}}{c_\infty}\right)\frac{d}{dt}\left[h_B-\frac{p_v(t)}{\rho_\infty}\right]$$
$$+\frac{1}{c_\infty^2}\frac{d}{dt}\left[g_2-R^2\frac{d}{dt}\frac{p_v(t)}{\rho_\infty}\right] \quad .$$

One of the most troublesome terms in the above equation is the following:

$$g_2=-\int_0^{t_*}\Gamma(t_*-\tau,\tau)\,d\tau \quad . \tag{B.1}$$

This term is the incident pressure term comparable to the function $g''(t)$ in the first order equation. Γ is a combination of the incident pressures and integrals of the incident pressures, resulting from the matching conditions for the solutions in the perturbation expansion. The variables t_* and τ are dimensionless times, t_* representing the present time in the integration of the equation for the bubble dynamics, and τ representing the dummy variable in the integral for g_2. The function g_2 is the integral at each time step from some initial time up to the present time in the integration of the equation for the bubble dynamics, and is, therefore, a function of the history of the incoming pressure disturbances. This added

complication makes calculation of $\ddot{R}$ with the second order equation very difficult for physical situations with incoming pressure disturbances. The second order equation is best suited to modeling an isolated spherical bubble, and will not be used for the multiple bubble studies.

This rather complicated second-order equation can be simplified somewhat. If it is assumed that no pressure disturbances propagate towards the bubble,

$$\Gamma = 0 \quad \Rightarrow \quad g_2 = 0 \tag{B.2}$$

$$p_v(t) = 0 \quad . \tag{B.3}$$

Setting $g_2 = 0$ and $p_v(t) = 0$, the equation for the bubble dynamics becomes:

$$\left(\frac{R}{c_\infty}\ddot{R}\right)^2 + \left[1 - \frac{3}{2}\frac{\dot{R}}{c_\infty}\left(1 - \frac{38}{15}\frac{\dot{R}}{c_\infty}\right)\right]R\ddot{R} + \frac{3}{2}\left[1 - \frac{5}{6}\frac{\dot{R}}{c_\infty}\left(1 - \frac{52}{25}\frac{\dot{R}}{c_\infty}\right)\right]\dot{R}^2 = \left(1 + \frac{1}{2}\frac{\dot{R}}{c_\infty}\right)h_B + \frac{R}{c_\infty}\left(1 - \frac{3}{2}\frac{\dot{R}}{c_\infty}\right)\dot{h}_B \quad . \tag{B.4}$$

The equation for the bubble dynamics is quadratic in the bubble wall acceleration, and it must be solved for $\ddot{R}$. The following may be defined:

$$m = \frac{\dot{R}}{c_\infty} \tag{B.5}$$

$$S = \frac{\dot{h}_B \rho_\infty}{\dot{p}_B} = \frac{\rho_\infty}{p_B + B}\left[\frac{n-1}{n}h_B + \frac{p_\infty + B}{\rho_\infty}\right] \tag{B.6}$$

$$Z_0 = \rho_\infty c_\infty \tag{B.7}$$

$$D = \frac{1}{Z_0}\left(\frac{R\dot{P}}{c_\infty^2} + \frac{m}{R}\left(\frac{2\sigma}{c_\infty} + 4\mu m\right)\right) \tag{B.8}$$

$$J_2 = 1 - \frac{3}{2}m\left(1 - \frac{38}{15}m\right) + \frac{4\mu S}{RZ_0}\left(1 - \frac{3}{2}m\right) \quad . \tag{B.9}$$

Then if the equation of bubble dynamics is written in the standard form for a quadratic equation ($A\ddot{R}^2 + B\ddot{R} + C = 0$),

$$\ddot{R} = \frac{B}{2A}\left(-1 \pm \sqrt{1 - 4\frac{AC}{B^2}}\right) \qquad A_2 = \frac{R^2}{c_\infty^2} \qquad B_2 = J_2 R \qquad \text{(B.10)}$$

$$C_2 = \frac{3}{2}\left[1 - \frac{5m}{6}\left(1 - \frac{52m}{25}\right)\right]m^2 c_\infty^2 - \left(1 + \frac{m}{2}\right)h_B - SD\left(1 - \frac{3m}{2}\right)c_\infty^2 \quad .$$

Before the complete equation for $\ddot{R}$ is written, it would be useful to determine which sign is proper in front of the square root. To check whether the + or – sign is correct, the equation should be examined near equilibrium conditions. That is to say, $\ddot{R}$ can be examined when the mach number vanishes, and $\left(h_B + RS\dot{P}/Z_o\right)/c_\infty^2 \to 0$:

$$A = \frac{R^2}{c_\infty^2} \qquad B \approx R\left(1 + \frac{4\mu S}{RZ_0}\right) \qquad C \approx -c_\infty^2\left(\frac{h_B + RS\dot{P}/Z_o}{c_\infty^2}\right) \quad . \qquad \text{(B.11)}$$

Now, these terms can be substituted into the appropriate equations, and assuming $\mu = 0$,

$$\ddot{R} \approx \frac{c_\infty^2}{2R}\left(-1 \pm \sqrt{1 + 4\left(\frac{h_B + RS\dot{P}/Z_o}{c_\infty^2}\right)}\right) \quad . \qquad \text{(B.12)}$$

The demand that $\ddot{R} \to 0$ as $\left(h_B + RS\dot{P}/Z_o\right)/c_\infty^2 \to 0$ indicates that the + sign is correct. The full second order equation for $\ddot{R}$ is then given by

$$\ddot{R} = \frac{c_\infty^2 J_2}{2R}\left[\sqrt{1 - \frac{4C_2}{J_2^2 c_\infty^2}} - 1\right] \quad . \qquad \text{(B.13)}$$

GLOSSARY

Symbols

α	Degree of Dissociation
α_i	Attenuation Coefficient
α_M	Accommodation Coefficient
β	O(1) Equation Indeterminacy
χ_i	Avg. Var. Pressure Correction
δ	Bubble Separation
ε	Emissivity/Absorptivity
ε_0	Acoustic Mach Number
ε_{hyd}	Hydraulic Efficiency
Γ	Mass Flow Correction Factor
γ	Ratio of Specific Heats
η	Intermediate Function
η_{init}	Discharge Energy Proportion
Φ	Incident Velocity Potential
φ	Velocity Potential
λ	Wavelength
μ	Viscosity
ν	Frequency
Π	Radiation Dissipated
ρ	Liquid Density
σ	Surface Tension
σ_{BB}	Stefan-Boltzmann Constant
τ	Bubble Period
Ω	Specific Delivered Power
ζ	Heat Flow Factor
A	Discharge Fitting Parameter
B,n	Liquid Eq. of State Constants
C	Mean Free Path Constant
c	Sound Speed
c_p	Const. Pressure Specific Heat
c_v	Const. Volume Specific Heat
c_{v_dis}	Const. Vol. Sp. Heat, Dis.
$c_{v\_H_2O}$	Const. Vol. Sp. Heat, Vapor
D	Bubble Diameter
E	Energy

f	Wave Function
f_{BB}	Specific Blackbody Radiation
F_{BB}	Total Blackbody Radiation
g	Wave Function
$g(\alpha)$	Number of Particles/Molecule
h	Liquid Enthalpy
I	Ionization Energy
k	Wave Number
k_B	Boltzmann Constant
ℓ	Photon Mean Free Path
L	Latent Vaporization Heat
L_{dis}	Latent Dissociation Heat
M	Mass
$\dot{m}$	Specific Mass Flow
m_w	Water Molecule Mass
N	Number of Bubbles
P	Internal Pressure
P_0	Discharge Power Amplitude
p	Pressure
p^*	Equilibrium Vapor Pressure
p_0	Evap. Temperature Constant
q	Specific Heat Flow
Q	Total Heat Flow
R	Bubble Radius
$\dot{R}$	Bubble Wall Velocity
$\ddot{R}$	Bubble Wall Acceleration
r	Radial Coordinate
$r.h.s.$	Right Hand Side
r_{ij}	Distance Between Bubbles
$\Re$	Ideal Gas Constant
T	Internal Temperature
T_{KE}	Kinetic Energy
t	Time
t_*	Non-Dim. Discharge Time
U	Gas Energy
u	Particle Velocity
V	Volume
$\dot{V}$	Volume Velocity
$\ddot{V}$	Volume Acceleration
W	Work
x	Dissipation Length
$\vec{x}$	Position Vector
$\mathbf{z}$	Specific Acoustic Impedance

Subscripts

∞	Undisturbed
a	Antisymmetric
B	Bubble Wall

BB	Blackbody	p	Constant Pressure
dis	Dissociated	R	Rosseland
E	Evaporation/Condensation	r	Retarded
init	Initial Conditions	s	Symmetric
i,j	Bubble Indices	T	Total
M	Massflow	v	Variable Part
max	Maximum Value	w	Water
min	Minimum Value		

BIBLIOGRAPHY

A Physicist's Desk Reference, edited by H. L. Anderson (American Institute of Physics, New York, 1989), 2nd ed. of *Physics Vade Mecum*, pp. 267–268.

Beckmann, W. C., A. C. Roberts, and B. Luskin, "Sub-Bottom Depth Recorder," *Geophysics* **24**(4), 749–760 (1959).

Bjørnø, L., "A Comparison Between Measured Pressure Waves in Water Arising From Electrical Discharges and Detonation of Small Amounts of Chemical Explosives," *Trans. ASME, J. Eng. Ind.*, Paper No. 69–Unt-1, 1–8 (1969).

Bornhorst, W. J., and G. N. Hatsopoulos, "Analysis of a Liquid Vapor Phase Change by the Methods of Irreversible Thermodynamics," *J. Appl. Mech.* **34**, 840–846 (1967).

Bornhorst, W. J., and G. N. Hatsopoulos, "Bubble-Growth Calculation Without Neglect of Interfacial Discontinuities," *J. Appl. Mech.* **34**, 847–853 (1967).

Caulfield, D. D., "Predicting Sonic Pulse Shapes of Underwater Spark Discharges," *Deep-Sea Research* **9**, 339–348 (1962).

Cole, R. H., *Underwater Explosions* (Princeton University Press, Princeton, New Jersey, 1948).

Cook, J. A., "Studies of Various Electrode Configurations for a Plasma Sound Source," *J. Acoust. Soc. Am. Suppl. 1* **88**, S168 (1990).

Cook, J. A., "Mutual Coupling Effects Between Elements in a Spark Source Array," *J. Acoust. Soc. Am.* **90**(4), Pt. 2, 2350 (1991).

Edelmann, H., "An Underwater Sound Source with Higher Seismic Efficiency," *Geophysical Prospecting* **16**, 474–490 (1968).

Epstein, D., and J. B. Keller, "Expansion and Contraction of Planar, Cylindrical, and Spherical Underwater Gas Bubbles," *J. Acoust. Soc. Am.* **52**(3), Pt. 2, 975–980 (1972).

Flynn, H. G., "Cavitation Dynamics. 1. A Mathematical Formulation," *J. Acoust. Soc. Am.* **57**(6), Pt. 1, 1379–1396 (1975).

Fujikawa, S., and T. Akamatsu, "Effects of the Non-Equilibrium Condensation of Vapour on the Pressure Wave Produced by the Collapse of a Bubble in a Liquid," *J. Fluid Mech.* **97**(3), 481–512 (1980).

Gardner, S., *Electro-Acoustic Properties of the Underwater Spark Discharge* (Edo Corporation, College Point, New York, 1961), Report 5480.

Gibson, D. C., "The Kinetic and Thermal Expansion of Vapor Bubbles," *Trans. ASME, J. Basic Eng.* **94**(1), 89–96 (1972).

Gibson, D. C., "The Pulsation Time of Spark Induced Vapor Bubbles," *Trans. ASME, J. Basic Eng.* **94**, 248–249 (1972).

Gilmore, F. R., *The Growth or Collapse of a Spherical Bubble in a Viscous Compressible Liquid* (California Institute of Technology Hydrodynamics Laboratory, Pasadena, California, 1952), Report 26–4.

Guman, W. J., "Study of an Inverse–Pinch Electric Discharge Sound Source," *J. Underwater Acoust.* **17**(3), 511–521 (1967).

Hentschel, W., and W. Lauterborn, "Acoustic Emission of Single Laser-Produced Cavitation Bubbles and their Dynamics," *Appl. Sci. Res.* **38**, 225–230 (1982).

Herring, C., *Theory of the Pulsations of the Gas Bubble Produced by an Underwater Explosion* (Columbia University, New London, Connecticut, 1941), NDRC Report No. C4–sr20–010.

Ioffe, A. I., "Theory of the Initial Stage of an Electrical Discharge in Water," *J. Appl. Mech. Tech. Phys. (PMTF)* **7**(6), 69–72 (1966).

Ioffe, A. I., and K. A. Naugol'nykh, "Formation of Shock Waves by an Electric Discharge in Water," *J. Appl. Mech. Tech. Phys. (PMTF)* **9**(1), 134–137 (1968).

Jackson, J. D., *Classical Electrodynamics* (John Wiley and Sons, New York, 1975), 2nd ed., pp. 290–292.

Johnston, R. C., "Development of More Efficient Airgun Arrays: Theory and Experiment," *Geophysical Prospecting* **30**, 752–773 (1982).

Keller, J. B., and I. I. Kolodner, "Damping of Underwater Explosion Bubble Oscillations," *J. Appl. Phys.* **27**(10), 1152–1161 (1956).

Keller, J. B., and M. Miksis, "Bubble Oscillations of Large Amplitude," *J. Acoust. Soc. Am.* **68**(2), 628–633 (1980).

Kelly, D. C., *Thermodynamics and Statistical Physics* (Academic Press, New York, 1973).

Khoroshev, G. A., "Collapse of Vapor-Air Cavitation Bubbles," *Akust. Zh.* **9**(3) 340–346 (1963) [English transl.: *Sov. Phys. Acoust.* **9**(3), 275–279 (1964)].

Kinsler, L. E., A. R. Frey, A. B. Coppens, and J. V. Sanders, *Fundamentals of Acoustics* (John Wiley and Sons, New York, 1982), 3rd ed.

Kirkwood, J. G., and H. A. Bethe, *The Pressure Wave Produced by an Underwater Explosion* (Office of Science Research and Development, 1942), Report 588.

Lastman, G. J., and R. A. Wentzell, "Comparison of Five Models of Spherical Bubble Response in an Inviscid Compressible Liquid," *J. Acoust. Soc. Am.* **69**(3), 638–642 (1981).

Lezzi, A., and A. Prosperetti, "Bubble Dynamics in a Compressible Liquid. Part 2. Second-order Theory," *J. Fluid Mech.* **185**, 289–321 (1987).

Martin, E. A., *The Underwater Spark: An Example of Gaseous Conduction at About 10,000 Atmospheres*, Ph.D. Dissertation (University of Michigan, Ann Arbor, 1956).

Martin, E. A., "Experimental Investigation of a High-Energy Density, High-Pressure Arc Plasma," *J. Appl. Phys.* **31**(2), 255–267 (1960).

Mellen, R. H., *An Experimental Study of the Collapse of a Spherical Cavity in Water* (U. S. Navy Underwater Sound Laboratory, New London, Connecticut, 1955), Research Report 279.

Mitchell, T., and F. G. Hammitt, "On the Effects of Heat Transfer upon Collapsing Bubbles," *Nuc. Sci. Eng.* **53**, 263–276 (1974).

Morse, P. M., *Vibration and Sound* (Acoustical Society of America, American Institute of Physics, New York, 1981), 2nd ed., Chap.7, pp. 311–325.

Naugol'nykh, K. A., "Electrical and Hydrodynamical Characteristics of an Impulsive Corona in Water," *Akust. Zh.* **13**(3), 417–426 (1967) [English transl.: *Sov. Phys. Acoust.* **13**(3), 352–359 (1968)].

Naugol'nykh, K. A., and N. A. Roi, *ELEKTRICHESKIE RAZRJADY V VODE* (Nauka, Moskva, 1971) [English transl.: *Spark Discharges in Water* (Applied Research Laboratories, The University of Texas at Austin, 1987), Internal Report].

Neppiras, E. A., and B. E. Noltingk, "Cavitation Produced by Ultrasonics: Theoretical Conditions for the Onset of Cavitation," *Proc. Phys. Soc. B (London)* **64B**, 1032–1038 (1951).

Neppiras, E. A., "Acoustic Cavitation," *Physics Reports* **61**(3), 159–251 (1980).

Noltingk, B. E., and E. A. Neppiras, "Cavitation Produced by Ultrasonics," *Proc. Phys. Soc. B (London)* **63B**, 674–683 (1950).

Nooteboom, J. J., "Signature and Amplitude of Linear Airgun Arrays," *Geophysical Prospecting* **26**, 194–201 (1978).

Okun', I. Z., "Generation of Compression Waves by a Pulsed Discharge in Water," *Zh. Tekh. Fiz.* **41**(2), 292–301 (1971) [English transl.: *Sov. Phys. Tech. Phys.* **16**(2), 219–226 (1971)].

Plesset, M. S., and A. Prosperetti, "Bubble Dynamics and Cavitation," *Ann. Rev. Fluid Mech.* **9**, 145–185 (1977).

Press, W. H., B. P. Flannery, S. A. Teukolsky, and W. T. Vetterling, *Numerical Recipes in Pascal* (Cambridge University Press, Cambridge, 1989), Chap. 15, pp. 599–632.

Prosperetti, A., and A. Lezzi, "Bubble Dynamics in a Compressible Liquid. Part 1. First-order Theory," *J. Fluid Mech.* **168**, 457–478 (1986).

Prosperetti, A., "Bubble Phenomena in Sound Fields: Part One," *Ultrasonics* **22**, 69–77 (1984).

Rayleigh, Lord, "On the Pressure Developed in a Liquid During the Collapse of a Spherical Cavity," *Phil. Mag.* **34**, 94–98 (1917).

Roberts, R. M., *The Energy Partition of Underwater Sparks*, Ph.D. Dissertation (The University of Texas at Austin, to be published).

Robinson, J. W., M. Ham, and A. N. Balaster, "Ultraviolet Radiation from Electrical Discharges in Water," *J. Appl. Phys.* **44**(1), 72–75 (1973).

Rogers, R. L., *Intermediate Energy Tests and Analysis of a Plasma Sound Source* (Applied Research Laboratories, The University of Texas at Austin, 1992), Report ARL–TR–92–15.

Ryabinin, A. G., and G. A. Ryabinin, "Gas-Bubble Energy in an Underwater Electrical Discharge," *Zh. Tekh. Fiz.* **46**, 881–884 (1976) [English transl.: *Sov. Phys. Tech. Phys.* **21**(4), 512–514 (1976)].

Safar, M. H., "The Radiation of Acoustic Waves from an Air-Gun," *Geophysical Prospecting* **24**, 756–772 (1976).

Schrage, R. W., *A Theoretical Study of Interphase Mass Transfer* (Columbia University Press, New York, 1953).

Shamko, V. V., "Integrated Bulk Characteristics of the Plasma in an Underwater Spark," *Zh. Tekh. Fiz.* **48**, 967–971 (1978) [English transl.: *Sov. Phys. Tech. Phys.* **23**(5), 564–567 (1978)].

Shima, A., and Y. Tomita, "Some Numerical Aspects of Cavitation Bubble Collapse," in *Ann. Rev. of Num. Fluid Mech. Heat Transfer*, edited by L. A. Dziobek and B. Brienza (Hemisphere Publishing Corporation, 1989), Vol. 2, Chap. 5, pp. 198–226.

Shima, A., and Y. Tomita, "Impulsive Generation by Bubble/Pressure-Wave Interaction," *AIAA Journal* **26**(4), 434–437 (1988).

Sinclair, J. E., and G. Bhattacharya, "Interaction Effects in Marine Seismic Source Arrays," *Geophysical Prospecting* **28**, 323–332 (1980).

Tomita, Y., and A. Shima, "On the Behavior of a Spherical Bubble and the Impulse Pressure in a Viscous Compressible Liquid," *Bull. JSME* **20**, 1453–1460 (1977).

Trilling, L., "The Collapse and Rebound of a Gas Bubble," *J. Appl. Phys.* **23**(1), 14–17 (1952).

Young, F. R., *Cavitation* (McGraw-Hill Book Company, London, 1989), Chap. 2, pp. 8–37.

Zel'dovich, Y. B., and Y. P. Raizer, *Physics of Shock Waves and High–Temperature Hydrodynamic Phenomena*, edited by W. D. Hayes and R. F. Probstein (Academic Press, New York, 1966), Vol. I, Chap. 6, pp. 269–276.

Ziolkowski, A., G. Parkes, L. Hatton, and T. Haugland, "The Signature of an Air Gun Array: Computation from Near-Field Measurements Including Interactions," *Geophysics* **47**(10), 1413–1421 (1982).

This page intentionally left blank.

1 June 1993

Distribution List for
ARL-TR-93-10
Technical Report under Grants N00014-91-J-1366 and N00014-93-J-0018

Copy No.	
1-2	DR LOGAN E HARGROVE OFFICE OF NAVAL RESEARCH PHYSICS DIVISION ONR 312 DEPARTMENT OF THE NAVY ARLINGTON VA 22217-5660
3	M BADIEY ONR 1125 OA OFFICE OF NAVAL RESEARCH DEPARTMENT OF THE NAVY ARLINGTON VA 22217-5660
4	OFFICE OF NAVAL RESEARCH TECHNICAL LIBRARY DEPARTMENT OF THE NAVY ARLINGTON VA 22217-5660
5-6	ADMINISTRATIVE GRANTS OFFICER OFFICE OF NAVAL RESEARCH RESIDENT REPRESENTATIVE N66009 ADMINISTRATIVE CONTRACTING OFFICER ROOM 582 FEDERAL BUILDING 300 EAST 8TH STREET AUSTIN TX 78701-3273
7	NAVAL RESEARCH LABORATORY TECHNICAL LIBRARY CODE 5226 WASHINGTON DC 20375-5320
8	NAVAL RESEARCH LABORATORY TECHNICAL LIBRARY STENNIS SPACE CENTER MS 39529-5004
9	NAVAL OCEANOGRAPHIC OFFICE TECHNICAL LIBRARY STENNIS SPACE CENTER MS 39522-5001
10	L FABIAN PMW 182-3 SPACE AND NAVAL WARFARE SYSTEMS COMMAND DEPARTMENT OF THE NAVY WASHINGTON ~C 20363-5100
11	SPACE AND NAVAL WARFARE SYSTEMS COMMAND TECHNICAL LIBRARY DEPARTMENT OF THE NAVY WASHINGTON DC 20363-5100

Distribution List for ARL-TR-93-10 under Grants N00014-91-J-1366 and N00014-93-J-0018
(cont'd)

Copy No.	
12	D EDELBLUTE CODE 712 NAVAL COMMAND CONTROL AND OCEAN SURVEILLANCE CENTER RDT&E DIVISION SAN DIEGO CA 92152-5000
13	NAVAL COMMAND CONTROL AND OCEAN SURVEILLANCE CENTER RDT&E DIVISION TECHNICAL LIBRARY SAN DIEGO CA 92152-5000
14	NAVAL COMMAND CONTROL AND OCEAN SURVEILLANCE CENTER RDT&E DIVISION DETACHMENT TECHNICAL LIBRARY P O BOX 997 KAILUA HI 96734-0997
15	NAVAL SURFACE WARFARE CENTER DAHLGREN DIVISION TECHNICAL LIBRARY DAHLGREN VA 22448
16	NAVAL SURFACE WARFARE CENTER COASTAL SYSTEMS STATION DAHLGREN DIVISION TECHNICAL LIBRARY PANAMA CITY FL 32407-5000
17	NAVAL SURFACE WARFARE CENTER CARDEROCK DIVISION TECHNICAL LIBRARY BETHESDA MD 20084-5000
18	NAVAL UNDERSEA WARFARE CENTER DIVISION TECHNICAL LIBRARY NEW LONDON CT 06320-5594
19-20	DEFENSE TECHNICAL INFORMATION CENTER BUILDING 5 CAMERON STATION ALEXANDRIA VA 22314
21	ADVANCED RESEARCH PROJECTS AGENCY TECHNICAL LIBRARY 3701 NORTH FAIRFAX DRIVE ARLINGTON VA 22203-1714

Distribution List for ARL-TR-93-10 under Grants N00014-91-J-1366 and N00014-93-J-0018 (cont'd)

Copy No.	
	DEFENSE MAPPING AGENCY HYDROGRAPHIC/TOPOGRAPHIC CENTER
22	TECHNICAL LIBRARY WASHINGTON DC 20315-0030
	NATIONAL ACADEMY OF SCIENCES NATIONAL RESEARCH COUNCIL
23	TECHNICAL LIBRARY 2101 CONSTITUTION AVENUE WASHINGTON DC 20418
	NATIONAL AERONAUTICS AND SPACE ADMINISTRATION
24	TECHNICAL LIBRARY LANGLEY RESEARCH CENTER HAMPTON VA 23665
	THE JOHNS HOPKINS UNIVERSITY APPLIED PHYSICS LABORATORY
25	TECHNICAL LIBRARY JOHNS HOPKINS ROAD LAUREL MD 20810
	THE UNIVERSITY OF WASHINGTON APPLIED PHYSICS LABORATORY
26	TECHNICAL LIBRARY 1013 NORTHEAST 40TH STREET SEATTLE WA 98105
	THE PENNSYLVANIA STATE UNIVERSITY APPLIED RESEARCH LABORATORY
27	TECHNICAL LIBRARY P O BOX 30 STATE COLLEGE PA 16801
	THE UNIVERSITY OF CALIFORNIA AT SAN DIEGO MARINE PHYSICAL LABORATORY OF THE SCRIPPS INSTITUTION OF OCEANOGRAPHY
28	TECHNICAL LIBRARY SAN DIEGO CA 92152
	WOODS HOLE OCEANOGRAPHIC INSTITUTION
29	TECHNICAL LIBRARY 86-95 WATER STREET WOODS HOLE MA 02543
30	K GENTLE THE UNIVERSITY OF TEXAS AT AUSTIN PHYSICS DEPARTMENT AUSTIN TX 78712

Distribution List for ARL-TR-93-10 under Grants N00014-91-J-1366 and N00014-93-J-0018 (cont'd)

Copy No.	
31	A GLEESON THE UNIVERSITY OF TEXAS AT AUSTIN PHYSICS DEPARTMENT AUSTIN TX 78712
32	T GRIFFY THE UNIVERSITY OF TEXAS AT AUSTIN PHYSICS DEPARTMENT AUSTIN TX 78712
33	M DOWNER THE UNIVERSITY OF TEXAS AT AUSTIN PHYSICS DEPARTMENT AUSTIN TX 78712
34	R ROBERTS 814-T2 GALLOP HILL ROAD GAITHERSBURG MD 20879
35	MICHAEL R BAILEY ARL:UT
36	NICHOLAS P CHOTIROS ARL:UT
37-40	JEFFREY A COOK ARL:UT
41	JOHN M HUCKABAY ARL:UT
42	THOMAS G MUIR ARL:UT
43	CLARK S PENROD ARL:UT
44-45	ROBERT L ROGERS ARL:UT
46	LIBRARY ARL:UT
47-56	ASG RESERVE ARL:UT